



UNIVERSIDAD DE LA REPÚBLICA  
FACULTAD DE INGENIERÍA



# Design and Implementation of an Attitude Determination and Control System for the AntelSat

TESIS PRESENTADA A LA FACULTAD DE INGENIERÍA DE LA  
UNIVERSIDAD DE LA REPÚBLICA POR

Matías Tassano Ferrés

EN CUMPLIMIENTO PARCIAL DE LOS REQUERIMIENTOS  
PARA LA OBTENCIÓN DEL TÍTULO DE  
MAGISTER EN INGENIERÍA ELÉCTRICA.

## DIRECTORES DE TESIS

Dr. Pablo Monzón ..... Universidad de la República  
Ing. Juan Pechiar ..... Universidad de la República

## TRIBUNAL

Prof. Rafael Canetti ..... Universidad de la República  
Dr. Pablo Musé ..... Universidad de la República  
Dr. Alejandro Romanelli ..... Universidad de la República

## DIRECTOR ACADÉMICO

Dr. Pablo Monzón ..... Universidad de la República

Montevideo  
Wednesday 12<sup>th</sup> August, 2015

*Design and Implementation of an Attitude Determination and Control System for the AntelSat*, Matías Tassano Ferrés.

ISSN 1688-2806

This thesis was written in L<sup>A</sup>T<sub>E</sub>X using the iietesis (v1.1) class.

Contains a total of 145 pages.

Compiled on Wednesday 12<sup>th</sup> August, 2015.

<http://iie.fing.edu.uy/>

Life is not easy for any of us. But what of that?  
We must have perseverance and above all confidence in ourselves. We must believe that we are gifted for something and that this thing must be attained.

MARIE CURIE

We will either find a way or make one.

HANNIBAL, CARTHAGINIAN GENERAL

This page has been intentionally left blank.

# I would like to thank...

My thesis supervisors, Pablo Monzón and Juan Pechiar, for providing their time and guidance.

The rest of the AntelSat team, in particular: Gonzalo Gutiérrez, Ignacio De León, Gonzalo Sotta, Gustavo De Martino, Andrés Touya, Pablo Yaniero, Simón González, Javier Ramos, Victor Macadar and Fernando Lema, for sharing a significant part of their lives with me. Their commitment and endurance made the realization of this whole project possible.

My family for their unwavering support and understanding while my work on this thesis lasted.

The folks at UNI/CTIC in Lima, Perú, in particular Renato Miyagusuku who welcomed me during my short stay in Lima.

This work would not have been possible without the financial support of ANTEL and ANII.

Last, but not least, I would like to deeply thank Anna. To enumerate all the reasons here would be very difficult, but she knows why.

This page has been intentionally left blank.

# Abstract

This thesis describes the design, analysis and construction of the Attitude Determination and Control System (ADCS) for the first Uruguayan nanosatellite, the AntelSat. The AntelSat project is a joint venture between the Electrical Engineering Institute (IIE) of Faculty of Engineering, Universidad de la República (UdelaR University) and Antel, the Uruguayan national telecommunications company. The satellite consists of a two-unit (2U) CubeSat, which implies that the ADCS is designed under tight mass, size, and energy constraints. In addition, these kind of satellites usually have limited sensing, computational and communication capabilities, motivating the need for autonomous and computationally efficient algorithms. Under these strict restraints, developing an effective attitude control system poses a significant challenge.

As presented in this thesis, for the attitude determination section of the ADCS, data available from sensors is taken as inputs for the computation of an optimal quaternion estimator. The use of a quaternion implementation of an unscented Kalman filter is also discussed. Additionally, attitude control is based on magnetic actuation with magnetorquers being commanded by pulse width modulation. It is shown that the control system is able to achieve the detumbling of the satellite after separation from the launch interface using the reliable B-dot control law. Nadir-pointing control is achieved with the use of a simple Linear Quadratic Regulator.

Also pertinent is the simulation environment that was implemented to develop the attitude determination and control algorithms and also to validate their performance. ADCS hardware prototypes and flight versions that were designed and constructed are introduced.

This page has been intentionally left blank.

# Resumen

Este documento de tesis describe el diseño, análisis y construcción de el Sistema de Determinación y Control de Actitud (ADCS por sus siglas en inglés) del primer satélite uruguayo, el AntelSat. El proyecto AntelSat es una actividad conjunta entre el Instituto de Ingeniería Eléctrica (IIE) de la Facultad de Ingeniería de la Universidad de la República y Antel, la empresa de telecomunicaciones nacional de Uruguay. El satélite consiste en un CubeSat de dos unidades (2U), lo que implica que el ADCS es diseñado bajo estrictas restricciones de masa, tamaño y energía. Además, este tipo de satélites posee una capacidad computacional, de comunicaciones y de medición limitada, lo que motiva la necesidad de lograr algoritmos computacionalmente eficientes. Bajo estas estrictas limitaciones, el desarrollo de un sistema de control de actitud efectivo se traduce en un reto importante.

Como se presenta en esta tesis, para el segmento de determinación de actitud del ADCS, la información proveniente de los sensores es tomada como entrada para el cálculo de un estimador de cuaternión óptimo. Se discute también el uso de una implementación con cuaterniones de un filtro de Kalman "unscented". Por otro lado, el control de actitud está basado en actuación magnética con magnetorquers comandados con modulación de ancho de pulso. Se demuestra que el sistema de control es capaz de reducir el valor de velocidad angular del satélite en la fase previa a la separación con la interfaz de lanzamiento, mediante la utilización del algoritmo B-dot. La estabilización de la actitud en modo de apunte al nadir se logra con el uso de un simple regulador lineal cuadrático.

Por otra parte, se presenta el entorno de simulación que fue implementado para el desarrollo de algoritmos de determinación y control de actitud, y también para validar el desempeño de los mismos. A su vez, se exhiben el hardware del ADCS que fue diseñado y construido, tanto prototipos como versiones de vuelo.

This page has been intentionally left blank.

# Preface

It was in November 2011 that I joined the AntelSat team as a member of the research staff at the Electrical Engineering Institute (IIE), Universidad de la República. The project had recently experienced a "restart" since the IIE had joined forces with Antel, the national telecommunications company. The good news about the partnership: the dream of building a satellite could finally materialize. The bad news about the partnership: the dream of building a satellite *had* to materialize, in a defined timeframe and with reasonable results.

Although, prior to my joining the project, there were some completed undergraduate projects dealing with the ADCS, when I began working on this element of the satellite, the majority of the work had to be done from scratch. I was the lead researcher, responsible for the whole of the development of this subsystem of the satellite. Gustavo De Martino, Simón González and Pablo Yaniero significantly contributed to onboard software development, porting and validation, while Ignacio De León, Gonzalo Gutiérrez and Gonzalo Sotta provided valuable support with the fabrication of the hardware and Javier Ramos aided with the testing of the Sun sensors. Portions of the introductory text were adapted from the paper "ATTITUDE DETERMINATION AND CONTROL SYSTEM OF THE URUGUAYAN CUBE-SAT, ANTELSAT" presented at the 16th International Conference on Advanced Robotics.

Considering the construction of the AntelSat, the whole process turned out to be a battle of endurance to be fought on all fronts, shoulder to shoulder with the rest of my team mates. Countless hours and nights passed by down in the trenches of the IIE labs. We fought against a small satellite and bigger circumstances. Ultimately, we prevailed.

Upon completion of this paper, the AntelSat has been in orbit for 10 months, predominantly working as expected.

Matías Tassano Ferrés

This page has been intentionally left blank.

## Acronyms

1U	A 10cm × 10cm × 10cm (one unit) CubeSat
2U	A 20cm × 10cm × 10cm (two units) CubeSat
$\mu$ C	Microcontroller
ADC	Analog-to-Digital converter
ADCS	Attitude Determination and Control System
CoM	Center of mass. It coincides with the center of gravity
CoP	Center of pressure
COTS	Commercial off-the-shelf
DCM	Direction Cosine Matrix
EKF	Extended Kalman filter
I <sup>2</sup> C	Inter-Integrated Circuit
IGRF	International Geomagnetic Reference Field
LQR	Linear quadratic regulator
LSB	Least significant bit
LEO	Low Earth Orbit
MCU	Main controller unit
NORAD	North American Aerospace Defence Command
P-POD	Poly-Picosatellite Orbital Deployer
PCB	Printed circuit board
PWM	Pulse width modulation
RAM	Random access memory
ROM	Read-only memory
SGP	Simplified general perturbations
SPI	Serial Peripheral Interface
TLE	Two Line Element
UKF	Unscented Kalman filter
rpm	Revolutions per minute

w.r.t.      With respect to

## Glossary

Attitude	is the orientation of a satellite.
Apogee	is the closest point to the Earth of an orbit around the Earth.
Eclipse	is, as seen from a satellite, the event where the Sun is obscured by the Earth.
Ecliptic	is the plane described by the apparent path of the Sun on the celestial sphere.
Ecliptic latitude	measures the angular distance of an object from the ecliptic towards the north or south ecliptic pole.
Ecliptic longitude	measures the angular distance of an object along the ecliptic from the primary direction. The primary direction points from the Earth towards the Sun at the vernal equinox of the Northern Hemisphere.
Epoch	is a moment in time used as a reference point for which the position of the orbital elements of a celestial body is specified.
J2000	is an epoch which corresponds to the 1st January 2000, noon TT (11:58:55.816 UTC), or 2451545 in Julian date.
Julian date	is the continuous count of days since noon 1st January 4313 BC. For instance, the Julian date for 00:30:00 UT 1st January 2013 is 2456293.520833.
Latitude	measures how far north or south of the equator a celestial object is located, in degrees.
Longitude	measures how far east or west of the prime meridian a celestial object is located, in degrees. The prime meridian is the Greenwich meridian and the angular measure is measured along the equator.
Mean Anomaly	for a circular orbit, it is the angle traveled by the satellite since the perigee.
Nadir	is the local vertical direction pointing in the direction of the force of gravity.

Obliquity of the ecliptic	is the angle between the plane of the ecliptic and the plane of the Earth's equator.
Orbital rate	is the average angular velocity of an orbit of a satellite.
Perigee	is the furthest point to the Earth of an orbit around the Earth.
Roll, pitch, yaw	are the Euler angles describing the attitude of a satellite w.r.t a certain reference frame.
Vernal equinox	is the point where the ecliptic crosses the equator going from south to north.
Zenith	is the point directly "above" a particular object. "Above" refers to the direction away from the Earth on the line connecting the object center of gravity and the Earth center.

### Reference Frames

ECEF	$\{\hat{i}_{ECEF}, \hat{j}_{ECEF}, \hat{k}_{ECEF}\}$	Earth Centered, Earth Fixed reference frame
ECI	$\{\hat{i}_1, \hat{i}_2, \hat{i}_3\}$	Earth Centered Inertial reference frame
ORF	$\{\hat{o}_1, \hat{o}_2, \hat{o}_3\}$	Orbit reference frame
BRF	$\{\hat{b}_1, \hat{b}_2, \hat{b}_3\}$	Body reference frame
CRF	$\{\hat{c}_1, \hat{c}_2, \hat{c}_3\}$	Control reference frame

### Notation

<b>A, v</b>	Matrices and vectors are in bold type
${}^o\mathbf{v}, {}^b\mathbf{v}, {}^i\mathbf{v}$	Vector <b>v</b> expressed in the Orbit, Body, and Inertial Reference Frame, respectively
$\mathbf{v} = (v_1, v_2, v_3) = [v_1 \ v_2 \ v_3]^T$	Elements of vector <b>v</b>
$\hat{\mathbf{u}}$	Unit vector
$\mathbf{q}^*$	Complex conjugate
$\mathbf{P} > 0$	Matrix <b>P</b> is positive definite
$diag([v_1 \dots v_n]^T)$	Diagonal matrix with zero off-diagonal elements and $[v_1 \dots v_n]^T$ corresponding to its diagonal

## Symbols

${}^c\boldsymbol{\omega}_{ci}$	Angular velocity from the Inertial Frame to the Control Frame, expressed in the Control Frame
$\mathbf{q}_{co}$	Attitude quaternion representing the rotation of the Control Frame w.r.t. the Orbit Frame
$\mathbf{m}$	Magnetic moment
$\mathbf{R}_{co}$	Rotation matrix from Orbit to Control Frame
$\mathbf{T}_{ctrl}$	Control torque applied by the satellite magnetic actuators
$\mathbf{T}_{dist}$	Disturbances torque
$\mathbf{T}_{gg}$	Gravity gradient torque
$\mathbf{T}_{ext}$	External torque
$\mathbf{I}$	Satellite's inertia tensor
${}^b\mathbf{m}$	Net magnetic dipole generated by the magnetorquer
$\mathbf{R}(\mathbf{q})$	Rotation matrix defined by a quaternion
$C_D$	Proportional gain of the B-dot control law
$\mathbf{B}_E$	Earth's magnetic field vector
$s$	Laplace transform variable
$\omega_c$	User selectable cut-off frequency of the state variable filter
$\omega_o$	Orbital rate
$T$	Orbital period
$T_s$	Sampling time
$\mathbf{i}_{coil}$	Magnetorquer current vector
$N_{coil}$	Number of coil windings
$A_{coil}$	Coil area
$\mathbf{E}_{n \times n}$	$n \times n$ identity matrix
$\mathbf{0}_{n \times n}$	$n \times n$ zeros matrix
$(\cdot)_k$	Signal at time $t = k$
$(\cdot)_{k-1}$	Signal at time $t = k - 1$
$\varphi, \theta, \psi$	Roll, pitch, yaw
$[\mathbf{a} \times]$	Skew symmetric matrix operator
$\mathbf{W}(\boldsymbol{\omega})$	$4 \times 4$ skew symmetric velocity



This page has been intentionally left blank.

# Contents

<b>1</b>	<b>Introduction</b>	<b>1</b>
1.1	The CubeSat Standard . . . . .	2
1.2	The AntelSat nanosatellite and its subsystems . . . . .	3
1.3	Introduction to ADCS . . . . .	7
1.4	The AntelSat orbit and launch vehicle . . . . .	8
1.5	Thesis Structure . . . . .	9
<b>2</b>	<b>Satellite Modelling</b>	<b>11</b>
2.1	Orbits and Two Line Elements . . . . .	11
2.2	Coordinate Systems . . . . .	15
2.3	Attitude Parametrizations and Rotations . . . . .	17
2.3.1	Direction Cosine Matrix . . . . .	17
2.3.2	Quaternions . . . . .	17
2.4	Environment Modelling . . . . .	19
2.4.1	Gravity-gradient Torque . . . . .	19
2.4.2	Solar Radiation Torque . . . . .	20
2.4.3	Aerodynamic Torque . . . . .	20
2.4.4	Magnetic Field . . . . .	22
2.5	Equations of Motion . . . . .	23
2.5.1	Attitude Dynamics . . . . .	24
2.5.2	Control Torque . . . . .	24
2.5.3	Attitude Kinematics . . . . .	25
2.6	Controllability . . . . .	26
2.7	Linearization . . . . .	27
2.7.1	Linearized Kinematics . . . . .	28
2.7.2	Linearized Dynamics . . . . .	28
2.7.3	Complete Linearized System . . . . .	30
2.7.4	Averaged Linearized System . . . . .	30
2.8	Summary . . . . .	31
<b>3</b>	<b>Attitude Determination</b>	<b>33</b>
3.1	Deterministic Method . . . . .	33
3.1.1	Introduction . . . . .	33
3.1.2	Wahba's problem . . . . .	34
3.1.3	Optimal Quaternion Estimation Method . . . . .	36

## Contents

3.2	Filtering Method . . . . .	37
3.2.1	Introduction . . . . .	37
3.2.2	Unscented Kalman Filtering . . . . .	38
3.2.3	UKF implementation for AntelSat . . . . .	40
3.3	Simulations . . . . .	44
3.4	Summary . . . . .	49
<b>4</b>	<b>Attitude Control</b> . . . . .	<b>51</b>
4.1	Detumbling Controller . . . . .	52
4.1.1	B-dot proportional control law . . . . .	52
4.1.2	Lyapunov Stability . . . . .	53
4.1.3	State variable filter . . . . .	53
4.1.4	Simulations . . . . .	54
4.2	Nominal Controller . . . . .	65
4.2.1	Averaging theory . . . . .	65
4.2.2	Simulations . . . . .	67
4.3	Summary . . . . .	71
<b>5</b>	<b>AntelSat Simulation Environment</b> . . . . .	<b>73</b>
5.1	Introduction . . . . .	73
5.2	Reference Models . . . . .	74
5.2.1	Orbit Propagators . . . . .	75
5.2.2	Magnetic Field Model . . . . .	75
5.2.3	Sun Vector Model . . . . .	76
5.2.4	Eclipse model . . . . .	77
5.3	Sensor and Actuator Models . . . . .	77
5.3.1	Magnetometer Model . . . . .	78
5.3.2	Sun Sensors Model . . . . .	79
5.3.3	Gyroscope Model . . . . .	80
5.3.4	Magnetorquer Model . . . . .	81
5.4	Summary . . . . .	82
<b>6</b>	<b>AntelSat Hardware</b> . . . . .	<b>83</b>
6.1	Introduction . . . . .	83
6.2	Attitude Actuators . . . . .	84
6.2.1	Estimating Minimum Requirements for AntelSat Actuators . . . . .	85
6.2.2	AntelSat Actuators Specifications . . . . .	86
6.3	Attitude Sensors . . . . .	88
6.3.1	AntelSat Sensors Specifications . . . . .	89
6.4	Design of the Hardware . . . . .	92
6.5	Summary . . . . .	95
<b>7</b>	<b>Conclusions and Recommendations</b> . . . . .	<b>97</b>
7.1	Conclusions . . . . .	97
7.2	Recommendations for Future Work . . . . .	98

<b>A</b>	<b>Worst case disturbance torques</b>	<b>99</b>
A.1	Aerodynamic Drag . . . . .	99
A.2	Solar Radiation Pressure . . . . .	100
A.3	Gravity-gradient . . . . .	100
A.4	Total Torque . . . . .	100
<b>B</b>	<b>AntelSat and ADCS Pictures</b>	<b>101</b>
<b>C</b>	<b>ADCS After Launch</b>	<b>107</b>
	<b>Bibliography</b>	<b>111</b>
	<b>List of Tables</b>	<b>117</b>
	<b>List of Figures</b>	<b>118</b>

This page has been intentionally left blank.

# Chapter 1

## Introduction

Recent years have seen a tremendous boost in the number of small satellites developed. This increment has been possible because of the significant reduction in cost and development time, which can be explained by different factors, one of these being the massive advances in integrated circuit technologies and microelectronics in general. Higher computing power together with more sophisticated solutions and lower energy consumption are available at affordable costs. Some authors suggest that the single largest step in reducing software cost is the use of commercial, off-the-shelf (COTS) software [1]. This is analogous for the adoption of COTS microelectronics in space application. Another relevant factor is the reduction of launch costs by sharing the launch vehicle with other missions, particular with a primary, larger mission. In this scenario—“piggy-backing”—the launch cost for one of the smaller satellites is only a fraction of the total launch cost.

An outstanding breakthrough in the small satellites field is the conception of the CubeSat standard [2]. Initially developed by California Polytechnic State University (Cal Poly) and Stanford University in 1999, the CubeSat standard nowadays enjoys wide acceptance and has been adopted by several institutions around the globe [3–6]. This standard introduced a launch system interface for nanosatellites. The use of this standardized interface leads to dramatic launch cost reductions and an increase in the number of launch possibilities. Nowadays, launch prices for a 1-unit CubeSat are close to USD 100,000 and projects usually take five months to three years from conception to launch. This explains why most of these projects are carried out by academic institutions, which take advantage of the vast amount of educational aspects inherent in the process. To set a comparative example, we consider the Earth-observing satellite ENVISAT, developed by the European Space Agency [7]. Construction of the ENVISAT started in December 1993 and the satellite was finally launched in March 2002. The total cost of the project was about USD 2.5 billion. Clearly, the development of a project of this magnitude is prohibitive for the vast majority of universities, whereas building a CubeSat presents itself as an attractive and feasible project.

The Lai project started back in 2008 when a group of professors from the IIE decided to start working on a student project aiming to launch a satellite. The first approaches were composed of attaching simple payloads to meteorological balloons.

## Chapter 1. Introduction

A total of four of these balloons were released as independent projects [8]. Due to the fact that these experiments proved successful, the next step was to start the development of a real nanosatellite dividing it in five different subsystems: Energy Management, Communications, Main Control, Attitude Determination and Control, and Payload. Some students at the IIE started working on some of these subsystems as undergraduate projects. However, in November of 2011, Antel, the national telecommunications company of Uruguay, became interested in the project and started funding the AntelSat CubeSat venture. Additionally, a group of engineers from Antel were in charge of developing the Payload subsystem. The development of the rest of the satellite was in charge of the research staff at the IIE.

### 1.1 The CubeSat Standard

As already mentioned, the introduction of the CubeSat standard opened up new horizons to universities worldwide willing to carry out projects related with space science and exploration. However, although most of the CubeSat projects come from academia, several companies build these type of satellites, e.g. the large aerospace company Boeing. The standard defines structural characteristics of the spacecraft: a 1-unit (1U) CubeSat has a volume of exactly one liter in the shape of a 10 cm cube and has mass of no more than 1.33 kg. CubeSats can also be expanded along one axis, i.e. a 2U CubeSat is a  $200\text{mm} \times 100\text{mm} \times 100\text{mm}$  prism and a 3U is a  $300\text{mm} \times 100\text{mm} \times 100\text{mm}$  prism. Additionally, the center of mass of the satellite must not be more than 2 cm away from its geometrical center.

Another important aspect of these type of spacecraft is that all CubeSats can be launched and deployed using a common deployment mechanism. This system is called the Poly-PicoSatellite Orbital Deployer (P-POD), which are developed and built by Cal Poly. Figure 1.1 displays the AntelSat ready to be inserted inside a P-POD.

These design specifications entail several advantages. First, by simplifying the design, the production of a satellite can be obtained at lower costs. On top of that, the introduction of the launch interface also brings down launch costs and managerial work involved. On the other hand, the CubeSat specification also imply stringent constraints on mass, volume and power budgets when designing the onboard systems. Particularly, if we consider the total external surface of a 1U CubeSat covered with solar panels, it will be only possible to obtain about 2W of power, which is clearly not a large amount to run a whole satellite.

## 1.2. The AntelSat nanosatellite and its subsystems

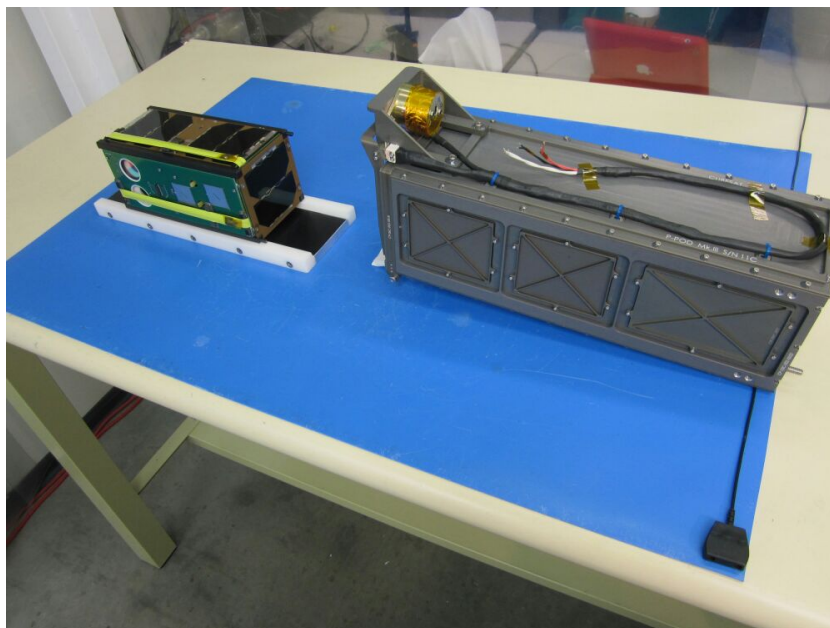


Figure 1.1: AntelSat ready to be inserted into a P-POD. This picture was taken inside a clean room at Cal Poly.

## 1.2 The AntelSat nanosatellite and its subsystems

AntelSat follows the CubeSat standard for a 2U CubeSat. Under these circumstances, the spacecraft is to weigh under 2.66 kg and the body consists of a rectangular prism with dimensions of  $200\text{mm} \times 100\text{mm} \times 100\text{mm}$ . Solar panels are mounted on five of its six sides and the remaining side is reserved for its two cameras (IR and visible spectrum) and its two S band antennas. Basically, AntelSat is a combined Earth-observation/technology demonstration mission, with the clear aim of acquiring knowledge and experience in the aerospace field.

Some of the key design aspects taken into account were low power consumption and maintaining modularity in the subsystems. A key reason for the latter is the fact that the project as a whole is conceived for educational and training purposes. Hence, each subsystem possesses its own microcontroller and is responsible for carrying out relevant tasks as independently and autonomously as possible. Furthermore, another predominant factor was dealing with the compromise between including redundancy in vital parts while keeping complexity at an affordable level.<sup>1</sup>

Each of the subsystem main microcontrollers are MSP430 from Texas Instruments. The major reasons for choosing this family of processors are their remarkably low power consumption and the previous domestic usage experience at IIE, along with the fact that they have been used in other comparable CubeSat projects [9–11].

---

<sup>1</sup>The KISS design principle was a mission motto in every moment of the development. KISS stands for "keep it short and simple" and is a concept introduced by the US Navy in 1960's.

## Chapter 1. Introduction

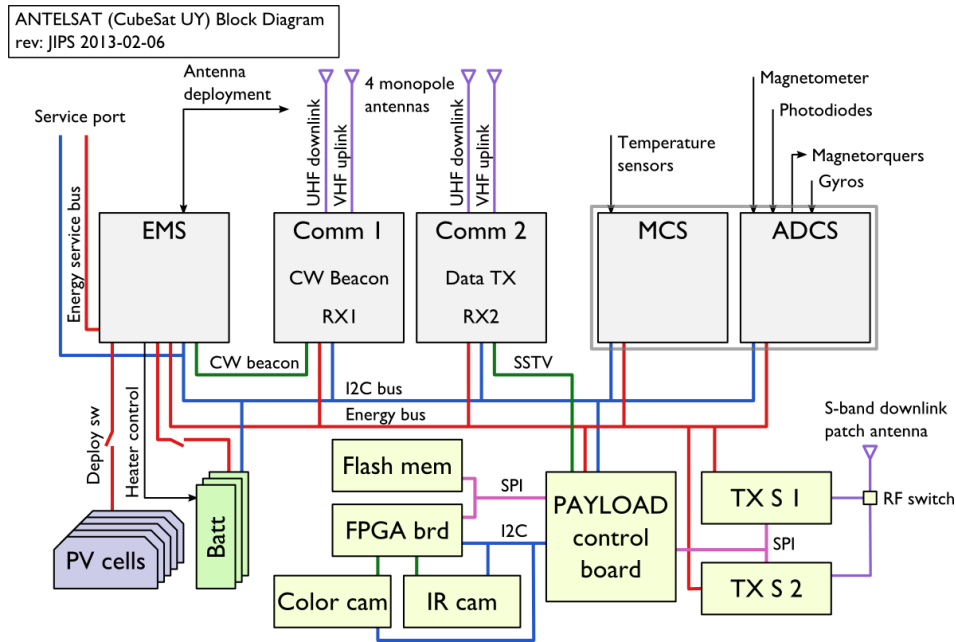


Figure 1.2: AntelSat nanosatellite subsystems and their interconnections.

As shown in Fig. 1.2, the onboard subsystems of the AntelSat are:

- **EMS** stands for Energy Management Subsystem. This subsystem is in charge of the power distribution to the rest of the subsystems, and also of handling current overloads. It handles the energy coming from the solar panels and stores it in the batteries. It features a maximum power tracking system (MPPT) to maximize the power acquired from the panels. Additionally, it electrically controls the radio beacon—even though the electronics of the latter are physically located in the COMM 1 board.
- **COMM 1 and 2** are the two radio communications subsystems. Each of the subsystems possess a VHF radio receiver, a total of two with the idea of redundancy in mind. COMM 1 contains the electronics of the radio beacon—although the beacon is commanded by the EMS—, whereas the COMM 2 has an UHF radio transmitter. COMM 2 also implements a slow-scan TV (SSTV) transmission mode to download pictures taken by the satellite in lower resolution.
- **MCS** is the Main Control Subsystem. This subsystem is composed only of a microprocessor and is in charge of understanding commands coming from the ground station. It is also in charge of collecting and sending logs.
- **Payload** is composed of two S band transmitters, a visible spectrum camera, an infrared camera, an FPGA to control the cameras, and a control board.
- **ADCS** stands for Attitude Determination and Control Subsystem. Attitude refers to the orientation/rotation of the spacecraft in space. The ADCS is

## 1.2. The AntelSat nanosatellite and its subsystems

introduced further in the next section.

All subsystems intercommunicate using an I2C bus.

Considering the mission success criteria, the first item in the expectations list of the AntelSat design team was to prepare a satellite qualified for launch, that is, a satellite which would pass all the pre-launch validations required by the launch service provider. This implies to have come through a successful design, fabrication and validation phases, which are not trivial tasks, in particular considering that AntelSat has been the first-of-its-kind type of venture in Uruguay. Then, assuming an already orbiting AntelSat, the following is the mission success criteria, in order of priority:

- Antennas are deployed and two-way communication is established with the spacecraft.
- The satellite is able to manage its power normally.
- The satellite detumbles itself.
- The satellite is able to take pictures of the Earth and download them using SSTV.
- The satellite is able to point to its nadir.
- S band communication is established.
- The satellite is able to download pictures using the S band transmitters.
- Scientific experiments are able to be performed. <sup>2</sup>

Figure 1.3 shows a render of the AntelSat with the antennas in a stowed configuration which illustrates the dimensions of the body of the spacecraft. Figure 1.4 is a render which displays an exploded view of the satellite.

---

<sup>2</sup>The scientific experiments to be run on the orbiting spacecraft include studying the effect of radiation in the onboard electronics and taking measurements with an ultra-low temperature sensor designed in the IIE (see [12]).

# Chapter 1. Introduction

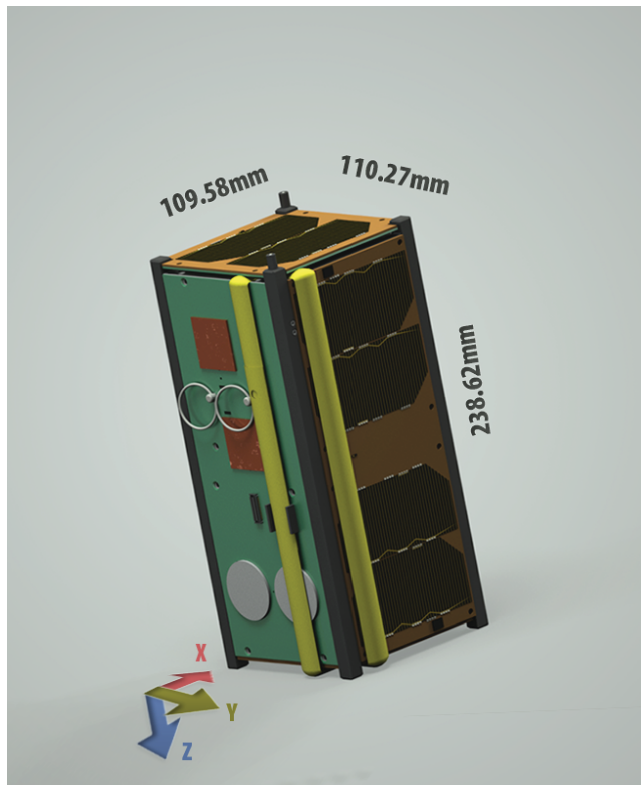


Figure 1.3: Render of the AntelSat with antennas in a stowed configuration.

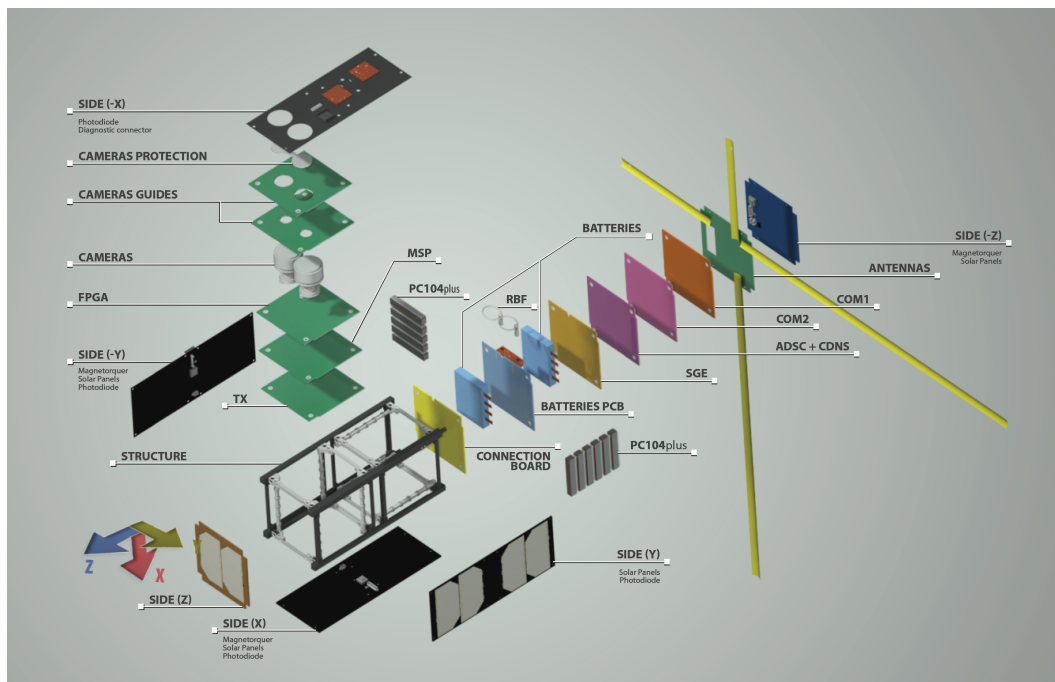


Figure 1.4: Render with an exploded view of the AntelSat.

## 1.3 Introduction to ADCS

Essentially, there are two objectives of the ADCS: to detumble the satellite, i.e. to reduce the satellite's angular rates<sup>3</sup>, and to point the side of the satellite with the cameras to the nadir. These goals must be achieved provided that the mass and volume of the ADCS do not exceed 20% of the AntelSat total values and that power cannot exceed 400 – 600 mW nominal.

Reasons to achieve the objectives above include:

- The direction of highest gain of the antennas should be pointing to the surface of the Earth to optimize the quality of communication.
- Cameras should point to the surface of the Earth and need a slow angular rate to achieve the best possible picture quality.
- The surface of solar panels exposed to solar radiation should be optimized in order to maximize power generation. A good scenario to achieve the former would be that face of the satellite which includes the cameras and patch antennas points to the nadir most of the time.

The ADCS can be divided in two main functions: attitude determination and attitude control. Attitude determination involves that the satellite must be able to determine its orientation in space and its rotation rate, whereas attitude control is involved with the ability to reorient the satellite into a desired attitude. Attitude determination relies on sensors and attitude estimation algorithms, while attitude control employs actuators and control algorithms. As can be seen in Fig. 1.2, ADCS sensors include a 3-axis magnetometers, six Sun sensors and three 1-axis gyroscopes, whereas actuators are three electromagnetic coils, or magnetorquer, one for each geometrical axis of the satellite.

As for the rest of the subsystems, a key design aspect of the ADCS was to maintain complexity as low as possible. This was one of the main reasons why other sensors or actuators were discarded, e.g. GPS or reaction wheels. As the ADCS is not one of the most critical subsystems in the spacecraft, redundancy was not added in order to preserve simplicity.

From the beginning, it was clear that the design of the ADCS could be approached subdividing it into its two main functions aforementioned. From that point, strategies to approach both functions were considered in parallel. In both cases, the selection of the strategies to be followed was to be strongly bonded to the need of implementation of these strategies within a defined timeframe, the lack of power and computational resources, and whether they were successful or not in similar previous missions.

Attitude control for missions that aim for three-axis control with magnetic actuation are commonly treated as two separate problems: a tumbling satellite and a nominal pointing mode. For the detumbling problem, by far the most used

---

<sup>3</sup>Angular velocities of a satellite could be relatively high—tens of degrees per second—especially after deployment from the launch rocket. In this situation, the dynamics of the satellite behave mostly nonlinearly.

## Chapter 1. Introduction

algorithm is the simple and robust B-dot control law and the chosen one to be implemented for the AntelSat. For the nominal pointing mode, a Linear Quadratic Regulator, which provides a computationally simple and power efficient control algorithm, was selected. More elaborated control strategies, such as Model Prediction Control or neural networks, were discarded for the reasons mentioned above.

Parallely, unlike attitude control, attitude determination is not considered as two separate problems but one. However, it was decided to make use of two different determination algorithms, for the reasons explained below. First, a deterministic optimal quaternion estimator was implemented for running on the onboard hardware. The design of the algorithm was completed in a short time and advantages of the algorithm itself include being computationally simple, whereas its disadvantages include that the algorithm is not able to yield valid outputs when the satellite is in eclipse, considering the sensor selection for the AntelSat mission. In this context, it was decided to also utilize a statistical filter which overcame this drawback. Thus, it was decided to implement an attitude estimator based on an unscented Kalman filter (UKF). The application of UKF on a CubeSat is very recent<sup>4</sup> which made for an interesting opportunity to approach a state-of-the-art method on the AntelSat. Unfortunately, the complete implementation of this filter could not be achieved on time and the UKF approach was not included in the onboard software. Nonetheless, Simulink code of the filter was later completed and validated, and the results are included in this thesis.

### 1.4 The AntelSat orbit and launch vehicle

The AntelSat was launched in a Dnepr rocket from Yasny, in the Orenburg region of Russia. Dnepr rockets consist of converted SS-18 intercontinental ballistic missiles and are nowadays used for launching artificial satellites into orbit, operated by launch service provider ISC Kosmostras [14]. Figure 1.5 shows a diagram of the Dnepr diagram.

The launch happened on 19th June 2014. In that occasion, AntelSat was launched together with other thirty-six satellites, establishing a world record for the most spacecraft launched by a single rocket [15]. Table 1.1 shows the characteristics of the Sun-synchronous polar orbit of the AntelSat.

---

<sup>4</sup>The first project of this kind dates back to 2011, see [13]

## 1.5. Thesis Structure

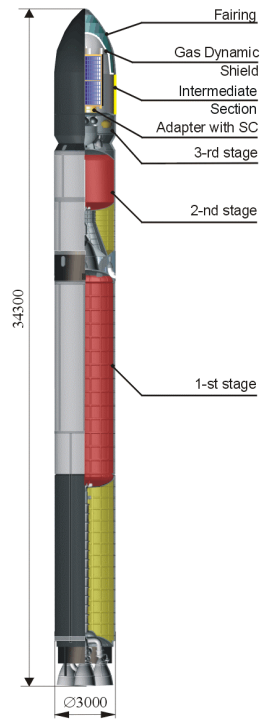


Figure 1.5: Diagram of Dnepr rocket (units in mm) [14].

Orbit Parameter	Value
Height	653 km
Period	98 min
Inclination	98°
Eccentricity	0.00589
RAAN	20.94°
Argument of perigee	248.33°

Table 1.1: AntelSat orbital parameters.

## 1.5 Thesis Structure

The remaining of the thesis is organized in the following way:

- **Chapter 2: Satellite Modelling**

The theoretical foundations needed for the development of the additional chapters are provided in this chapter. It introduces Keplerian orbits, coordinate systems used in the thesis as well as rotations and quaternions—the selected attitude parametrization. It also presents the environment of a

## Chapter 1. Introduction

spacecraft in space, with a focus on the disturbance torques and the satellite equations of motion.

- **Chapter 3: Attitude Determination**

This chapter discusses the two different attitude estimation methods proposed for the AntelSat: a deterministic method and an unscented Kalman filter. Descriptions for both start by giving a theoretical introduction and follow with the design of each estimator. The chapter closes with computer simulations showing the performance of both methods.

- **Chapter 4: Attitude Control**

This chapter introduces the attitude control strategies based on magnetic actuation. First, the detumbling controller is presented: a robust and simple controller with the aim of keeping the rotational velocity of the satellite low. Second, the nominal pointing controller: a Linear Quadratic Regulator (LQR) for 3-axis satellite control. Computer simulations are also included.

- **Chapter 5: AntelSat Simulation Environment**

The simulation environment developed as a tool for both developing the attitude determination and control algorithms and for assessing their performance is reviewed in this chapter. Models used for sensors and actuators are explained.

- **Chapter 6: AntelSat Hardware**

This chapter is devoted to the design and construction of the hardware of the AntelSat ADCS. The selection of sensors and actuators is addressed.

- **Chapter 7: Conclusions and Recommendations for Future Work**

This chapter includes the concluding remarks of the thesis and the recommendations for future work.

# Chapter 2

## Satellite Modelling

Before trying to determine and control the attitude of a spacecraft, accurate models of the orbit and the satellite equations of motions, as well as of the disturbances that affect the system, are needed. These models are then used for the design of algorithms and for the simulator used to validate them.

In order to give the necessary background, Section 2.1 starts this chapter by offering a general description on Keplerian orbits and Two Line Elements. Section 2.2 continues with an explanation of the different coordinate systems used in this thesis. Section 2.3 follows with the different attitude parametrizations and in particular quaternions, the selected parametrization for this thesis. Section 2.4 presents the equations used for modelling the environment and the different disturbance torques considered, while the satellite equations of motion are presented in Section 2.5. Finally, Sections 2.6 and 2.7 introduce theory foundations on which to base the design of the attitude controller.

### 2.1 Orbits and Two Line Elements

Kepler's three empirical laws of planetary motion are commonly used to describe a system composed of a spacecraft orbiting around the Earth. There are six classical elements to fully describe a Keplerian orbit. These consist of five independent quantities which completely describe the size, shape and orientation of an orbit plus one quantity required to determine the position of a satellite along the orbit [16]:

- $a$ : semimajor axis
- $e$ : eccentricity
- $M$ : mean anomaly
- $\Omega$ : right ascension longitude of the ascending node (RAAN)
- $i$ : inclination of the orbit plane
- $\omega$ : argument of the perigee

## Chapter 2. Satellite Modelling

Elements  $a$  and  $e$  determine the size and shape of an elliptic orbit. An eccentricity value of  $0 < e < 1$  indicates an elliptic orbit, whereas  $e = 0$  implies a circular orbit and  $e > 1$  an hyperbolic orbit. In the case of the orbit of the AntelSat, the eccentricity is very close to zero and for practical reasons we consider a circular orbit.

The mean anomaly  $M$  pinpoints the position of the satellite at a given time. For a circular orbit, this is the angle travelled by the satellite from the perigee (the closest point of the orbit to the Earth). The mean anomaly is given in degrees by:

$$M = 360 \cdot \frac{(t_e - t_p)}{T} \quad (2.1)$$

where  $T$  is the orbital period and  $t_e - t_p$  represents the time required to travel from the perigee to a certain position.  $t_e$  is called time of epoch and is measured in the Julian Date (JD) format. This date is measured in days since noon of January 1st, 4713 BC. The mean anomaly can be used to calculate the true anomaly  $\nu$ , which is similar to the mean anomaly but for elliptic orbits.

The RAAN element  $\Omega$  is the angle measured from the vernal equinox (see Section 2.2)  $\gamma$  to the ascending node, counterclockwise. The ascending node is the point where the satellite crosses the Earth's equatorial plane from south to north.

The inclination  $i$  is the angle between the Earth's equatorial plane and the orbital plane. Orbits with  $i < 90^\circ$  are called prograde, while orbits with  $i > 90^\circ$  are called retrograde. An equatorial orbit has zero inclination and a polar orbit  $i = 90^\circ$ .

The angle argument of perigee  $\omega$  determines the orientation of the orbit in its plane. It is the angle measured between the perigee and the ascending node in the direction of the velocity of the satellite. Figure 2.1 displays an example of a Keplerian orbit featuring these elements.

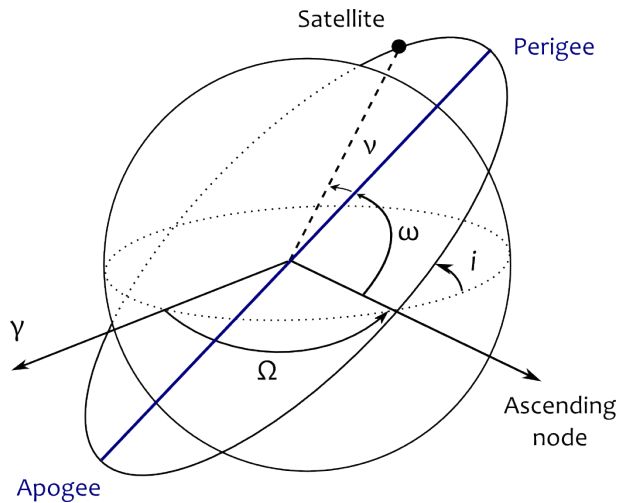


Figure 2.1: Geometric properties of an ellipse and Keplerian orbital elements.

The Two Line Elements (TLE) elements can be obtained from the North American Aerospace Defense Command (NORAD) [17]. NORAD is a combined organi-

## 2.1. Orbits and Two Line Elements

zation from Canada and the United States that provides orbital elements of man-made objects in space. The elements are published in the TLE format. Table 2.1 illustrates this format.

TLEs are used as inputs in a Simplified General Perturbations (SGP) orbit propagator. Section 5.2.1 treats more into detail orbit propagators and how the position and velocity of the spacecraft are computed.

---

**Line 1**

---

<b>Column</b>	<b>Description</b>
01	Line Number of Element Data
03-07	Satellite Number
08	Classification (U=Unclassified)
10-11	International Designator (Last two digits of launch year)
12-14	International Designator (Launch number of the year)
15-17	International Designator (Piece of the launch)
19-20	Epoch Year (Last two digits of year)
21-32	Epoch (Day of the year and fractional portion of the day)
34-43	First Time Derivative of the Mean Motion
45-52	Second Time Derivative of Mean Motion (decimal point assumed)
54-61	BSTAR drag term (decimal point assumed)
63	Ephemeris type
65-68	Element number
69	Checksum (Modulo 10)

---

**Line 2**

---

<b>Column</b>	<b>Description</b>
01	Line Number of Element Data
03-07	Satellite Number
09-16	Inclination [Degrees]
18-25	Right Ascension of the Ascending Node [Degrees]
27-33	Eccentricity (decimal point assumed)
35-42	Argument of Perigee [Degrees]
44-51	Mean Anomaly [Degrees]
53-63	Mean Motion [Revs per day]
64-68	Revolution number at epoch [Revs]
69	Checksum (Modulo 10)

---

Table 2.1: TLE set format [18]

## 2.2 Coordinate Systems

This section defines the coordinate systems used throughout this thesis. They are introduced in order to define vectors in  $\mathbb{R}^3$  and to describe the spaceflight dynamics. All coordinate systems considered are right-handed three-dimensional Cartesian systems, and the term reference frame will be used as an indistinguishable synonym of the former. The idea behind the definition of the reference frames is that multiple reference frames carefully placed ease calculations.

- Earth Centered Inertial Reference Frame (ECI)

This inertial frame  $\mathfrak{F}_i = \{\hat{i}_1, \hat{i}_2, \hat{i}_3\}$  has its origin in the center of mass of the Earth. Its z-axis (i.e.  $\hat{i}_3$  direction) points toward the North Pole, while the x-axis points toward the vernal equinox (i.e. the  $\hat{i}_1$  direction is parallel to the Sun-to-Earth line on the first day of spring in the northern hemisphere). The  $\hat{i}_2$  unit vector completes the right-hand orthogonal coordinate system.

The motion of a rigid body in space, such as a satellite, is best described in an inertial frame. In such frames, no fictitious forces are present (e.g centrifugal force). The ECI is not a perfect inertial frame since the Earth rotates around the Sun and about itself, both resulting in centripetal accelerations. Nonetheless, these accelerations can be neglected [19].

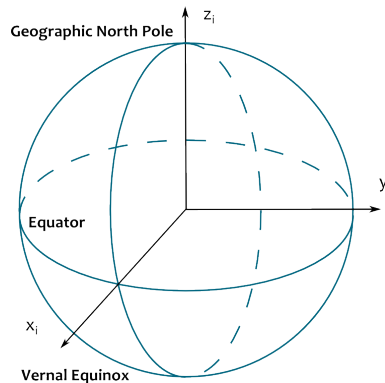


Figure 2.2: Inertial Reference Frame

- Orbit Reference Frame (ORF)

The orbit frame considered in this thesis is that which is usually referred to as ‘Local Vertical Local Horizontal’ (LVLH), as the two defining directions are vertical and horizontal to the Earth’s surface at the location of the spacecraft. The orientation of the satellite with respect to the ORF is also known as roll, pitch and yaw.

In the ORF  $\mathfrak{F}_o = \{\hat{o}_1, \hat{o}_2, \hat{o}_3\}$ , the z-axis is always nadir-pointing. The x-axis is perpendicular to the z-axis and is included in the orbit plane. The x-axis has the same direction as the velocity vector if the orbit is circular.

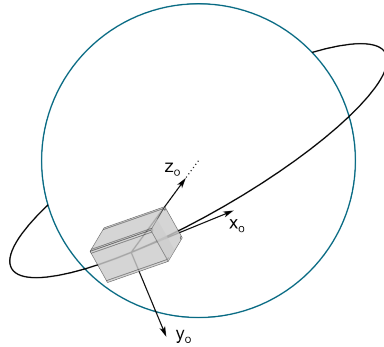


Figure 2.3: Orbit Reference Frame

- Body Reference Frame (BRF)

The origin of the BRF  $\mathfrak{F}_b = \{\hat{b}_1, \hat{b}_2, \hat{b}_3\}$  is placed in the center of gravity of the satellite and its axes are parallel to the edges of the CubeSat, i.e. normal to its side plates.  $\hat{b}_3$  points along the camera boresight and  $\hat{b}_1$  points through the UHF/VHF antennas panel.

In aeronautics, this particular ordering for the body frame is defined as ‘forward-down-over the right wing plane’ for x-y-z, respectively. This frame is helpful for defining the orientation of the attitude measurements and ADCS hardware.

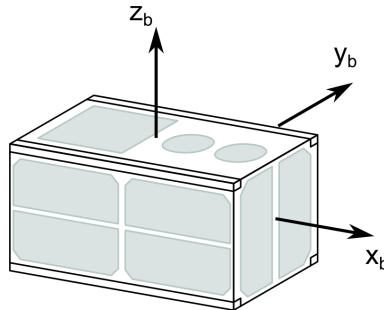


Figure 2.4: Body Reference Frame

- Control Reference Frame (CRF)

The CRF  $\mathfrak{F}_c = \{\hat{c}_1, \hat{c}_2, \hat{c}_3\}$  is located in the center of mass (CoM) and its axes coincide with the principal axes of the satellite. This assures that the inertia tensor expressed in this frame is a diagonal matrix, in which its diagonal elements are the eigenvalues of the inertia matrix.

Unless otherwise indicated, the simplifying assumption that the CRF and BRF coincide will hold through the thesis in order to demonstrate concepts in a clearer manner.

## 2.3 Attitude Parametrizations and Rotations

Although other parametrizations provide a clearer physical interpretation—e.g. Euler angles—the preferred parametrization for this thesis is quaternions, as in several other projects [20–22]. This is justified by the absence of singularities and the fact that quaternions provide a convenient product rule for successive rotations, which makes them computationally faster than other representations. The information presented in this section is mostly based on [23].

### 2.3.1 Direction Cosine Matrix

With reference frames already introduced, it follows to discuss rotations of such frames, in order to express the orientation of objects relative to different viewpoints. The basic problem is to specify the orientation of the CRF w.r.t. some reference coordinate frame, e.g. the ORF. It is important that the rotation which transforms one coordinate frame into the other preserves distance and natural orientation of  $\mathbb{R}^3$ . If  $\mathbf{A}$  is the transformation matrix, it must be a proper real orthogonal matrix, that is, it must comply with the following constraints

$$\begin{aligned}\mathbf{A}\mathbf{A}^T &= \mathbf{E}_{3 \times 3} \\ \det \mathbf{A} &= 1\end{aligned}\tag{2.2}$$

where  $\mathbf{E}_{3 \times 3}$  is the 3 by 3 identity matrix. A transformation matrix of this type is called a direction cosine matrix (DCM). The DCM has nine parameters, but only three degrees of freedom.

For instance, a vector expressed in the ORF can be transformed to the BRP using the DCM which relates both coordinate systems,  $\mathbf{R}_{bo}$ , in the following manner

$${}^b\mathbf{v} = \mathbf{R}_{bo} {}^o\mathbf{v}\tag{2.3}$$

For the inverse transformation,  $\mathbf{R}_{ob}$  is used instead, which is the transpose of  $\mathbf{R}_{bo}$  since they are orthonormal matrices

$$\mathbf{R}_{ob} = \mathbf{R}_{bo}^{-1} = \mathbf{R}_{bo}^T$$

### 2.3.2 Quaternions

The quaternions are an extension of the complex numbers, i.e. an example of the more general class of hypercomplex numbers. They are members of a noncommutative division algebra and the set of quaternions is denoted  $\mathbb{H}$ . The quaternion  $\mathbf{q}$  is composed of a scalar  $q_4$  and a vector  $\mathbf{q}_v$

$$\mathbf{q} = [\mathbf{q}_v^T \ q_4]^T = [q_1 \ q_2 \ q_3 \ q_4]^T = \mathbf{i}q_1 + \mathbf{j}q_2 + \mathbf{k}q_3 + q_4\tag{2.4}$$

## Chapter 2. Satellite Modelling

where  $\mathbf{i}$ ,  $\mathbf{j}$ ,  $\mathbf{k}$  are basis elements of  $\mathbb{H}$  and satisfy the following conditions (known as special products)

$$\begin{aligned} \mathbf{i}^2 = \mathbf{j}^2 = \mathbf{k}^2 = \mathbf{ijk} &= -1 \\ \mathbf{ij} = \mathbf{k} = -\mathbf{ji} \\ \mathbf{jk} = \mathbf{i} = -\mathbf{kj} \\ \mathbf{ki} = \mathbf{j} = -\mathbf{ik} \end{aligned} \quad (2.5)$$

The complex conjugate of the quaternion  $\mathbf{q}$  is defined as

$$\mathbf{q}^* = [-\mathbf{q}_v^T \ q_4]^T \quad (2.6)$$

The norm, or length, of the quaternion  $\mathbf{q}$  is given by

$$|\mathbf{q}| = \sqrt{\mathbf{q}^*\mathbf{q}} = \sqrt{q_1^2 + q_2^2 + q_3^2 + q_4^2} \quad (2.7)$$

Unit quaternions ( $|\mathbf{q}| = 1$ ) are used to describe 3D rotations. Their construction is based on Euler's rotation theorem. The latter states that the rotation of coordinate systems can be uniquely described by a unit vector  $\mathbf{e} = [e_1 \ e_2 \ e_3]^T$  and an angle of rotation  $\phi$ . Then, the quaternion  $\mathbf{q}$  can be expressed as

$$\begin{aligned} q_1 &\equiv e_1 \sin(\phi/2) \\ q_2 &\equiv e_2 \sin(\phi/2) \\ q_3 &\equiv e_3 \sin(\phi/2) \\ q_4 &\equiv \cos(\phi/2) \end{aligned} \quad (2.8)$$

Additionally, the same attitude can be expressed by two quaternions,  $\mathbf{q}$  and  $-\mathbf{q}$ .

An often useful expression in attitude determination is the direct cosine matrix from the ORF to the CRF and it is given as

$$\mathbf{R}_{co} = [{}^c\mathbf{i}_o \ {}^c\mathbf{j}_o \ {}^c\mathbf{k}_o] \quad (2.9)$$

where  ${}^c\mathbf{i}_o$ ,  ${}^c\mathbf{j}_o$ ,  ${}^c\mathbf{k}_o$  are the unit vectors of the x, y and z axes of the ORF, respectively, projected onto the coordinates of the CRF.

The DCM can also be parametrized by the attitude quaternion,  $\mathbf{q}_{co}$ , as

$$\mathbf{R}_{co} = \begin{bmatrix} q_1^2 - q_2^2 - q_3^2 + q_4^2 & 2(q_1q_2 + q_3q_4) & 2(q_1q_3 - q_2q_4) \\ 2(q_1q_2 - q_3q_4) & -q_1^2 + q_2^2 - q_3^2 + q_4^2 & 2(q_2q_3 + q_1q_4) \\ 2(q_1q_3 + q_2q_4) & 2(q_2q_3 - q_1q_4) & -q_1^2 - q_2^2 + q_3^2 + q_4^2 \end{bmatrix} \quad (2.10)$$

Another way of expressing a DCM in terms of an attitude quaternion is

$$\mathbf{R}(\mathbf{q}) = (q_4^2 - \mathbf{q}_v^T \mathbf{q}_v) \mathbf{E}_{3 \times 3} + 2\mathbf{q}_v \mathbf{q}_v^T - 2q_4 [\mathbf{q}_v \times] \quad (2.11)$$

where  $[\mathbf{q}_v \times]$  is the skew-symmetric matrix defined as

$$[\mathbf{a} \times] = \begin{bmatrix} 0 & -a_3 & a_2 \\ a_3 & 0 & -a_1 \\ -a_2 & a_1 & 0 \end{bmatrix} \quad (2.12)$$

- **Addition and multiplication**

Addition is defined by the sum of the corresponding components

$$\mathbf{q} + \mathbf{p} = \mathbf{i}(q_1 + p_1) + \mathbf{j}(q_2 + p_2) + \mathbf{k}(q_3 + p_3) + (q_4 + p_4) \quad (2.13)$$

On the other hand, multiplication is more complex since the conditions in Eq. (2.5) must be met and commutative law does not apply. Multiplication of two quaternions  $\mathbf{q}$  and  $\mathbf{p}$  is the given by

$$\mathbf{q} \otimes \mathbf{p} = \begin{bmatrix} p_4 & p_3 & -p_2 & p_1 \\ -p_3 & p_4 & p_1 & p_2 \\ p_2 & -p_1 & p_4 & p_3 \\ -p_1 & -p_2 & -p_3 & p_4 \end{bmatrix} \begin{bmatrix} q_1 \\ q_2 \\ q_3 \\ q_4 \end{bmatrix} = \mathbf{R}(\mathbf{p}) \cdot \mathbf{q} \quad (2.14)$$

As aforementioned, quaternions provide simple methods for the calculation of successive rotations. In particular, the transformation from the ECI to the CRF can be expressed as the product of the quaternion describing the rotation from the ORF to the CRF,  $\mathbf{q}_{co}$ , and the quaternion describing the rotation from the ECI to the ORF,  $\mathbf{q}_{oi}$

$$\mathbf{q}_{ci} = \mathbf{q}_{co} \otimes \mathbf{q}_{oi} \quad (2.15)$$

## 2.4 Environment Modelling

Attitude simulation and prediction require a model of the environment surrounding the satellite. Sources of disturbance torques taken into account in this thesis include solar radiation pressure, aerodynamic drag and Earth's gravitational field. The information presented in this section is based on [16, 23]

### 2.4.1 Gravity-gradient Torque

One of the dominating external torques acting on a LEO spacecraft is due to a gravity-gradient. This gradient exists because of the variation in the Earth's gravitational force over the spacecraft body. It is worth noting that there would be no gravitational torque in a uniform gravitational field.

The gravity-gradient torque can be explicitly modelled as

$${}^c\mathbf{T}_{gg} = \frac{3\mu}{R_{cm}^3} ({}^c\hat{\mathbf{R}}_{cm} \times \mathbf{I} {}^c\hat{\mathbf{R}}_{cm}) \quad (2.16)$$

where  $\mu$  is the Earth's gravitational constant,  $R_{cm}$  is the distance from the satellite's center of gravity to the center of the Earth and  ${}^c\hat{\mathbf{R}}_{cm}$  is the local zenith vector.  $R_{cm}$  is regarded as constant for the orbit involved. Since the zenith is equivalent

## Chapter 2. Satellite Modelling

to  $-{}^c\hat{\mathbf{o}}_3$  and  $\frac{3\mu}{R_{cm}^3} = \omega_0$ , where  $\omega_0$  is the orbital rate, the gravity gradient can now be expressed as

$${}^c\mathbf{T}_{gg} = \omega_0 ({}^c\hat{\mathbf{o}}_3 \times \mathbf{I} {}^c\hat{\mathbf{o}}_3) \quad (2.17)$$

Two interesting characteristics of the gravity-gradient may be deduced from Eq. (2.17): (a) the torque is normal to the local vertical, and (b) there is no resultant torque for a spherical symmetric spacecraft (its inertia tensor would be equal to a constant multiplied by an identity matrix and  ${}^c\hat{\mathbf{o}}_3 \times {}^c\hat{\mathbf{o}}_3 = \mathbf{0}$ ).

### 2.4.2 Solar Radiation Torque

The portion of the satellite's surface exposed to the Sun is subject to radiation pressure which results in a torque about the spacecraft's center of mass. Although other sources of electromagnetic radiation exist, such as solar radiation reflected by the Earth (albedo), direct solar illumination is the dominant and only one considered in this thesis.

The drag force exerted by the solar radiation is given by

$$\mathbf{F}_{sr} = -\frac{\mathbf{F}_{solar}}{c} C_k A_p \hat{\mathbf{r}}_{sun} \quad (2.18)$$

where  $c$  is the speed of light in vacuum,  $A_p$  is the projected area of the satellite exposed to the radiation,  $\hat{\mathbf{r}}_{sun}$  is the unit Sun vector in the CRF,  $\mathbf{F}_{solar}$  is the solar constant of Total Solar Irradiance (TSI) and  $C_k$  is a coefficient used to specify the outer material of the satellite.

A TSI of 1366 W/m<sup>2</sup> has been chosen based on [24]. For the value of the coefficient  $C_k$ ,  $C_k = 1$  implies a perfect absorbent material,  $C_k > 1$  a reflecting material and  $0 \leq C_k \leq 2$  [23]. A typical value of  $C_k = 1.5$  has been used for this thesis.

The resultant torque on the satellite  $T_{sr}$  is then given by the following cross product

$$\mathbf{T}_{sr} = \mathbf{r}_{cp} \times \mathbf{F}_{sr} \quad (2.19)$$

where  $\mathbf{r}_{cp}$  is a vector from the center of mass (CoM) of the satellite to its center of pressure (CoP). The center of pressure is at the intersection of the line of action of the resultant radiation force and the plane passing through the center of mass of the satellite perpendicular to the line of action [23].

### 2.4.3 Aerodynamic Torque

An aerodynamic drag force originates from the interaction of the molecules in the upper atmosphere with the satellite's surface. This force can be modelled as an elastic impact without reflection.

If we assume that the satellite can be seen as a plane with area  $A_p$  then the drag force exerted on the satellite is given by

$$\mathbf{F}_{aero} = -\frac{1}{2} C_a \rho_a A_p \|\mathbf{v}_{sat}\|^2 \hat{\mathbf{v}}_{sat} \quad (2.20)$$

## 2.4. Environment Modelling

where  $C_a$  is the aerodynamic drag coefficient,  $\rho_a$  is the atmosphere density,  $\mathbf{v}_{sat}$  is the translational velocity vector of the satellite and  $\hat{\mathbf{v}}_{sat}$  is a unit vector in the direction of the latter.

The drag coefficient  $C_a$  is a function of the surface structure and the local angle of attack. For practical applications,  $C_a = 2$  is a good estimate. The expected atmospheric density  $\rho_a$  is not a constant value and can be expressed in function of the F10.7 index. This index gives an idea of the solar activity at the Earth's orbit since it is a measure of the noise level generated by the Sun at 10.7 cm wavelength [1]. Figure 2.5 shows the temporal variability of the F10.7 index and Fig. 2.6 displays atmospheric density values for different orbit heights as a function of this index. An average value of  $\rho_a = 1.5 \times 10^{-13} \text{ kg/m}^3$  is used for this thesis.

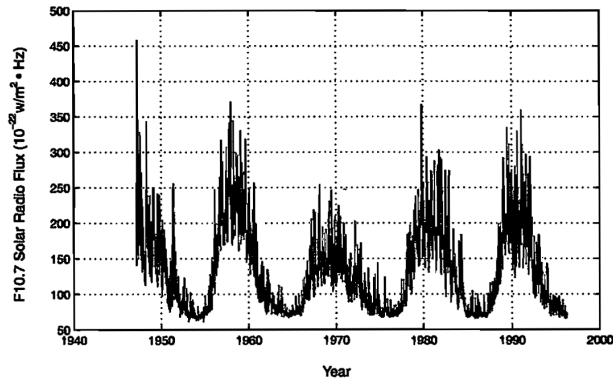


Figure 2.5: Observed daily radio flux at 10.7 cm [1].

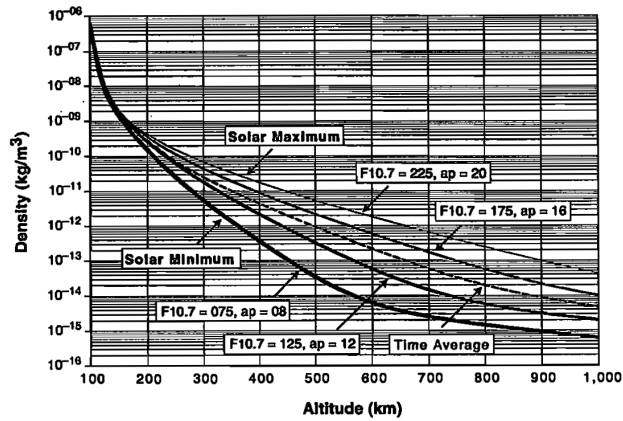


Figure 2.6: Density vs. altitude for various F10.7 values [1].

The resultant aerodynamic torque on the satellite  $T_{aero}$  is then given by the following cross product

$$\mathbf{T}_{aero} = \mathbf{r}_{cp} \times \mathbf{F}_{aero} \quad (2.21)$$

where  $\mathbf{r}_{cp}$  is a vector from the center of mass (CoM) of the satellite to its center of pressure (CoP).

### 2.4.4 Magnetic Field

The magnetic field surrounding the Earth is created by a combination of sources. More than 90% of this field is generated internally in the planet in the Earth's outer core. This portion of the geomagnetic field is referred to as the Main Field and it varies slowly in time. It can be grossly described as that of a bar magnet with its magnetic poles inside the Earth and its field lines extending into space (see Fig. 2.7). Current flowing inside the magnetosphere and the ionosphere cause variations in the intensity of the geomagnetic field on a much shorter time scale and as large as 10% of the Main Field [25].

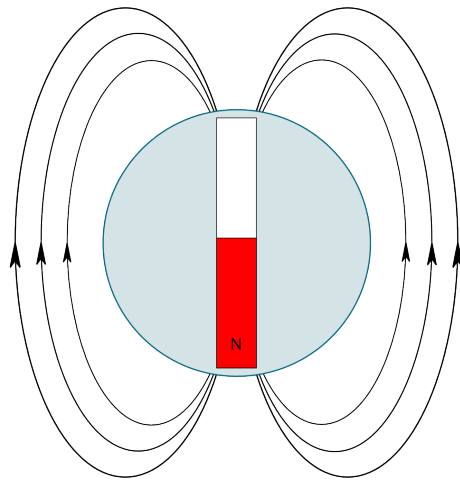


Figure 2.7: Earth's magnetic field modelled as a dipole magnet. N stands for the north pole of the dipole magnet.

The Main Field can be described with different mathematical models, in particular the International Geomagnetic Reference Field (IGRF) published by the International Association of Geomagnetism and Astronomy (IAGA) [26].

- IGRF

The IGRF model represents the Earth's magnetic field by a truncated spherical harmonic series (for more details see [23,26]). An implementation of the 11th generation of this model has been used for simulation.

Since 2000 the model truncation of the harmonics has been extended from degree 10 to 13 in order to better reflect the available measurements data. This involves a total of 210 coefficients. Currently, these coefficients are updated every five years and the latest generation of coefficients is valid for 2015-2020. The model is assumed to be linear over these five year intervals. Figure 2.8 shows a magnetic field strength contour chart for an orbit height of 630 km.

- Simple Geomagnetic Model

## 2.5. Equations of Motion

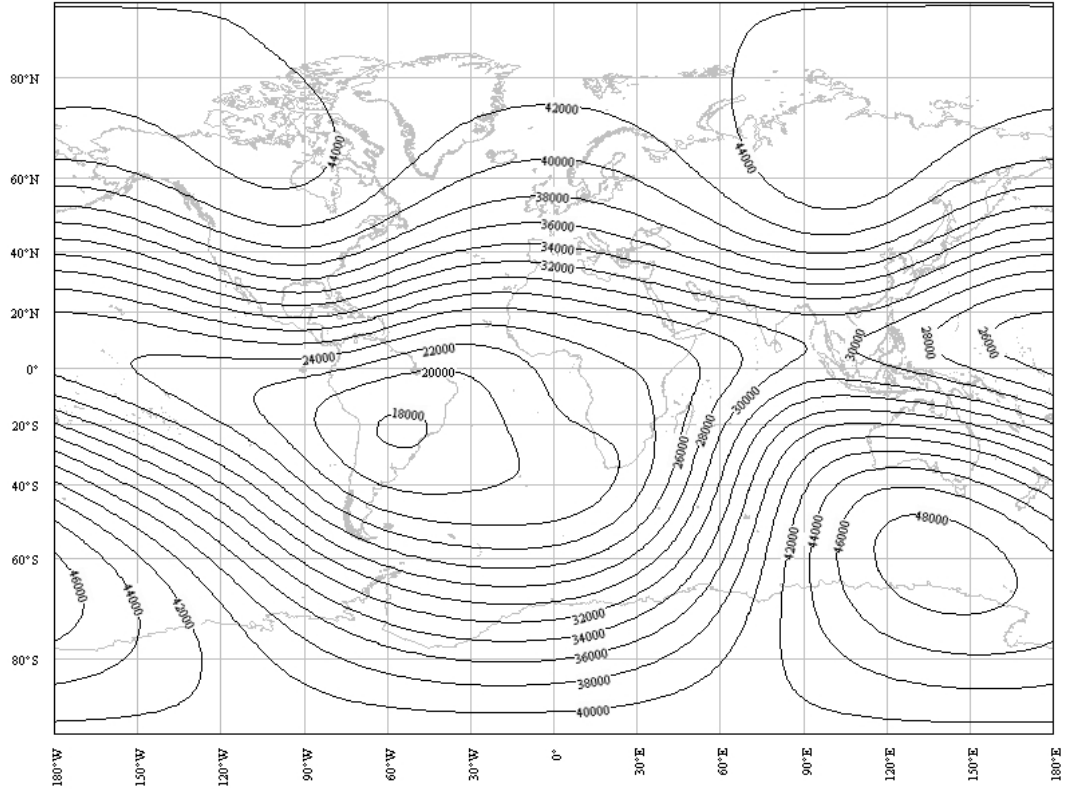


Figure 2.8: Total magnetic field strength contours in  $nT$ . The data was generated using the IGRF model for Jan 1st, 2010 for an orbit height of 630 km [13].

Time variations of the geomagnetic model can be approximated as being periodic, although true periodicity would hold if the orbit did not precess and the Earth did not rotate. A dipole approximation of the geomagnetic field, together with the assumptions of no Earth rotation and no orbit precession, yields the following periodic model expressed in the ORF as in [23]:

$${}^o\mathbf{B}_E = \frac{\mu_m}{R_{orb}^3} \begin{bmatrix} \cos \omega_0 t \cdot \sin i_m \\ -\cos i_m \\ 2 \sin \omega_0 t \cdot \sin i_m \end{bmatrix} \quad (2.22)$$

where  $i_m$  is the inclination of the orbit w.r.t. the magnetic equator,  $\mu_m$  is the total dipole strength of the Earth and  $R_{orb}$  is the orbital radius. As has been shown in [27], the accuracy of this simple model suffices for the analytical derivation of control laws.

## 2.5 Equations of Motion

The mathematical model of the satellite is based on the dynamic and kinematic equations of motion. The dynamics relate the development of angular velocities

## Chapter 2. Satellite Modelling

with the influence of external torques. The kinematic equations provide the relations between the time derivative of the attitude representation and the angular velocity.

The problem to be addressed is to solve the evolution of the attitude of the satellite over time. This process involves two stages. Firstly, the angular velocity of the body is found through time integration of the dynamic equations. Secondly, in order to determine the orientation, the kinematic equations are used.

Even though the satellite equations of motion describe the time dependent relative orientation between different coordinate frames, explicit notation indicating this time dependency has been omitted for the sake of simplicity. Results shown in this section are derived from [23].

### 2.5.1 Attitude Dynamics

The satellite is modelled as a rigid body with six degrees of freedom. Under these assumptions, Euler's law of angular momentum is applied to relate net torques acting about the CoM with the angular velocity of the control frame w.r.t the inertial frame. The resultant dynamic equation of motion is

$$\mathbf{I}^c \dot{\boldsymbol{\omega}}_{ci} = -{}^c\boldsymbol{\omega}_{ci} \times \mathbf{I}^c \boldsymbol{\omega}_{ci} + \mathbf{T}_{ctrl} + \mathbf{T}_{gg} + \mathbf{T}_{dist} \quad (2.23)$$

where  ${}^c\boldsymbol{\omega}_{ci}$  is the angular velocity of the control reference frame w.r.t the inertial reference frame,  $\mathbf{I}$  is the inertia tensor of the satellite,  $\mathbf{T}_{ctrl}$  is the control torque applied by the electromagnetic actuators,  $\mathbf{T}_{gg}$  is the gravity gradient torque, and  $\mathbf{T}_{dist}$  is the torque applied by the disturbances. Although  $\mathbf{T}_{gg}$  can be considered as a component included in  $\mathbf{T}_{dist}$ , the former is considered apart in this section ( $\mathbf{T}_{dist} = \mathbf{T}_{sr} + \mathbf{T}_{aero}$  only), as keeping  $\mathbf{T}_{gg}$  separated from  $\mathbf{T}_{dist}$  proves useful when designing the control algorithm by previously linearizing the system equations (see Sections 2.7 and 4.2). The summand  ${}^c\boldsymbol{\omega}_{ci} \times \mathbf{I}^c \boldsymbol{\omega}_{ci}$  represents the cross coupling between the components of the angular velocity vector. It arises due to the fact that dynamics are described in a rotating reference frame.

An important remark about the equation is the fact that it is expressed in the CRF. This is due to the fact that the inertia tensor of the satellite remains constant if expressed in a frame fixed to the body of the satellite. Moreover, expressing the inertia tensor in the CRF simplifies some calculations, since by definition the inertia tensor is a diagonal matrix if seen under this coordinate system.

### 2.5.2 Control Torque

The control torque acting on the satellite is generated by the interaction between the local geomagnetic field and the magnetorquer current  $i_{coil}$ , which gives rise to a magnetic moment  $\mathbf{m}$

$$\mathbf{m} = N_{coil} A_{coil} i_{coil} \hat{\mathbf{n}} \quad (2.24)$$

where  $A_{coil}$  is the area of the coil,  $N_{coil}$  is the number of windings of the coil and  $\hat{\mathbf{n}}$  is a unit vector normal to the plane defined by the coil and with the positive direction defined according to the direction of the current in the coil.

## 2.5. Equations of Motion

Since the electromagnetic coils are placed perpendicularly to each of the axes of the BRF, the resultant moment vector is given in the same coordinate system. Thus, a rotation matrix is needed to transform the vector from the BRF to the CRF

$${}^c\mathbf{m} = \mathbf{R}_{co} {}^b\mathbf{m} \quad (2.25)$$

The magnetic torque equation is given by

$${}^c\mathbf{T}_{ctrl} = {}^c\mathbf{m} \times {}^c\mathbf{B}_E \quad (2.26)$$

where  ${}^c\mathbf{B}_E$  is the geomagnetic field in the CRF. It can be deduced from Eq. (2.26) that the control torque always lies perpendicular to the geomagnetic field, never parallel. Regarding this fact, a mapping of the control vector can be introduced in order to achieve a more power efficient control law. This method was first proposed in [28]. The idea behind this power optimality method is as follows: since the component of the magnetic moment which is parallel to the geomagnetic field does not contribute to the generated control torque, it would be desirable that the original control signal  $\mathbf{u}$  was mapped to a new control signal  $\mathbf{m}$  which possessed no parallel components.

$${}^c\mathbf{u} \mapsto {}^c\mathbf{m} : {}^c\mathbf{m} = {}^c\mathbf{u} \times {}^c\mathbf{B}_E = -[{}^c\mathbf{B}_E \times] {}^c\mathbf{u} \quad (2.27)$$

Then the magnetic torque vector can be expressed in terms of the new control vector  $\mathbf{u}$  as

$$\begin{aligned} \mathbf{T}_{ctrl} &= (\mathbf{u} \times {}^c\mathbf{B}_E) \times {}^c\mathbf{B}_E \\ &= \mathbf{G}(t)\mathbf{u} \end{aligned} \quad (2.28)$$

### 2.5.3 Attitude Kinematics

The kinematics describes the orientation of the satellite's body in space, which is possible to obtain through integration of the angular velocity. The kinematic equations can be expressed separately for the vector and scalar parts of the attitude quaternion

$$\begin{aligned} \dot{\mathbf{q}}_v &= \frac{1}{2} {}^c\boldsymbol{\omega}_{co} q_4 - \frac{1}{2} {}^c\boldsymbol{\omega}_{co} \times \mathbf{q}_v \\ \dot{q}_4 &= -\frac{1}{2} {}^c\boldsymbol{\omega}_{co} \cdot \mathbf{q}_v \end{aligned} \quad (2.29)$$

although a combined expression is also used

$$\dot{\mathbf{q}} = \frac{1}{2} \cdot \begin{bmatrix} q_4 \mathbf{E}_{3 \times 3} + [\mathbf{q}_v \times] \\ -\mathbf{q}_v^T \end{bmatrix} \cdot {}^c\boldsymbol{\omega}_{co} \quad (2.30)$$

It is convenient to represent the above equation with an equivalent bilinear form

$$\dot{\mathbf{q}} = \frac{1}{2} \mathbf{W}({}^c\boldsymbol{\omega}_{co}) \cdot \mathbf{q} \quad (2.31)$$

## Chapter 2. Satellite Modelling

where

$$\mathbf{W}({}^c\boldsymbol{\omega}_{co}) = \begin{bmatrix} 0 & {}^c\boldsymbol{\omega}_{co3} & -{}^c\boldsymbol{\omega}_{co2} & {}^c\boldsymbol{\omega}_{co1} \\ -{}^c\boldsymbol{\omega}_{co3} & 0 & {}^c\boldsymbol{\omega}_{co1} & {}^c\boldsymbol{\omega}_{co2} \\ {}^c\boldsymbol{\omega}_{co2} & -{}^c\boldsymbol{\omega}_{co1} & 0 & {}^c\boldsymbol{\omega}_{co3} \\ -{}^c\boldsymbol{\omega}_{co1} & -{}^c\boldsymbol{\omega}_{co2} & -{}^c\boldsymbol{\omega}_{co3} & 0 \end{bmatrix} \quad (2.32)$$

The angular velocity of the CRF relative to the ORF can be written as

$$\begin{aligned} {}^c\boldsymbol{\omega}_{co} &= {}^c\boldsymbol{\omega}_{ci} - {}^c\boldsymbol{\omega}_{oi} \\ &= {}^c\boldsymbol{\omega}_{ci} - (-\omega_0 {}^c\hat{\mathbf{o}}_2) \end{aligned} \quad (2.33)$$

Equation (2.31) represents the rate of change for  $\dot{\mathbf{q}}_{co}$ , but the rate of change of  $\dot{\mathbf{q}}_{ci}$  can also be expressed with the correspondent equation:

$$\dot{\mathbf{q}}_{ci} = \frac{1}{2} \mathbf{W}({}^c\boldsymbol{\omega}_{ci}) \cdot \mathbf{q}_{ci} \quad (2.34)$$

where  $\mathbf{W}(\cdot)$  is as defined in Eq. (2.32).

## 2.6 Controllability

Attitude control by magnetic actuation possesses a serious constraint: not all directions are controllable at any given time, i.e. the system is fundamentally underactuated. As expressed in Eq. (2.26), the control torque—produced by the interaction of the geomagnetic field with the magnetic field generated by the magnetorquers—is always perpendicular to the local direction of the geomagnetic field vector. Notwithstanding, 3-axis magnetic stabilization is possible if the considered orbit sees a variation of the magnetic field which is sufficient to guarantee the stabilizability of the spacecraft [29]. Since the considered orbit has a high inclination, as the satellite travels along it the geomagnetic field varies its orientation in the ORF. So considered along an orbit, the system can be regarded as controllable on average, in spite of the previously mentioned underactuation. As an instance, the yaw is not controllable over the poles, but it is over the equator, as can be seen in Fig. 2.9.

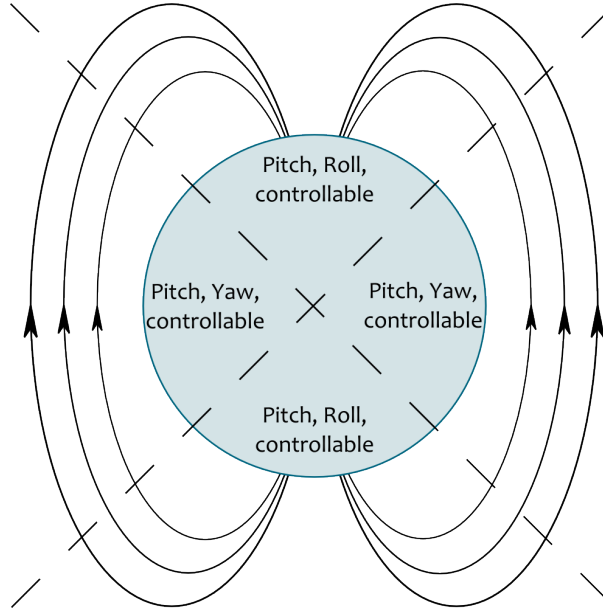


Figure 2.9: Fundamental underactuation. Not all degrees of freedom may be manipulated at any given time.

## 2.7 Linearization

A linearized model of the satellite will be used for the application of linear systems theory and control laws in Section 4.2. In this context, the effects of the disturbance torques will be disregarded—except for the gravity-gradient—, thus, no linearization of those will be presented in this section. The objective of the following section is to find a set of equations which are linear in the state variables  $\mathbf{x} = [\mathbf{q}^T \dot{\mathbf{q}}^T]^T = [\mathbf{q}_{co}^T \dot{\mathbf{q}}_{co}^T]^T$ .

AntelSat is a nadir-pointing satellite. For this reason, the satellite motion is considered in a neighbourhood of the ORF, i.e.  $\mathbf{q}_{equi} = [0001]^T$  and  ${}^c\boldsymbol{\omega}_{co,equi} = [000]^T$ .

To begin with the linearization of the satellite equations, the way that the state vector components are linearized must be defined. For the case of the attitude quaternion, the assumption of small deviations from the reference are considered and for this reason

$$\delta\mathbf{q} = \begin{bmatrix} e_1 \sin(\frac{\delta\phi}{2}) \\ e_2 \sin(\frac{\delta\phi}{2}) \\ e_3 \sin(\frac{\delta\phi}{2}) \\ \cos(\frac{\delta\phi}{2}) \end{bmatrix} \approx \begin{bmatrix} \delta q_1 \\ \delta q_2 \\ \delta q_3 \\ 1 \end{bmatrix} = \begin{bmatrix} \delta\mathbf{q}_v \\ 1 \end{bmatrix} \quad (2.35)$$

Linearization of the angular velocity is based on a first-order approximation of the Taylor series in Eq. (2.33):

$$\begin{aligned} {}^c\boldsymbol{\omega}_{ci} &= \mathbf{R}_{co} \cdot [0 - \omega_0 0]^T + \delta\boldsymbol{\omega} \\ \Rightarrow \delta\boldsymbol{\omega} &= {}^c\boldsymbol{\omega}_{ci} + \omega_0 {}^c\hat{\mathbf{o}}_2 \end{aligned} \quad (2.36)$$

## Chapter 2. Satellite Modelling

where  $\mathbf{R}_{co} = [{}^c\hat{\mathbf{o}}_1 \ {}^c\hat{\mathbf{o}}_2 \ {}^c\hat{\mathbf{o}}_3]$  is the rotation matrix from the ORF to CRF and

$${}^c\hat{\mathbf{o}}_2 = \begin{bmatrix} 2(q_1q_2 + q_3q_4) \\ 1 - 2(q_1^2 + q_3^2) \\ 2(q_2q_3 - q_1q_4) \end{bmatrix} \quad (2.37)$$

### 2.7.1 Linearized Kinematics

Combining Eqs. (2.30) and (2.36) yields

$$\begin{bmatrix} \dot{q}_1 \\ \dot{q}_2 \\ \dot{q}_3 \\ \dot{q}_4 \end{bmatrix} = \frac{1}{2} \begin{bmatrix} q_4 & -q_3 & q_2 \\ q_3 & q_4 & -q_1 \\ -q_2 & q_1 & q_4 \\ -q_1 & -q_2 & -q_3 \end{bmatrix} ({}^c\boldsymbol{\omega}_{ci} + \omega_0 {}^c\hat{\mathbf{o}}_2) \quad (2.38)$$

Expanding the above equation and keeping terms up to a first-order gives

$$\begin{bmatrix} \delta\dot{q}_1 \\ \delta\dot{q}_2 \\ \delta\dot{q}_3 \end{bmatrix} = \frac{1}{2} \begin{bmatrix} \delta\omega_1 + 2\omega_0 \delta q_3 \\ \delta\omega_2 + \omega_0 \\ \delta\omega_3 - 2\omega_0 \delta q_1 \end{bmatrix} \quad (2.39)$$

where  $\delta\boldsymbol{\omega} = [\delta\omega_1 \ \delta\omega_2 \ \delta\omega_3]^T$ .

For the angular velocity of the control frame w.r.t. the orbital frame, Eq. (2.29) is considered and rewritten

$$\dot{\mathbf{q}}_v = \frac{1}{2} [q_4 + [\mathbf{q}_v \times]] {}^c\boldsymbol{\omega}_{co} \approx \frac{1}{2} {}^c\boldsymbol{\omega}_{co} \Rightarrow \delta\boldsymbol{\omega} \approx 2 \delta\dot{\mathbf{q}}_v \quad (2.40)$$

Combining Eqs. (2.29) and (2.39) and differentiating with respect to time we obtain

$$\delta\dot{\boldsymbol{\omega}} = 2 \delta\ddot{\mathbf{q}}_v - 2\omega_0 \begin{bmatrix} \delta\dot{q}_3 \\ 0 \\ -\delta\dot{q}_1 \end{bmatrix} \quad (2.41)$$

### 2.7.2 Linearized Dynamics

Rewriting Eq. (2.23) and combining Eqs. (2.17) and (2.28) yields

$${}^c\boldsymbol{\omega}_{ci} = \mathbf{I}^{-1} [-{}^c\boldsymbol{\omega}_{ci} \times \mathbf{I} \cdot {}^c\boldsymbol{\omega}_{ci} + 3\omega_0^2 {}^c\hat{\mathbf{o}}_3 \times {}^c\hat{\mathbf{o}}_3 + \mathbf{G}(t)\mathbf{u}] \quad (2.42)$$

The above equation is divided into the contributions of the cross coupling, the gravity gradient torque, and the control torque. The disturbance torque  $\mathbf{T}_{dist}$  depends on the satellite position relative to the Sun and Earth and will be disregarded in the linear model.

- Linearization of Cross Coupling

$$\mathbf{I}^{-1}[-{}^c\boldsymbol{\omega}_{ci} \times \mathbf{I} \cdot {}^c\boldsymbol{\omega}_{ci}] \approx \omega_0 \begin{bmatrix} -2\sigma_1(\delta\dot{q}_3 + \omega_0 \delta q_1) \\ 0 \\ 2\sigma_3(\delta\dot{q}_1 - \omega_0 \delta q_3) \end{bmatrix} \quad (2.43)$$

where

$$\sigma_1 = \frac{I_2 - I_3}{I_1}, \quad \sigma_2 = \frac{I_1 - I_3}{I_2}, \quad \sigma_3 = \frac{I_2 - I_1}{I_3} \quad (2.44)$$

- Linearization of Gravity-Gradient

$$\begin{aligned} \mathbf{I}^{-1}[3\omega_0^2 {}^c\hat{\mathbf{o}}_3 \times {}^c\hat{\mathbf{o}}_3] &= 6\omega_0^2 \begin{bmatrix} \sigma_1 (q_1 q_4 + q_2 q_3)(q_1^2 + q_2^2 - q_3^2 - q_4^2) \\ -\sigma_2 (q_1 q_3 - q_2 q_4)(q_1^2 + q_2^2 - q_3^2 - q_4^2) \\ 2\sigma_3 (q_1 q_4 + q_2 q_3)(q_1 q_3 - q_2 q_4) \end{bmatrix} \\ &\approx 6\omega_0^2 \begin{bmatrix} -\sigma_1 \delta q_1 \\ \sigma_2 \delta q_2 \\ 0 \end{bmatrix} \end{aligned} \quad (2.45)$$

- Linearization of Control Torque

$${}^c\mathbf{T}_{ctrl} = {}^c\mathbf{m} \times (\mathbf{R}_{co} \cdot {}^o\mathbf{B}_E) \approx {}^c\mathbf{m} \times {}^o\mathbf{B}_E - 2 {}^c\mathbf{m} \times (\delta\mathbf{q} \times {}^o\mathbf{B}_E) \quad (2.46)$$

When linear feedback is implemented ( ${}^c\mathbf{m} = \mathbf{K} \cdot \mathbf{x}$ ), the second summand becomes a term of second-order approximation and it can be disregarded.

Thus, the linearization of the control torque yields

$${}^c\mathbf{T}_{ctrl} \approx {}^c\mathbf{m} \times {}^o\mathbf{B}_E \quad (2.47)$$

Combining Eq. (2.47) with the power optimality concept introduced in Eq. (2.28) gives

$${}^c\mathbf{T}_{ctrl} \approx [{}^o\mathbf{B}_E \times][{}^o\mathbf{B}_E \times] \mathbf{u} \quad (2.48)$$

Regarding Eq. (2.22) the double product of the skew matrices above can be expressed as

$$[{}^o\mathbf{B}_E \times][{}^o\mathbf{B}_E \times] = -\frac{\mu_m^2}{R_{orb}^6} \mathbf{H}(t) \quad (2.49)$$

## Chapter 2. Satellite Modelling

where the entries  $h_{ij}(t)$  of the matrix  $\mathbf{H}(t)$  are given by

$$\begin{aligned}
 h_{11}(t) &= 4 \sin^2 i_m \sin^2 \omega_0 t + \cos^2 i_m \\
 h_{22}(t) &= (\cos^2 \omega_0 t + 4 \sin^2 \omega_0 t) \sin^2 i_m \\
 h_{33}(t) &= \sin^2 i_m \cos^2 \omega_0 t + \cos^2 i_m \\
 h_{12}(t) &= h_{21}(t) = -0.5 \sin 2i_m \cos \omega_0 t \\
 h_{13}(t) &= h_{31}(t) = -\sin^2 i_m \sin 2\omega_0 t \\
 h_{23}(t) &= h_{32}(t) = -\sin 2i_m \sin \omega_0 t
 \end{aligned} \tag{2.50}$$

### 2.7.3 Complete Linearized System

By gathering the results from previous subsections into Eq. (2.42) we obtain

$$2 \delta \ddot{\mathbf{q}}_v - 2\omega_0 \begin{bmatrix} \delta \dot{q}_3 \\ 0 \\ -\delta \dot{q}_1 \end{bmatrix} = 2\omega_0 \begin{bmatrix} -\sigma_1(\delta \dot{q}_3 + \omega_0 \delta q_1) \\ 0 \\ \sigma_3(\delta \dot{q}_1 - \omega_0 \delta q_3) \end{bmatrix} + 6\omega_0^2 \begin{bmatrix} -\sigma_1 \delta q_1 \\ \sigma_2 \delta q_2 \\ 0 \end{bmatrix} - \frac{\mu_m^2}{R_{orb}^6} \mathbf{I}^{-1} \mathbf{H}(t) \mathbf{u} \tag{2.51}$$

Let  $\mathbf{x} = [\delta \mathbf{q}_v^T \ \delta \dot{\mathbf{q}}_v^T]^T$  and  $\mathbf{u}$  be the state variable and the control signal, respectively. Then, by rearranging terms in the equation above, the linearized equations of motion can be written as

$$\dot{\mathbf{x}} = \mathbf{A} \mathbf{x} + \mathbf{B}(t) \mathbf{u} \tag{2.52}$$

where

$$\mathbf{A} = \begin{bmatrix} \mathbf{0}_{3 \times 3} & \mathbf{E}_{3 \times 3} \\ \mathbf{A}_1 & \mathbf{A}_2 \end{bmatrix}, \quad \mathbf{B}(t) = -\frac{\mu_m^2}{2R_{orb}^6} \begin{bmatrix} \mathbf{0}_{3 \times 3} \\ \mathbf{I}^{-1} \mathbf{H}(t) \end{bmatrix} \tag{2.53}$$

where

$$\mathbf{A}_1 = \begin{bmatrix} -4\omega_0^2 \sigma_1 & 0 & 0 \\ 0 & 3\omega_0^2 \sigma_2 & 0 \\ 0 & 0 & -\omega_0^2 \sigma_3 \end{bmatrix}, \quad \mathbf{A}_2 = \begin{bmatrix} 0 & 0 & \omega_0(1 - \sigma_1) \\ 0 & 0 & 0 \\ \omega_0(\sigma_3 - 1) & 0 & 0 \end{bmatrix}$$

### 2.7.4 Averaged Linearized System

In the following subsection, a linear time-invariant model of the satellite will be presented. This model consists of a set of averaged linear state equations derived from the model introduced in Section 2.7.3. In Section 4.2.1, this model will be used to derive an attitude controller and the relevant theory about averaged systems will be presented.

The model presented in Eq. (2.52) clearly corresponds to a time dependent system as the entries of the matrix  $\mathbf{B}(t)$  vary according to the position of the spacecraft on its orbit. As seen in Section 2.4.4,  ${}^o\mathbf{B}_E(t)$  can be considered as a periodic function, hence,  $\mathbf{B}(t)$  can also be regarded as periodic.

## 2.8. Summary

Let  $\mathbf{x} = [\delta\mathbf{q}_v^T \ \delta\dot{\mathbf{q}}_v^T]^T$  and  $\mathbf{u}$  be the state variable and the control signal, respectively. Then, the averaged linearized state equations can be written as

$$\dot{\mathbf{x}} = \mathbf{A}\mathbf{x} + \bar{\mathbf{B}}\mathbf{u} \quad (2.54)$$

where  $\mathbf{A}$  is defined in Eq. (2.53) and  $\bar{\mathbf{B}}$  is

$$\bar{\mathbf{B}} = -\frac{\mu_m^2}{2R_{orb}^6} \begin{bmatrix} \mathbf{0}_{3 \times 3} \\ \mathbf{I}^{-1}\bar{\mathbf{H}} \end{bmatrix} \quad (2.55)$$

where  $\bar{\mathbf{H}}$  is the orbit average of the control input matrix  $\mathbf{H}(t)$  and the entries  $h_{ij}(t)$  of the latter are as in Eq. (2.50)

The orbit average of  $\mathbf{H}(t)$  is defined as

$$\bar{\mathbf{H}} = \frac{1}{T} \int_0^T \mathbf{H}(t) dt \quad (2.56)$$

Although it is possible to numerically integrate  $\mathbf{H}(t)$  in order to find a solution for Eq. (2.56), an analytical approach is as a more sensible option. This analytical approach simplifies the calculation of the averaged model for systems on low eccentricity orbits. This method was first proposed in [6].

Noting that

$$\int_0^T \sin^2(\omega_0 t) dt = \int_0^T \cos^2(\omega_0 t) dt = \frac{1}{2}, \quad \int_0^T \sin(2\omega_0 t) dt = 0$$

$\bar{\mathbf{H}}$  can be computed as

$$\bar{\mathbf{H}} = \text{diag} \left( (1 + \sin^2 i_m) \left( \frac{5}{2} \sin^2 i_m \right) \left( 1 - \frac{1}{2} \sin^2 i_m \right) \right)^T$$

## 2.8 Summary

In this chapter, a description of a Keplerian orbit of a satellite around the Earth was presented, along with its description in the Two Line Element format. Moreover, coordinate systems and attitude parametrizations were introduced. Models for the equations of motion of the satellite and the environment are included. Finally, the chapter presents the necessary theory to develop the attitude control algorithms.

This page has been intentionally left blank.

# Chapter 3

## Attitude Determination

In order to control the spacecraft, its attitude needs to be first estimated so that this estimation can be used as input for the attitude controller. Determining the spacecraft attitude implies completely specifying the attitude matrix.

A possible means of estimating the attitude of a satellite is by using unit vector observations. Under these conditions, an optimal and fast algorithm for quaternion estimation has been chosen to carry out the attitude determination task: the QUaternion ESTimator (QUEST) [30]. Like many other methods, it uses two vector measurements: the unit vector to the Sun and the Earth's magnetic field vector.

Another approach is the use of statistical filters. Kalman filters have been widely used in aerospace projects, especially extended Kalman filters (EKF). Recently, a number of different projects have approached the attitude determination strategy with unscented Kalman filters (UKF) [31]. UKF is a relatively new technique that is able to handle the nonlinear dynamics behaviour.

This chapter presents the two different attitude determination methods. Section 3.1 introduces the deterministic method, i.e. the optimal quaternion estimation method. Section 3.2 then follows with the development of the attitude estimator based on an unscented Kalman filter. Lastly, Section 3.3 closes the chapter with simulations showing the performance of the different methods.

### 3.1 Deterministic Method

#### 3.1.1 Introduction

As many other methods, QUEST uses two vector measurements: the unit vector to the Sun and the Earth's magnetic field vector. The onboard Sun sensors and magnetometer are used to measure these vectors, respectively. When information from one of the sensors is regarded with higher confidence compared to the information from the remaining sensor, this algorithm reduces to the TRIAD algorithm [23]. The inputs needed by the algorithm are two antiparallel reference vectors and two antiparallel measured vectors. In order to compute the reference vectors, actual

## Chapter 3. Attitude Determination

time and position of the spacecraft are needed for running the models. Position is computed using an onboard orbit propagator, which requires the time and the orbital parameters included in the Two Line Element (TLE, see Section 2.1). Figure 3.1 summarizes the above information. From this point, a set of data acquired from the sensors is compared to an estimated set of data from onboard models. It is a requirement having two antiparallel observations and for this reason the attitude cannot be determined with this method during the eclipse phase, since a reliable Sun vector measurement cannot be obtained from the Sun sensors.

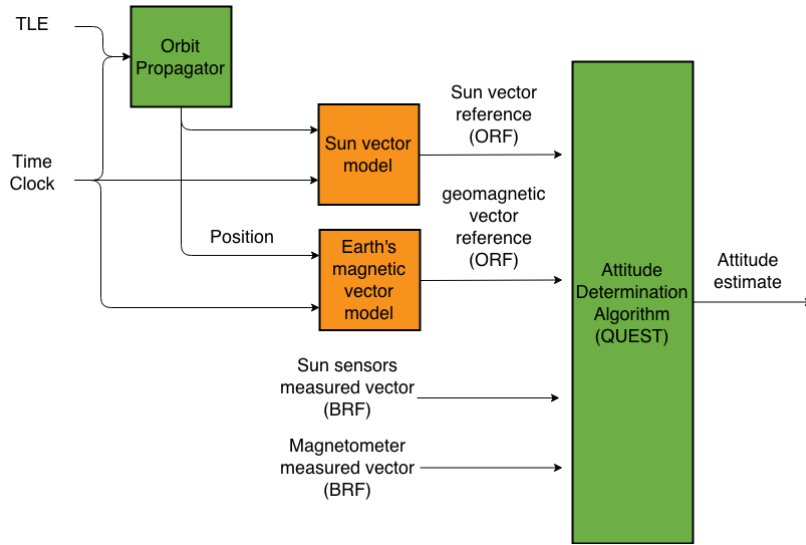


Figure 3.1: Deterministic Attitude Determination Process Diagram

### 3.1.2 Wahba's problem

Given a set of  $n \geq 2$  vector measurements  $\mathbf{b}_i$  in the body system (BRF), a possible choice for an optimal attitude matrix  $\mathbf{A}$  is that which minimizes the loss function

$$J(\mathbf{A}) = \sum_{i=1}^n w_i |\mathbf{b}_i - \mathbf{A}\mathbf{r}_i|^2 \quad (3.1)$$

where  $w_i$  is an optional set of weights for each observation and  $\mathbf{r}_i$  is the corresponding set of vectors in the reference coordinate system (ORF in this case). This problem is known as Wahba's problem after Grace Wahba who first posed the problem in 1965 [30].

It is possible to rewrite the loss function in the following way

$$J(\mathbf{A}) = -2 \sum_{i=1}^n \mathbf{W}_i \mathbf{A} \mathbf{V}_i + \text{constant terms} \quad (3.2)$$

where vectors  $\mathbf{W}_i$  and  $\mathbf{V}_i$  are defined as

$$\mathbf{W}_i = \sqrt{w_i} \mathbf{b}_i; \quad \mathbf{V}_i = \sqrt{w_i} \mathbf{r}_i; \quad (3.3)$$

### 3.1. Deterministic Method

It is clear that the loss function  $J(\mathbf{A})$  is a minimum when

$$\tilde{J}(\mathbf{A}) = \sum_{i=1}^n \mathbf{W}_i \mathbf{A} \mathbf{V}_i \equiv \text{trace}(\mathbf{W}^T \mathbf{A} \mathbf{V}) \quad (3.4)$$

is a maximum, where  $\mathbf{W}$  and  $\mathbf{V}$  are (3 x n) matrices defined by

$$\begin{aligned} \mathbf{W} &\equiv [\mathbf{W}_1 \vdots \mathbf{W}_2 \vdots \dots \vdots \mathbf{W}_n] \\ \mathbf{V} &\equiv [\mathbf{V}_1 \vdots \mathbf{V}_2 \vdots \dots \vdots \mathbf{V}_n] \end{aligned} \quad (3.5)$$

Then, the aim is to find an attitude matrix  $\mathbf{A}$  which maximizes Eq. (3.4). In order to do this, we consider the parametrization of  $\mathbf{A}$  in terms of the attitude quaternion  $\mathbf{q} = [\mathbf{q}_v^T q_4]^T$ , such as in Eq. (2.11),

$$\mathbf{A}(\mathbf{q}) = (q_4^2 - \mathbf{q}_v^T \mathbf{q}_v) \mathbf{E}_{3 \times 3} + 2\mathbf{q}_v \mathbf{q}_v^T - 2q_4 [\mathbf{q}_v \times] \quad (3.6)$$

where  $[\mathbf{q}_v \times]$  is the skew-symmetric matrix of  $\mathbf{q}_v$ , as defined in Eq. (2.12).

Substitution of Eq. (3.6) into Eq. (3.4) and considerable matrix algebra gives a convenient form for the modified loss function [23]

$$\tilde{J}(\mathbf{q}) = \mathbf{q}^T \mathbf{K} \mathbf{q} \quad (3.7)$$

where  $\mathbf{K}$  is a (4 x 4) matrix given by

$$\mathbf{K} \equiv \begin{bmatrix} \mathbf{B} + \mathbf{B}^T - \mathbf{E}_{3 \times 3} \text{trace}(\mathbf{B}) & \sum_i w_i \mathbf{b}_i \times \mathbf{r}_i \\ \sum_i w_i (\mathbf{b}_i \times \mathbf{r}_i)^T & \text{trace}(\mathbf{B}) \end{bmatrix} \quad (3.8)$$

Considering the normalization constraint  $\mathbf{q}^T \mathbf{q} = 1$ , the extrema of  $\tilde{J}$  can be found by applying the method of Lagrange multipliers. Let  $g$  be a new function defined by

$$g(\mathbf{q}) = \mathbf{q}^T \mathbf{K} \mathbf{q} - \lambda \mathbf{q}^T \mathbf{q} \quad (3.9)$$

where  $\lambda$  is the Lagrange multiplier.  $g(\mathbf{q})$  is maximized without constraint, but  $\lambda$  is chosen to satisfy the normalization constraint. After we differentiate Eq. (3.9) w.r.t.  $\mathbf{q}^T$  and set the result equal to zero, we obtain the eigenvector equation

$$\mathbf{K} \mathbf{q} = \lambda \mathbf{q} \quad (3.10)$$

It follows that the quaternion which parameterizes the optimal attitude matrix—in the sense of Eq. (3.1)—is an eigenvector of  $\mathbf{K}$ . Substituting Eq. (3.10) into Eq. (3.7) yields

$$\tilde{J}(\mathbf{q}) = \mathbf{q}^T \mathbf{K} \mathbf{q} = \lambda \mathbf{q}^T \mathbf{q} = \lambda \quad (3.11)$$

Thus, the optimal quaternion is found if the normalized eigenvector corresponding to the largest eigenvalue is chosen. In the case when the two largest eigenvalues of  $\mathbf{K}$  are equal, there will be no unique solution. However, it can be shown that if the measurement vectors are not collinear, these eigenvalues are distinct and thus the procedure yields three-axis attitude [23].

## Chapter 3. Attitude Determination

This result is known as the q-method. Nonetheless, finding a numerical solution for the eigenproblem could pose a computation burden. For this reason, there exist some variations on the q-method which avoid the need for computing eigenvectors. The optimal QUaternion ESTimation (QuEst) method described in the following subsection finds a numerically friendly approximation to the largest eigenvalue of  $\mathbf{K}$ .

### 3.1.3 Optimal Quaternion Estimation Method

Given the measurement vectors from the Sun sensor  ${}^b\mathbf{s}$  and the magnetometer  ${}^b\mathbf{b}$  and the respective reference vectors in the ORF,  ${}^o\mathbf{s}$  and  ${}^o\mathbf{b}$ , it is useful to define the normalized cross product

$$\begin{aligned}\mathbf{p}_B &\equiv \frac{{}^b\mathbf{b} \times {}^b\mathbf{s}}{|{}^b\mathbf{b} \times {}^b\mathbf{s}|} \\ \mathbf{p}_O &\equiv \frac{{}^o\mathbf{b} \times {}^o\mathbf{s}}{|{}^o\mathbf{b} \times {}^o\mathbf{s}|}\end{aligned}\quad (3.12)$$

It is noteworthy that  $\mathbf{p}_B$  or  $\mathbf{p}_O$  is undefined if the reference or observed vectors, respectively, are collinear.

As it is shown in [30], the optimal attitude quaternion estimate is obtained by the following expression

$$\mathbf{q}_{opt} = \begin{cases} \frac{1}{2\sqrt{\gamma(\gamma+\alpha)(1+\mathbf{p}_B \cdot \mathbf{p}_O)}} \begin{bmatrix} (\gamma + \alpha)(\mathbf{p}_B \times \mathbf{p}_O) + \beta(\mathbf{p}_B + \mathbf{p}_O) \\ (\gamma + \alpha)(1 + \mathbf{p}_B \cdot \mathbf{p}_O) \end{bmatrix} & \text{for } \alpha \geq 0 \\ \frac{1}{2\sqrt{\gamma(\gamma-\alpha)(1+\mathbf{p}_B \cdot \mathbf{p}_O)}} \begin{bmatrix} (\gamma - \alpha)(\mathbf{p}_B + \mathbf{p}_O) + \beta(\mathbf{p}_B \times \mathbf{p}_O) \\ \beta(1 + \mathbf{p}_B \cdot \mathbf{p}_O) \end{bmatrix} & \text{for } \alpha \leq 0 \end{cases}\quad (3.13)$$

where

$$\begin{aligned}\alpha &= (1 + \mathbf{p}_B \cdot \mathbf{p}_O)(w_1 {}^b\mathbf{b} \cdot {}^o\mathbf{b} + w_2 {}^b\mathbf{s} \cdot {}^o\mathbf{s}) \\ &\quad + (\mathbf{p}_B \times \mathbf{p}_O) \cdot (w_1 {}^b\mathbf{b} \times {}^o\mathbf{b} + w_2 {}^b\mathbf{s} \times {}^o\mathbf{s}) \\ \beta &= (\mathbf{p}_B + \mathbf{p}_O) \cdot (w_1 {}^b\mathbf{b} \times {}^o\mathbf{b} + w_2 {}^b\mathbf{s} \times {}^o\mathbf{s}) \\ \gamma &= \sqrt{\alpha^2 + \beta^2}\end{aligned}\quad (3.14)$$

Note that since the reference and observed vectors are given in the orbital and body coordinate system, respectively, the resulting attitude quaternion is the one describing the rotation of the BRF with respect to the ORF,  $\mathbf{q}_{bo}$ .

The quaternion rate, which is used to determine the control action during nominal mode, is obtained by numerical differentiation of the quaternion estimates. Once the quaternion rate is computed, it is possible to obtain the angular velocity estimate, by applying the inverse kinematics equation, Eq. (2.30), i.e.

$${}^b\boldsymbol{\omega}_{bo} = 2(q_4 \mathbf{E}_{3 \times 3} - q_4 [\mathbf{q}_v \times] + \mathbf{q}_v \mathbf{q}_v^T) \cdot [\dot{\mathbf{q}}_v^T q_4]^T \quad (3.15)$$

## 3.2. Filtering Method

In order to mitigate the high frequency noise inherent in the differentiation process a digital filter is used

$$\begin{aligned}\boldsymbol{\omega}_{k,filtered} &= \alpha\boldsymbol{\omega}_k + (1 - \alpha)\boldsymbol{\omega}_{k-1} \\ \alpha &= \frac{T_s}{T_s + T_f}\end{aligned}\tag{3.16}$$

The constant  $T_s$  denotes the sampling time of the system and  $T_f$  is a filter time constant. For this implementation,  $T_f$  has been set to 60 seconds and the sampling time is one second.

Constants  $w_1$  and  $w_2$  reflect the relative confidence on measurements taken by the magnetometer and Sun sensors, respectively. Under these circumstances, and since the Sun sensors are not accurate sensors, the constants have been set to  $w_1 = 0.9$  and  $w_2 = 0.1$ .

## 3.2 Filtering Method

### 3.2.1 Introduction

Kalman filters have been widely used in aerospace projects, in particular extended Kalman filters (EKF). The Kalman Filter is an optimal filter for estimating a linear system. However, since most real-world systems are of a nonlinear nature, the EKF was developed to help account for those nonlinearities. The EKF tackles nonlinearities by linearizing the system about its last-known estimate assuming that the error incurred by neglecting the higher order terms is small in comparison to the first-order terms. This filter operates by approximating the state distribution as a Gaussian random variable (GRV) and then propagating it through the first-order linearization of the nonlinear system. For this reason, the EKF is a suboptimal nonlinear filter due to the truncation of the higher-order terms when linearizing the system [32].

Recently, a number of different projects have approached the attitude determination strategy with unscented Kalman filters (UKF) [31]. UKF is a relatively new technique that is able to handle the approximation problems intrinsically related to EKF. This more recent approach achieves significantly more accurate estimation results and faster convergence times. What is more, in certain situations—in particular when body angular rates are high and satellite dynamics turn highly nonlinear—an EKF based algorithm could never converge as the first-order approximation cannot adequately capture large errors. Even in these situations UKF is able to converge [33].

UKF is based on the unscented transformation, which relies on the assumption that approximating a Gaussian distribution is easier than approximating a nonlinear transformation [34]. One of the characteristic aspects of UKF is the introduction of a set of sample (sigma) points to approximate the state distribution as a GRV. Sigma points are a minimal set of deterministically chosen weighted sample points. They give an adequate coverage of the input and output probability distribution, i.e. when propagated through the nonlinear system they capture

## Chapter 3. Attitude Determination

the posterior mean and covariance in an accurate way. The summary of the UKF equations and the attitude estimator implementation shown are based on those presented in [13, 32].

### 3.2.2 Unscented Kalman Filtering

Both system and measurement noise are assumed to be additive, i.e. zero-mean. The number of sigma points required is  $2L + 1$ , where  $L$  is the number of states in the filter. The sigma point approach can be summarized as follows

1. A set of sigma points are calculated using the mean and square-root decomposition of the covariance matrix of the state variable
2. Sigma points are propagated through the nonlinear model (predict step)
3. The a posteriori statistics are calculated using functions of the propagated sigma points and weights (update step).

The filter is initialized with the predicted mean and covariance of the state.

$$\begin{aligned}\hat{\mathbf{x}}(t_0) &= E\{\hat{\mathbf{x}}_0\} \\ \mathbf{P}_{\mathbf{x}_0} &= E\{(\mathbf{x}(t_0) - \hat{\mathbf{x}}_0)(\mathbf{x}(t_0) - \hat{\mathbf{x}}_0)^T\}\end{aligned}\quad (3.17)$$

Then, the sigma point matrix  $\boldsymbol{\chi}_{k-1}$  is calculated

$$\begin{aligned}(\boldsymbol{\chi}_{k-1})_0 &= \hat{\mathbf{x}}_{k-1} \\ (\boldsymbol{\chi}_{k-1})_i &= \hat{\mathbf{x}}_{k-1} + (\sqrt{(L + \lambda)\mathbf{P}_{k-1}})_i, \quad i = 1 \dots L \\ (\boldsymbol{\chi}_{k-1})_i &= \hat{\mathbf{x}}_{k-1} + (\sqrt{(L + \lambda)\mathbf{P}_{k-1}})_i, \quad i = L + 1 \dots 2L\end{aligned}\quad (3.18)$$

where  $\lambda = \alpha^2(L + \kappa) - L$  is a scaling parameter. The constant  $\alpha$  determines the spread of the sigma points and  $\kappa$  is a secondary parameter which is usually set to  $\kappa = 3 - L$  [35].  $(\sqrt{(L + \lambda)\mathbf{P}_{k-1}})_i$  is the  $i$ th column of the matrix square root.

From this point, the prediction step is performed by propagating the sigma vectors through the nonlinear system model  $f$

$$(\boldsymbol{\chi}_k)_i = f((\boldsymbol{\chi}_{k-1})_i), \quad i = 1, \dots, 2L + 1 \quad (3.19)$$

The a priori state estimate is then computed

$$\hat{\mathbf{x}}_k^- = \sum_{i=0}^{2L} W_i^{(m)} (\boldsymbol{\chi}_k)_{i+1} \quad (3.20)$$

where

$$\begin{aligned}W_0^{(m)} &= \frac{\lambda}{L + \lambda} \\ W_i^{(m)} &= \frac{\lambda}{2(L + \lambda)}, \quad i = 1 \dots 2L\end{aligned}\quad (3.21)$$

### 3.2. Filtering Method

and the last part of the prediction step involves the calculation of the a priori error covariance

$$\mathbf{P}_k^- = \sum_{i=0}^{2L} W_i^{(c)} [(\boldsymbol{\chi}_k)_i - \hat{\mathbf{x}}_k^-][(\boldsymbol{\chi}_k)_i - \hat{\mathbf{x}}_k^-]^T + \mathbf{Q}_k \quad (3.22)$$

The matrix  $\mathbf{Q}_k$  is the process noise covariance matrix. The weights  $W_i^{(c)}$  are defined as

$$\begin{aligned} W_0^{(c)} &= \frac{\lambda}{L + \lambda} + (1 - \alpha^2 + \beta) \\ W_i^{(c)} &= \frac{\lambda}{2(L + \lambda)}, \quad i = 1 \dots 2L \end{aligned} \quad (3.23)$$

The scaling parameter  $\beta$  is used to incorporate prior knowledge of the distribution of the state vector and its optimal value for Gaussian distributions is  $\beta = 2$  [35].

The update step is then started by transforming the columns of  $(\boldsymbol{\chi}_k)_k$  through the sensor model  $h$ . Let  $(\mathbf{Z}_k)_i$  and  $\hat{\mathbf{z}}_k^-$  be the transformed sigma points and the transformed measurement vector, respectively. Then

$$\begin{aligned} (\mathbf{Z}_k)_i &= h((\boldsymbol{\chi}_k)_i), \quad i = 1, \dots, 2L + 1 \\ \hat{\mathbf{z}}_k^- &= \sum_{i=0}^{2L} W_i^{(m)} (\mathbf{Z}_k)_{i+1} \end{aligned} \quad (3.24)$$

The a posteriori state estimate can be computed using the measurement vector  $\mathbf{z}_k$

$$\hat{\mathbf{x}}_k = \hat{\mathbf{x}}_k^- + \mathbf{K}_k (\mathbf{z}_k - \hat{\mathbf{z}}_k^-) \quad (3.25)$$

The Kalman gain is calculated as

$$\mathbf{K}_k = \mathbf{P}_{\hat{x}_k \hat{z}_k} \mathbf{P}_{\hat{z}_k \hat{z}_k}^{-1} \quad (3.26)$$

where the measurement covariance matrix  $\mathbf{P}_{\hat{z}_k \hat{z}_k}$  and the state-measurement cross-covariance  $\mathbf{P}_{\hat{x}_k \hat{z}_k}$  are defined as

$$\begin{aligned} \mathbf{P}_{\hat{z}_k \hat{z}_k} &= \sum_{i=0}^{2L} W_i^{(c)} [(\mathbf{Z}_k)_i - \hat{\mathbf{z}}_k^-][(\mathbf{Z}_k)_i - \hat{\mathbf{z}}_k^-]^T + \mathbf{R} \\ \mathbf{P}_{\hat{x}_k \hat{z}_k} &= \sum_{i=0}^{2L} W_i^{(c)} [(\boldsymbol{\chi}_k)_i - \hat{\mathbf{x}}_k^-][(\mathbf{Z}_k)_i - \hat{\mathbf{z}}_k^-]^T \end{aligned} \quad (3.27)$$

The matrix  $\mathbf{R}$  is the measurement noise covariance matrix.

Finally, the last section of the update step requires the computation of the a posteriori error covariance

$$\mathbf{P}_k = \mathbf{P}_k^- - \mathbf{K}_k \mathbf{P}_{\hat{z}_k \hat{z}_k} \mathbf{K}_k^T \quad (3.28)$$

The resultant a posteriori error covariance matrix must be saved to be used in the following iteration of the filter.

## Chapter 3. Attitude Determination

### 3.2.3 UKF implementation for AntelSat

The state vector used by the UKF based estimator for the AntelSat is

$$\mathbf{x} = [ \mathbf{q}^T \ \boldsymbol{\omega}^T \ \mathbf{T}_{dist}^T ]^T = [ \mathbf{q}_{ci}^T \ c\boldsymbol{\omega}_{ci}^T \ c\mathbf{T}_{dist}^T ]^T \quad (3.29)$$

The quaternion and rate vector are needed for attitude control. Considering slowly varying disturbance torques, an estimate of the disturbance torque vector  $\mathbf{T}_{dist}$  is included in the state estimate to provide added robustness and accuracy [36,37].

The use of quaternions as a part of the state variable presents certain obstacles. This is due to the fact that unit quaternions are not closed for addition and scalar multiplication and the UKF determines the time update through a weighted average. This implies that the use of full four-element quaternions in the update step of the UKF would not always produce a unit quaternion. Thus, a three-element error quaternion  $\delta\hat{\mathbf{q}}_k$  is defined in Eq. (3.30), as in e.g. [13,21,32]. The error quaternion does not have this constraint [33].

$$\begin{aligned} \delta\hat{\mathbf{q}}_k &= \hat{\mathbf{q}}_k \otimes (\hat{\mathbf{q}}_k^-)^{-1} \\ \delta\hat{\mathbf{q}}_k &= [ \delta\hat{\mathbf{q}}_{v,k}^T \ \delta\hat{q}_4 ]^T = [ \delta\hat{q}_1 \ \delta\hat{q}_2 \ \delta\hat{q}_3 \ \delta\hat{q}_4 ]^T \end{aligned} \quad (3.30)$$

Given the estimated quaternion  $\hat{\mathbf{q}}_k$ , the vector part of the error quaternion  $\delta\hat{\mathbf{q}}_k$  is the update to the predicted quaternion  $\hat{\mathbf{q}}_k^-$ . The three-element error quaternion is expanded to a four-element quaternion and the aforementioned unity constraint is preserved with the use of a multiplicative update step, as in Eq. (3.31)

$$\begin{aligned} \delta\hat{\mathbf{x}}_k &= \mathbf{K}_k(\mathbf{z}_k - \hat{\mathbf{z}}_k^-) \\ \hat{\mathbf{q}}_k &= [ (\delta\hat{\mathbf{q}}_{v,k})^T \ \sqrt{1 - (\delta\hat{\mathbf{q}}_{v,k})^T \cdot (\delta\hat{\mathbf{q}}_{v,k})} ]^T \otimes \hat{\mathbf{q}}_k^- \\ \hat{\mathbf{x}}_k &= [ \hat{\mathbf{q}}_k^T \ (\hat{\boldsymbol{\omega}}_k^- + \delta\hat{\boldsymbol{\omega}}_k)^T \ (\hat{\mathbf{T}}_{dist,k}^- + \delta\hat{\mathbf{T}}_{dist,k})^T ]^T \end{aligned} \quad (3.31)$$

Full and error sigma points,  $\boldsymbol{\chi}$  and  $\delta\boldsymbol{\chi}$  respectively, are then determined by

$$\begin{aligned} (\boldsymbol{\chi})_i &= [ (\mathbf{q}^\sigma)_i^T \ (\boldsymbol{\omega}^\sigma)_i^T \ (\mathbf{T}_{dist}^\sigma)_i^T ]^T \\ (\delta\boldsymbol{\chi})_i &= [ (\delta\mathbf{q}_v^\sigma)_i^T \ (\delta\boldsymbol{\omega}^\sigma)_i^T \ (\delta\mathbf{T}_{dist}^\sigma)_i^T ]^T \end{aligned} \quad (3.32)$$

In order to calculate the sigma points a matrix square root must be computed. This can be efficiently carried out by using a Cholesky decomposition (see [38]). In this thesis, the lower-triangular Cholesky factorization is used. Since the number of error states used for the UKF filter is  $L = 9$ , the amount of sigma point vectors involved is  $2L + 1 = 19$ .

Inputs needed by the estimator include observations of sun, magnetic field and angular rate vectors,  ${}^b\mathbf{s}$ ,  ${}^b\mathbf{b}$  and  ${}^b\boldsymbol{\omega}$  respectively, and predicted measurements in the ECI,  ${}^i\mathbf{s}$ ,  ${}^i\mathbf{b}$  respectively.

The state needs to be propagated though the nonlinear equations defined for the system. These equations consist of the satellite equations of motion Eqs. (2.23) and (2.34) with the addition of the disturbance torque equation

$$\begin{aligned}
\dot{\boldsymbol{\omega}} &= \mathbf{I}^{-1}(\mathbf{T}_{ctrl} + \mathbf{T}_{dist} - \boldsymbol{\omega} \times \mathbf{I}\boldsymbol{\omega}) \\
\dot{\mathbf{q}} &= \frac{1}{2}\mathbf{W}(\boldsymbol{\omega}) \cdot \mathbf{q} \\
\dot{\mathbf{T}}_{dist} &= \mathbf{0}
\end{aligned} \tag{3.33}$$

The control torque  $\mathbf{T}_{ctrl}$  is computed in accordance with Eqs. (2.24) and (2.26) using the controller output of the previous step for the magnetorquer current vector  $\mathbf{i}_{coil,k-1}$ . The state propagation is carried out by numerically integrating the continuous time functions in Eq. (3.33) over a sampling time  $T_s$  with a fourth-order Runge Kutta method (denoted as *RK4*, see [39]). The state propagations has to be done for every sigma point. Finally, the a priori state estimate is found by a weighted sum of all the propagated sigma points, as in Eq. (3.20). If the sampling time  $T_s$  is relatively large compared to the angular velocity of the satellite, it might be necessary to use several sub-steps in the Runge Kutta method. However, as the multiple simulations performed have shown, a single sub-step suffices even for the worst case of magnitude of angular velocity considered—this fact is also noted in [13]. On top of that, the addition of extra sub-steps would sensibly increment calculation times involved, since state propagation is the most computationally costly part of the algorithm and it has to be carried out for every sigma point. Altogether, a single sub-step for the Runge Kutta method is used in this implementation.

For calculating the expected measurement, the attitude state information included in every sigma points is used. Reference vectors for the Sun and geomagnetic field vectors given in the inertial coordinate system,  ${}^i\mathbf{s}$  and  ${}^i\mathbf{b}$ , are rotated to the spacecraft body coordinate system according to the corresponding attitude quaternion  $\mathbf{q}^\sigma$ . For the angular rate expected measurement,  $\boldsymbol{\omega}^\sigma$  is used

$$h((\boldsymbol{\chi}_k)) = \begin{bmatrix} \mathbf{R}(\mathbf{q}^\sigma) {}^i\mathbf{s} \\ \mathbf{R}(\mathbf{q}^\sigma) {}^i\mathbf{b} \\ \boldsymbol{\omega}^\sigma \end{bmatrix} \tag{3.34}$$

The direction cosine matrix  $\mathbf{R}$  represents the same rotation as  $\mathbf{q}^\sigma$ , as defined in Eq. (2.11). Sun and geomagnetic field measurements are normalized beforehand to avoid numerical complications when handling matrix computations. Sun measurements are not taken into account when the spacecraft is in eclipse.

Contrary to the deterministic method presented in Section 3.1.3, the UKF-based estimator yields attitude information with respect to the inertial reference system, i.e.  $\mathbf{q}_{ci}$  and  ${}^c\boldsymbol{\omega}_{ci}$ , and not w.r.t. the ORF, i.e.  $\mathbf{q}_{co}$  and  ${}^c\boldsymbol{\omega}_{co}$ . Translation from  $\mathbf{q}_{ci}$  and  ${}^c\boldsymbol{\omega}_{ci}$  to  $\mathbf{q}_{co}$  and  ${}^c\boldsymbol{\omega}_{co}$  can be accomplished by applying Eqs. (2.15) and (2.33), respectively.

As mentioned earlier in the thesis, for simplicity's sake it is assumed that the body and control coordinate systems coincide. If this assumption was not considered, and since Eq. (3.33) is expressed in the CRF, both the control torque and angular rate vectors would have had to be rotated from the BRF to the CRF. The

## Chapter 3. Attitude Determination

same holds for the Sun and magnetic field measurement vectors since the coordinate system they are expressed in and the coordinate system for reference vectors in Eq. (3.34) have to be the same.

A summary of the involved steps in the attitude estimator is presented below.

### 1. Initialization

- (a) The state is initialized with

$$\hat{\mathbf{x}}_0 = [ \hat{\mathbf{q}}_0^T \ \boldsymbol{\omega}_0^T \ \hat{\mathbf{T}}_{dist,0}^T ]^T = [ 0 \ 0 \ 0 \ 1 \ \boldsymbol{\omega}_{k-1}^T \ 0 \ 0 \ 0 ]^T \quad (3.35)$$

- (b) Calculate weights

$$\begin{aligned} W_0^{(c)} &= \frac{\lambda}{L + \lambda} + (1 - \alpha^2 + \beta), \quad W_i^{(c)} = \frac{\lambda}{2(L + \lambda)}, \\ W_0^{(m)} &= \frac{\lambda}{L + \lambda}, \quad W_i^{(m)} = \frac{\lambda}{2(L + \lambda)}, \quad i = 1 \dots 2L \end{aligned} \quad (3.36)$$

### 2. Predict

- (a) Calculate error sigma points

$$\delta \boldsymbol{\chi}_{k-1} = [ \mathbf{0}_{9 \times 1} \ - (\sqrt{(L + \lambda) \mathbf{P}_{k-1}})^T \ (\sqrt{(L + \lambda) \mathbf{P}_{k-1}})^T ]^T \quad (3.37)$$

- (b) Full sigma points

$$\begin{aligned} (\mathbf{q}_{k-1}^\sigma)_i &= [ (\delta \mathbf{q}_{v,k-1}^\sigma)^T \sqrt{1 - (\delta \mathbf{q}_{v,k-1}^\sigma)^T \cdot (\delta \mathbf{q}_{v,k-1}^\sigma)} ]^T \otimes \hat{\mathbf{q}}_{k-1} \\ (\boldsymbol{\chi}_{k-1})_i &= [ (\mathbf{q}_{k-1}^\sigma)_i^T \ (\hat{\boldsymbol{\omega}}_{k-1} + (\delta \boldsymbol{\omega}_{k-1}^\sigma)_i)^T \\ &\quad (\hat{\mathbf{T}}_{dist,k-1} + (\delta \mathbf{T}_{dist,k-1}^\sigma)_i)^T ]^T, \quad \text{for } i = 1, \dots, 2L + 1 \end{aligned} \quad (3.38)$$

- (c) Numerical propagation

$$(\boldsymbol{\chi}_k)_i = RK4((\boldsymbol{\chi}_{k-1})_i, T_{ctrl,k-1}, T_s), \quad \text{for } i = 1, \dots, 2L + 1 \quad (3.39)$$

- (d) Compute a priori state estimate and normalize quaternion

$$\begin{aligned} \hat{\mathbf{x}}_k^- &= \sum_{i=0}^{2L} W_i^{(m)} (\boldsymbol{\chi}_k)_{i+1} \\ \hat{\mathbf{q}}_k^- &= \hat{\mathbf{q}}_k^- / \|\hat{\mathbf{q}}_k^-\| \end{aligned} \quad (3.40)$$

- (e) Full state to error state

$$\begin{aligned} (\delta \boldsymbol{\chi}_{k-1})_i &= [ ((\mathbf{q}_k^\sigma)_i \otimes (\hat{\mathbf{q}}_k^-)^{-1})_{v,i}^T \ ((\boldsymbol{\omega}_k^\sigma)_i - \hat{\boldsymbol{\omega}}_k^-)^T \\ &\quad ((\mathbf{T}_{dist,k}^\sigma)_i - \hat{\mathbf{T}}_{dist,k}^-)^T ]^T, \quad \text{for } i = 1, \dots, 2L + 1 \end{aligned} \quad (3.41)$$

(f) Calculate a priori covariance

$$\mathbf{P}_k^- = \sum_{i=0}^{2L} W_i^{(c)} [(\delta\boldsymbol{\chi}_k)_i - \delta\hat{\mathbf{x}}_k^-][(\delta\boldsymbol{\chi}_k)_i - \delta\hat{\mathbf{x}}_k^-]^T + \mathbf{Q} \quad (3.42)$$

### 3. Update

(a) Normalize Sun and magnetic field measurement vectors

$$\begin{aligned} {}^b\mathbf{s}_k &= {}^b\mathbf{s}_k / \left\| {}^b\mathbf{s}_k \right\|, \quad {}^b\mathbf{b}_k = {}^b\mathbf{b}_k / \left\| {}^b\mathbf{b}_k \right\| \\ \mathbf{z}_k &= [ ({}^b\mathbf{s}_k)^T \quad ({}^b\mathbf{b}_k)^T \quad ({}^b\boldsymbol{\omega}_k)^T ]^T \end{aligned} \quad (3.43)$$

(b) Calculate transformed measurement of each sigma point

$$(\mathbf{Z}_k)_i = \begin{bmatrix} \mathbf{R}(\mathbf{q}_k^\sigma)^i \mathbf{s} \\ \mathbf{R}(\mathbf{q}_k^\sigma)^i \mathbf{b} \\ \boldsymbol{\omega}_k^\sigma \end{bmatrix}, \text{ for } i = 1, \dots, 2L + 1 \quad (3.44)$$

(c) Expected measurement vector

$$\hat{\mathbf{z}}_k^- = \sum_{i=0}^{2L} W_i^{(m)} (\mathbf{Z}_k)_{i+1} \quad (3.45)$$

(d) Compute covariance matrices

$$\begin{aligned} \mathbf{P}_{\hat{\mathbf{z}}_k \hat{\mathbf{z}}_k} &= \sum_{i=0}^{2L} W_i^{(c)} [(\mathbf{Z}_k)_i - \hat{\mathbf{z}}_k^-][(\mathbf{Z}_k)_i - \hat{\mathbf{z}}_k^-]^T + \mathbf{R} \\ \mathbf{P}_{\hat{\mathbf{x}}_k \hat{\mathbf{z}}_k} &= \sum_{i=0}^{2L} W_i^{(c)} [(\boldsymbol{\chi}_k)_i - \hat{\mathbf{x}}_k^-][(\mathbf{Z}_k)_i - \hat{\mathbf{z}}_k^-]^T \end{aligned} \quad (3.46)$$

(e) Kalman gain

$$\mathbf{K}_k = \mathbf{P}_{\hat{\mathbf{x}}_k \hat{\mathbf{z}}_k} \mathbf{P}_{\hat{\mathbf{z}}_k \hat{\mathbf{z}}_k}^{-1} \quad (3.47)$$

(f) Error state

$$\delta\hat{\mathbf{x}}_k = \mathbf{K}_k (\mathbf{z}_k - \hat{\mathbf{z}}_k^-) \quad (3.48)$$

(g) Expand error quaternion and calculate full state

$$\hat{\mathbf{x}}_k = [ \hat{\mathbf{q}}_k^T \quad (\hat{\boldsymbol{\omega}}_k^- + \delta\hat{\boldsymbol{\omega}}_k)^T \quad (\hat{\mathbf{T}}_{dist,k}^- + \delta\hat{\mathbf{T}}_{dist,k})^T ]^T \quad (3.49)$$

(h) Compute a posteriori covariance

$$\mathbf{P}_k = \mathbf{P}_k^- - \mathbf{K}_k \mathbf{P}_{\hat{\mathbf{z}}_k \hat{\mathbf{z}}_k} \mathbf{K}_k^T \quad (3.50)$$

### 3.3 Simulations

A vast number of simulations were carried out to verify the performance of the attitude determination methods and to compare its results. A representative simulation run is presented in this section.

The orbit parameters used for these simulations are those of a polar orbit with an inclination of nearly  $99^\circ$  and an orbit height of close to 650 km. These parameters imply an orbital period of 98 min. This kind of orbit is typical for CubeSats.

Initial roll, pitch, yaw and angular rates were set to  $RPY = [120 \ -32 \ 88]^\circ$  and  ${}^b\boldsymbol{\omega}_{bi} = [0.05 \ 1 \ 2]^\circ/\text{s}$ , respectively, with initial condition attitude estimates set to zero. Because of the initial conditions used, the satellite starts in a detumbling state and thus, the B-dot control law is used at the beginning. Once the angular rate underpasses the nominal threshold value, the LQR controller takes over.

Expected noise for the sensors has been set in the following manner. Noise in the magnetic field measurements (magnetometer) has a variance of  $\sigma_{mm}^2 = 2e^{-12}$ . For the Sun sensors, a standard deviation of  $\sigma_{ss}^2 = 0.05$  for normalized measurements was considered. The gyroscope is expected to add a noise with a variance of  $\sigma_{gy}^2 = 10e^{-6}$ .

For the UKF, the measurement noise covariance matrix  $\mathbf{R}$ , the model noise covariance  $\mathbf{Q}$  and the initial error covariance matrix  $\mathbf{P}_0$  were tuned to the following values, based on the noise in the sensors and multiple simulation runs:

$$\begin{aligned} \mathbf{Q} &= \text{diag}([10 \ 10 \ 10 \ 1 \ 1 \ 1 \ 1 \ 0.01 \ 0.01 \ 0.01] * 10^{-6}) \\ \mathbf{R} &= \text{diag}([0.48 \ 0.48 \ 0.48 \ 50 \ 50 \ 50 \ 0.01 \ 0.01 \ 0.01] * 10^{-3}) \\ \mathbf{P}_0 &= \text{diag}([10^{-3} \ 10^{-3} \ 10^{-3} \ 10^{-3} \ 10^{-3} \ 10^{-3} \ 10^{-9} \ 10^{-9} \ 10^{-9}]) \end{aligned} \quad (3.51)$$

The elements of the process noise covariance matrix should be increased to add robustness to the filter, and they should be decreased to improve accuracy. Reducing the values corresponds to “trust” more in the model. The first three diagonal elements in  $\mathbf{Q}$  are related to the expected noise in the quaternion part of the state vector, the next three correspond to the noise in the angular rate part of the state vector and the last three reflect the noise of the disturbance torque vector. For the  $\mathbf{R}$ , its diagonal elements reflect the expected noise in the magnetic field vector measurements, Sun vector measurements and angular rate measurements, respectively. The elements of the initial error covariance matrix  $\mathbf{P}_0$  are related to how good a guess the initial state is. All off-diagonal elements are set to zero.

UKF tuning values  $\alpha$ ,  $\beta$  and  $\gamma$  were set to  $\sqrt{3}$ , 2 and 0, respectively.

Figures 3.2 to 3.4 show the results of the simulation run for the QuEst algorithm for close to 1.5 orbits. The shaded areas represent the times in which the satellite was in eclipse. The values in these areas are not valid since there are no Sun vector measurements available, making the attitude unobservable. The default output for the algorithm under this circumstance is roll, pitch, yaw equal to  $(0, 0, 0)^\circ$ . In Fig. 3.2, the difference between the angles for the real attitude and for the algorithm output is presented. The results are displayed for each axis separately. Figure 3.3 presents the euclidean norm of the mentioned difference and Fig. 3.4

### 3.3. Simulations

shows a logarithm of this norm. The real attitude considered in this case is the rotation of the BRF w.r.t. ORF, that is, the rotation described by  $\mathbf{q}_{bo}$ .

Figures 3.5 and 3.6 show the results of the same simulation run, but this time for the UKF-based estimator. Again, the shaded areas represent the times in which the satellite was in eclipse, although values in these areas are valid in this case since the UKF is able to determine the attitude even when the spacecraft is in eclipse. The real attitude considered in this case is the rotation of the BRF w.r.t. ECI, that is, the rotation described by  $\mathbf{q}_{bi}$ . The difference between the angles for the real attitude and for the algorithm output is considered. Figure 3.5 presents the euclidean norm of the mentioned difference and Fig. 3.6 shows a logarithm of this norm.

As can be seen in the mentioned figures, the UKF estimator outperforms the QuEst algorithm. The main reason for this is that the former provides an attitude estimate even when the spacecraft is in eclipse, while the latter does not. On top of that, average error values are smaller for the UKF. QuEst presents a mean error outside the eclipse of  $4.5^\circ$  with occasional bursts of up to  $30^\circ$ , while UKF gets to a steady-state mean error of  $1.75^\circ$  after the first orbit. After the initial convergence phase, that is before 0.2 orbits, UKF never exceeds  $10^\circ$  in error, even in the second eclipse stage.

The representative simulation run presented starts with the satellite in eclipse and with an initial attitude condition far off the default initial condition considered for the UKF (roll, pitch, yaw equals to  $(0, 0, 0)$ ), which poses a disadvantageous situation for attitude estimation. However, as can be seen in Fig. 3.5, convergence is pretty fast since an error of under  $10^\circ$  is achieved in less than 20 minutes, 10 minutes after leaving the eclipse stage. Faster convergence times for the UKF could be achieved by using a more accurate initial condition, say, by taking the output of the QuEst. Nevertheless, this could not be possible if the satellite were in eclipse at the beginning of the attitude determination.

One of the major drawbacks of the UKF are computation times. As mentioned earlier, this is mainly due to the fact that state propagation has to be run for all sigma vectors. Clearly, adding more elements to the state vector—e.g. in order to add more robustness to the filter or to estimate some relevant parameters—sensibly adds to the calculation burden. As has been mentioned earlier, an effective method to reduce these times is to remove sub-steps in the Runge Kutta implementation. Various simulations have shown that runs using ten, four and one Runge Kutta sub-steps produced no significant difference while computation times significantly reduced as the amount of sub-steps diminished.

### Chapter 3. Attitude Determination

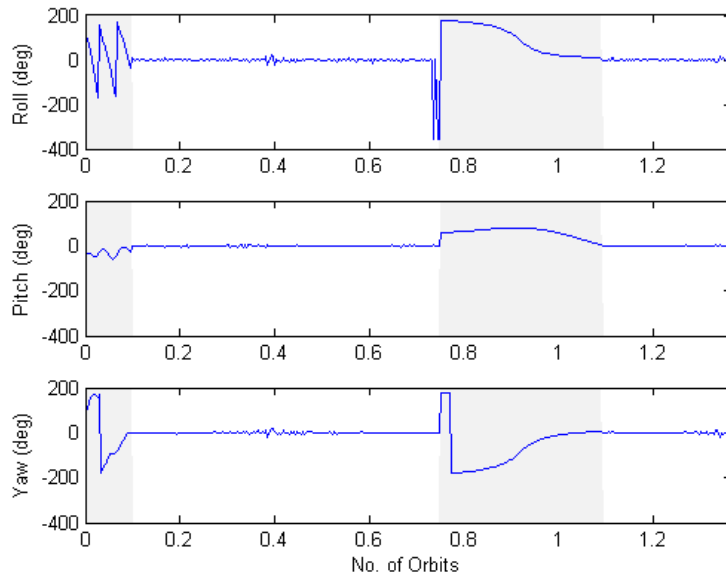


Figure 3.2: Attitude error in degrees of QuEst with respect to  $\mathbf{q}_{bo}$ .

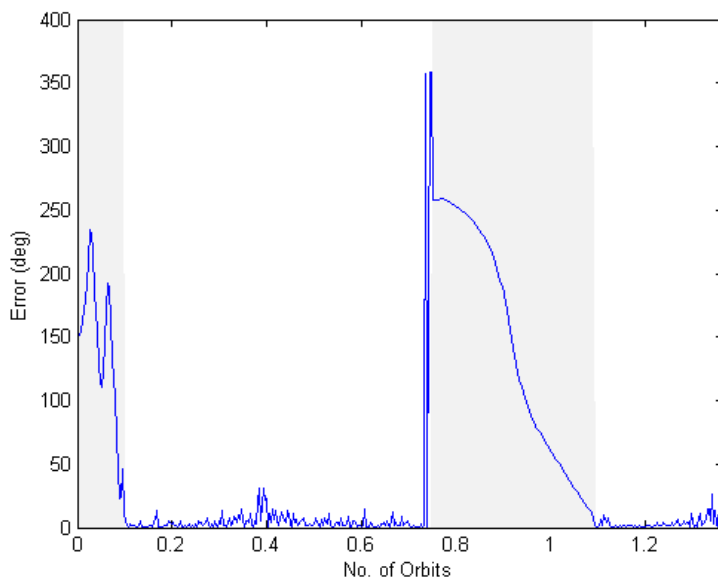


Figure 3.3: Absolute attitude error in degrees of QuEst with respect to  $\mathbf{q}_{bo}$ .

### 3.3. Simulations

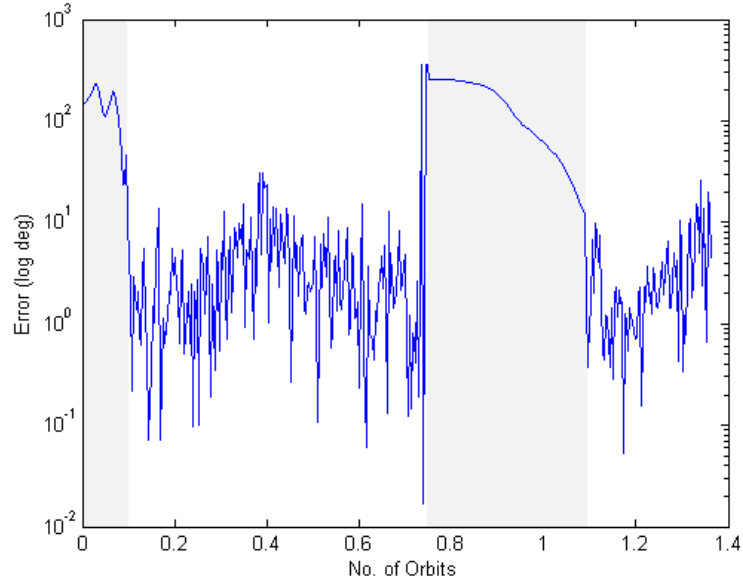


Figure 3.4: Absolute attitude error of QuEst with respect to  $\mathbf{q}_{bo}$ , in logarithmic scale.

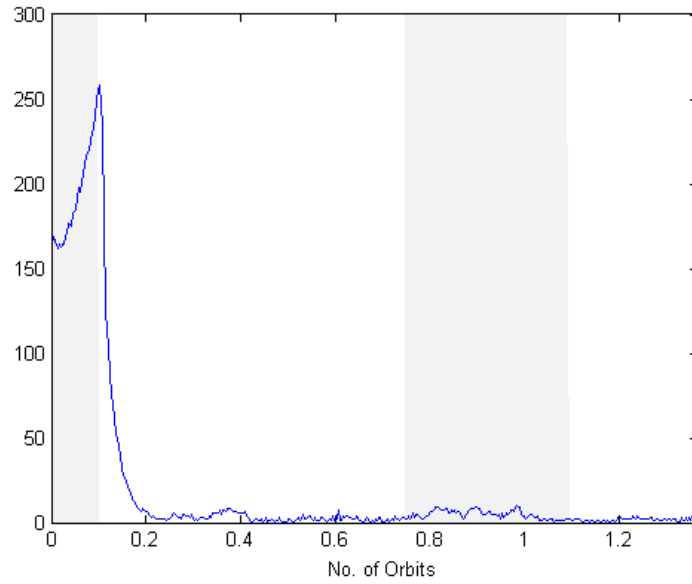


Figure 3.5: Absolute attitude error in degrees of UKF with respect to  $\mathbf{q}_{bi}$ .

### Chapter 3. Attitude Determination

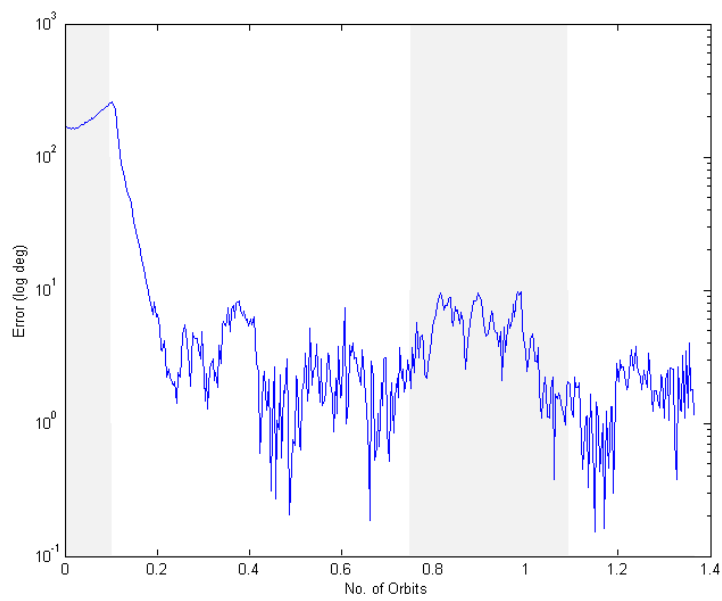


Figure 3.6: Absolute attitude error of UKF with respect to  $\mathbf{q}_{bi}$ , in logarithmic scale.

## 3.4 Summary

In this chapter, a description of the different attitude determination methods was presented with, on one hand, the optimal quaternion estimator, a deterministic method, and on the other hand, an attitude estimator based on an unscented Kalman filter. A theory background has also been introduced. Finally, the chapter closes with simulations that demonstrate the performance of the different methods.

This page has been intentionally left blank.

# Chapter 4

## Attitude Control

In classical literature, magnetic attitude control schemes for satellite were used in combination with other active or passive stabilization techniques, not particularly as the main attitude control method. Uses of magnetic actuators in attitude control include momentum management of wheel-based systems [40], spin-stabilized systems [41,42] and gravity-gradient based systems [43]. On the other hand, there have been a growing number of studies that consider active 3-axis magnetic attitude stabilization for nadir-pointing spacecraft [3,4,6,44]. In [45], the earliest such study, a 3-axis proportional-derivative control law was presented. [46] first attempted to use a fully magnetic control scheme using a linear quadratic regulator (LQR). In [28] the idea was developed further using a combination of both linear and nonlinear control theory. In particular, a LQR constant gain controller based on the application of control theory for linear time-invariant periodic systems was developed.

Magnetic actuators possess several advantages over other similar options: a magnetorquer-based system will weigh less than either a wheel-based system or a gravity-gradient system, and it will consume less power than a wheel-based system. Thus, they are ideal for small satellite applications where power and weight budgets are tightly constrained. However, attitude control by means of magnetic actuation pose a significant challenge: the system is under-actuated. As can be seen in Eq. (2.26), the resultant control torque is perpendicular to the local geomagnetic field, hence, the system is controllable at any given instant in the orbit only in the two axes that are perpendicular to Earth's magnetic field. Notwithstanding, the system is controllable if the orbit is inclined because the geomagnetic field vector rotates in space as the satellite travels around its orbit [29]. It is a time-varying system that can be approximated as periodic.

The attitude control strategy for the AntelSat is as follows. Two different control phases are defined: detumbling and nadir pointing. Each of these phases possess its own controller. Detumbling occurs when the spacecraft rotational velocity presents significant values-i.e. when the satellite is deployed from the rocket. Under these circumstances, the system presents considerable nonlinear behaviour thus, a nonlinear controller is applied-the B-bot controller. For the nadir stabilization phase, a full state feedback LQR controller is employed. In this situation,

## Chapter 4. Attitude Control

the satellite trajectory must remain in a window of 10 degrees for pitch, roll and yaw, and its angular rate must remain quite small. Consequently, it is reasonable to adopt a linear approach for this mode.

In this chapter, control laws for the aforementioned control phases are presented, along with relevant theoretical background. Computer simulations to show the feasibility of each controller are also presented. Section 4.1 introduces the detumbling controller, whereas Section 4.1.4 includes simulations related to this controller. On the other hand, Section 4.2 presents the nominal controller, whereas the respective simulations are included in Section 4.2.2.

### 4.1 Detumbling Controller

One of the very first tasks that the attitude control system of the nanosatellite is to carry out after the deployment of the spacecraft from the carrier rocket is the stabilization of its angular rate.

This damping of the rotational kinetic energy, is often referred to as detumbling and is of central importance for a correct development of the mission. This procedure should be done correctly by a robust and simple system. Hence, a  $\dot{\mathbf{B}}$  (B-dot) controller was selected for the detumbling of the AntelSat. This kind of controller has long been used effectively in various projects [3, 4, 47, 48].

The aim of the controller is to reduce the kinetic energy of the satellite to a level where a more accurate controller can take over. It only requires the measurements from the onboard magnetometer.

#### 4.1.1 B-dot proportional control law

The simplicity of the control law can be observed in the following equation.

$${}^b\mathbf{m} = -C_D {}^b\dot{\mathbf{B}}_E \quad (4.1)$$

where  $C_D$  is a positive scalar gain. On a per-axis basis, the B-dot control laws command a magnetic moment whose sign is opposite to that of the rate of change of the magnetic field along that axis. Since  ${}^b\dot{\mathbf{B}}_E$  is perpendicular to  ${}^b\mathbf{B}_E$ , this control law gives an output to the actuators which is a dipole moment perpendicular to  ${}^b\mathbf{B}_E$ .

It is based on the assumption that, for high angular rates, the rate of change of the B-field in the body reference frame is mainly due to the rotation of the spacecraft. This point can be expressed as:

$${}^b\dot{\mathbf{B}}_E \approx {}^b\boldsymbol{\omega}_{bi} \times {}^b\mathbf{B}_E \quad (4.2)$$

In reality, the geomagnetic time derivative  ${}^b\dot{\mathbf{B}}_E$  is difficult to measure and an estimate  $\hat{{}^b\dot{\mathbf{B}}_E}$  will be used instead for the implementation of the controller.

### 4.1.2 Lyapunov Stability

The stability using the control law in Eq. (4.1) can be proved using the Lyapunov stability criterion for the zero angular rate  ${}^b\boldsymbol{\omega}_{bo}$ . The Lyapunov candidate function and its derivative is

$$V = \frac{1}{2} {}^b\boldsymbol{\omega}_{bi}^T \cdot \mathbf{I} {}^b\boldsymbol{\omega}_{bi} \quad (4.3)$$

$$\dot{V} = {}^b\boldsymbol{\omega}_{bi}^T \cdot \mathbf{I} \dot{{}^b\boldsymbol{\omega}_{bi}} \quad (4.4)$$

Neglecting external disturbances, the change of kinetic energy during the detumbling phase is due to the torque applied by the magnetorquers, that is, the kinetic energy decreases if the dot product of the angular velocity and the torque is negative

$${}^b\boldsymbol{\omega}_{bi}^T \cdot {}^b\mathbf{T}_{ctrl} < 0 \quad (4.5)$$

The control torque is

$${}^b\mathbf{T}_{ctrl} = {}^b\mathbf{m} \times {}^b\mathbf{B}_E \quad (4.6)$$

Substituting this into Eq. (4.5) and using that  $\mathbf{a}^T(\mathbf{b} \times \mathbf{c}) = \mathbf{c}^T(\mathbf{a} \times \mathbf{b})$  gives

$$\begin{aligned} {}^b\boldsymbol{\omega}_{bi}^T \cdot ({}^b\mathbf{m} \times {}^b\mathbf{B}_E) < 0 &\Leftrightarrow -{}^b\boldsymbol{\omega}_{bi}^T \cdot ({}^b\mathbf{B}_E \times {}^b\mathbf{m}) < 0 \\ &\Leftrightarrow -{}^b\mathbf{m}^T \cdot ({}^b\boldsymbol{\omega}_{bi} \times {}^b\mathbf{B}_E) < 0 \end{aligned} \quad (4.7)$$

The above inequality can be solved by

$${}^b\mathbf{m} = C_D \cdot ({}^b\boldsymbol{\omega}_{bi} \times {}^b\mathbf{B}_E) \quad (4.8)$$

since  $C_D$  is a positive. Using the main assumption for the detumbling phase in Eq. (4.2) (basically,  ${}^b\boldsymbol{\omega}_{bi} \approx {}^b\boldsymbol{\omega}_{bo}$ ), the B-dot control law becomes as stated in Eq. (4.1).

### 4.1.3 State variable filter

The B-dot algorithm takes B-field vector measurements from the magnetometer as inputs to compute its outputs. Since any real sensor adds noise to the measurement process, the signals have to be filtered before computing their derivative. In order to achieve this, a design as shown in Fig. 4.1 is proposed.

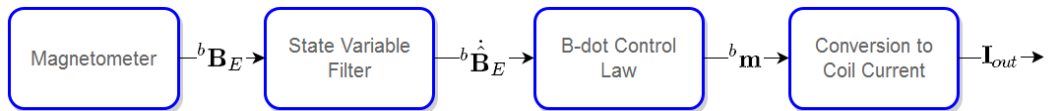


Figure 4.1: Block diagram of the B-dot controller

A state variable filter will be used to estimate the derivative of the Earth's magnetic field. A block diagram of the filter is shown in Fig. 4.2, where  $\omega_c$  is the cut-off frequency for the filter and  $s$  is the Laplace transform variable.

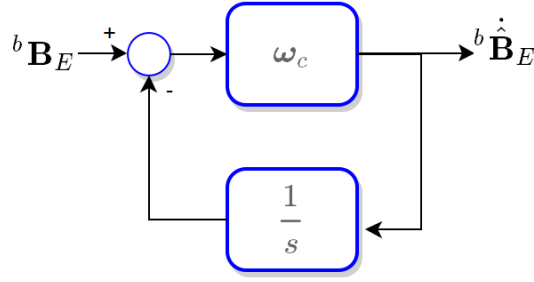


Figure 4.2: Block diagram of the state variable filter

Here, the Laplace transform for the transfer function is

$$\frac{b\dot{\mathbf{B}}_E}{b\mathbf{B}_E}(s) = \frac{s\omega_c}{s + \omega_c} \quad (4.9)$$

For low frequencies ( $s \ll \omega_c$ ) the transfer function approximates to  $s$ , which corresponds to pure differentiation. For large frequencies ( $s \gg \omega_c$ ) the transfer function approximates to  $\omega_c$ , which is just a gain. The cut-off frequency  $\omega_c$  should be chosen around 5 to 10 times as high as the fastest expected change of  $b\mathbf{B}_E$ . As mentioned before, it is assumed in the detumbling stage that the change in the Earth's magnetic field is due to the rotation of the satellite, thus the maximum change is determined by the maximum spin rate of the satellite multiplied by the maximum magnitude of the magnetic field.

In practice, the integration appearing in Fig. 4.2 will be performed numerically. The bilinear transform method was used in the filter design process. For this, the following substitution is performed in Eq. (4.9) (see e.g. [49]) and it gives:

$$\begin{aligned} s &\leftarrow \frac{2}{T} \frac{1 - z^{-1}}{1 + z^{-1}} \\ b\dot{\mathbf{B}}_{Ek} &= b(b\mathbf{B}_{Ek} - b\mathbf{B}_{Ek-1} - a b\dot{\mathbf{B}}_{Ek-1}) \\ a &= \frac{\omega_c - 2/T}{\omega_c + 2/T} \\ b &= \left(\frac{2\omega_c}{T}\right) \frac{1}{(2/T + \omega_c)} \end{aligned} \quad (4.10)$$

#### 4.1.4 Simulations

This section presents some representative simulations carried out to assert the performance of the detumbling controller.

The orbit parameters used for these simulations are those of a polar orbit with an inclination of nearly  $99^\circ$  and an orbit height of close to 650 km. These parameters imply an orbital period of 98 min and  $\omega_0 = 0.011$  rad/s. This kind of orbit is typical for CubeSats. Perturbation torques and realistic sensor and actuator models were included.

## 4.1. Detumbling Controller

The B-dot controller gain  $C_D$  is set to  $C_D = 20000$  based on iterative simulations. While this gain keeps the consumption low, it keeps the requirements for the controller.

Initial roll, pitch, yaw and angular rates were set to  $RPY = [ +20 \ -32 \ +88 ]^\circ$  and  ${}^b\omega_{bo} = [ +40 \ -30 \ -12 ]^\circ/\text{s}$ , respectively. The total simulation time is 2.5 orbits. Figures 4.3 to 4.6 present the results of running the detumbling controller in these highly nonlinear conditions. It is worth noting that average expected angular rates after deployment of the satellite from the P-POD are 2-8 times less than the ones used in this simulation.

Figure 4.3 displays the angular velocity of each axis expressed in rad/s, whereas Fig. 4.4 presents the absolute value of the angular velocity, also expressed in rad/s. Finally, Fig. 4.5 shows the control exerted by the magnetorquers, and Fig. 4.6 displays the disturbance torque applied on the satellite.

As can be seen in Fig. 4.4, the absolute value of the angular rate reaches the nominal controller threshold value ( $0.1^\circ/\text{s} = 0.017\text{rad/s}$ ) in 1.2 orbits. In other words, the controller is able to decrease the initial angular rate value in 500% in about 120 min.

Two other simulation runs are presented below to show the robustness of the control law. Initial roll, pitch, yaw and angular rates were set to the same values as the previous simulation run. The total simulation time is 2.5 orbits. Figs. 4.7 to 4.10 display the results of running the same controller for the same initial conditions, but with the Y-axis coil off, while Figs. 4.11 to 4.14 display the results of running the controller with only the Z-axis coil on. This situation could occur, i.e., in case of actuator malfunction. Figures 4.7 and 4.11 display the angular velocity of each axis expressed in rad/s for each case, respectively, whereas Figs. 4.8 and 4.12 present the absolute value of the angular velocity, also respectively and expressed in rad/s. Finally, Figs. 4.9 and 4.13 show control torque exerted by the magnetorquers, and Figs. 4.10 and 4.14 display the total disturbance torque applied on the satellite, respectively.

For the first case—Y-axis coil off—, it can be seen on Fig. 4.8 that the absolute value of the angular rate reaches the nominal controller threshold value as well, although in a longer period of time than the nominal case (1.6 orbits compared to 1.2).

For the remaining case—only Z-axis coil on—, simulations show that even with one coil working the detumbling controller is able to sensibly decrease the magnitude of the angular rate of the spacecraft, although in this case the final absolute value of the angular rate remains higher than the nominal controller threshold value. This implies that even though the B-dot control law consists of a truly trustworthy resource for attitude control, it possesses its limits. Nonetheless, despite the fact the final magnitude of the angular velocity for this case is not as low as it would be desired, the controller is able to reduce the initial value of the angular rate in a factor of 8, leaving the spacecraft in a reasonable situation.

## Chapter 4. Attitude Control

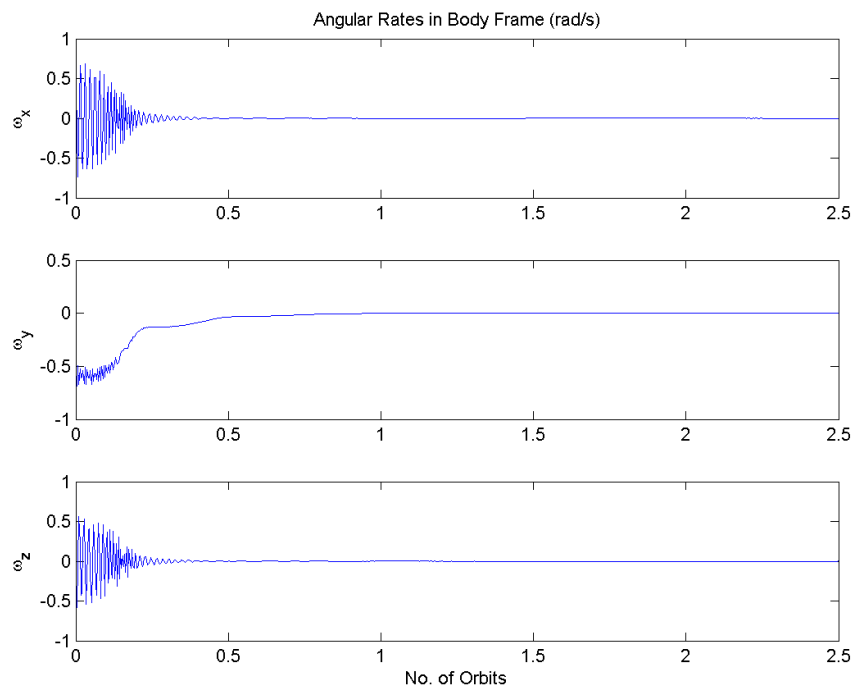


Figure 4.3: Angular rate of the satellite applying the B-dot algorithm.

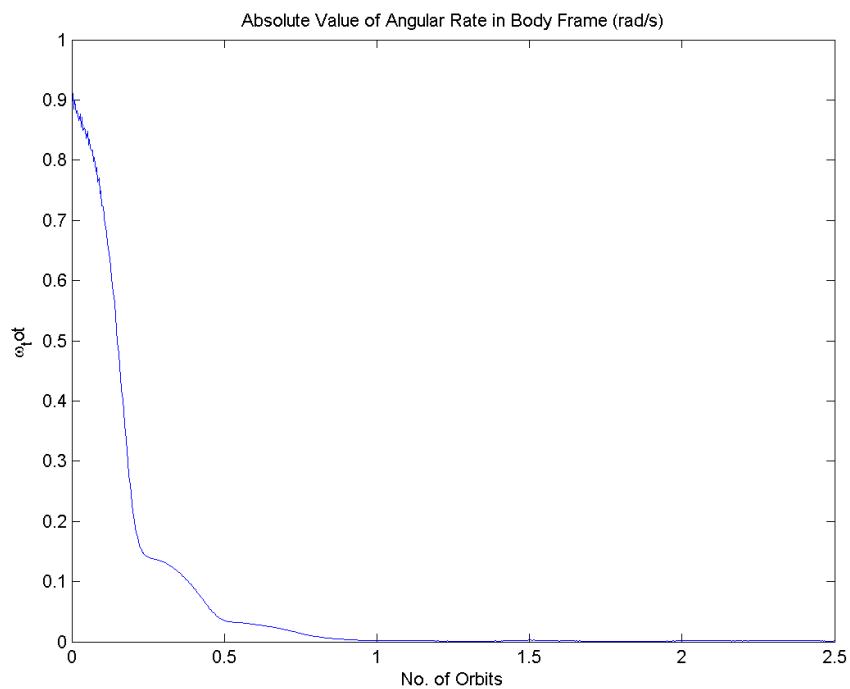


Figure 4.4: Magnitude of the angular rate of the satellite applying the B-dot algorithm.

## 4.1. Detumbling Controller

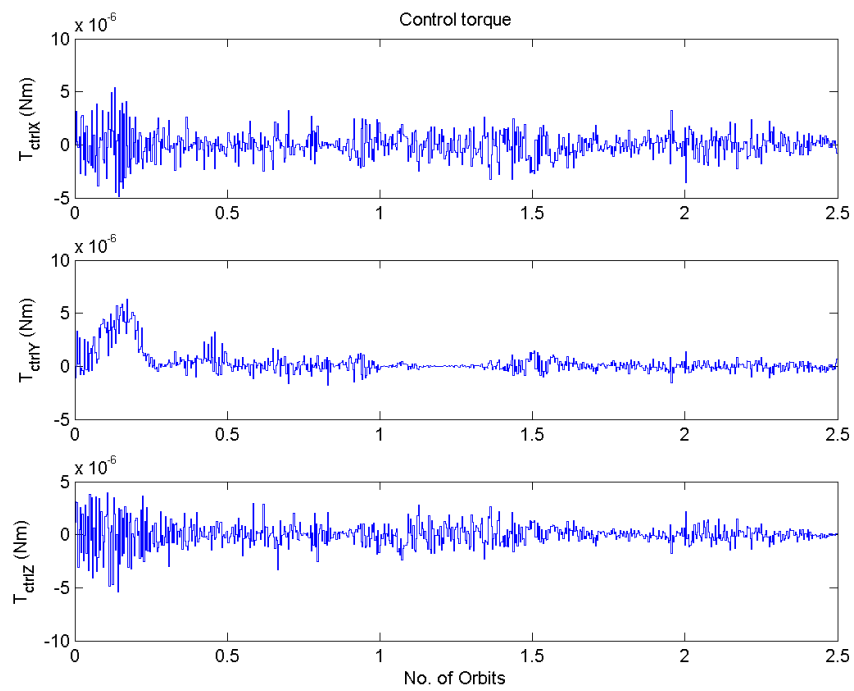


Figure 4.5: Control torque for the B-dot algorithm.

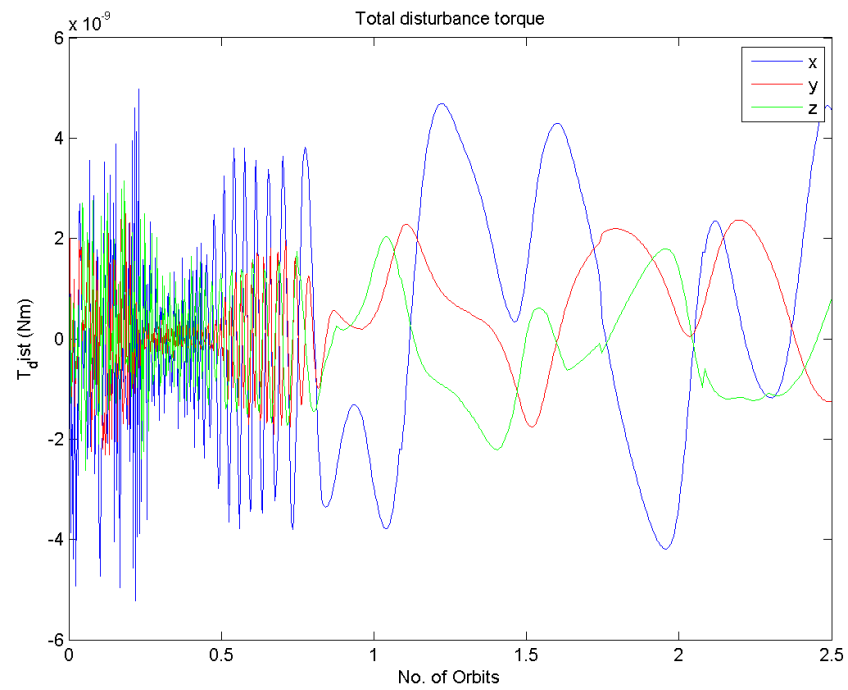


Figure 4.6: Total disturbance torque for the B-dot algorithm simulation run.

## Chapter 4. Attitude Control

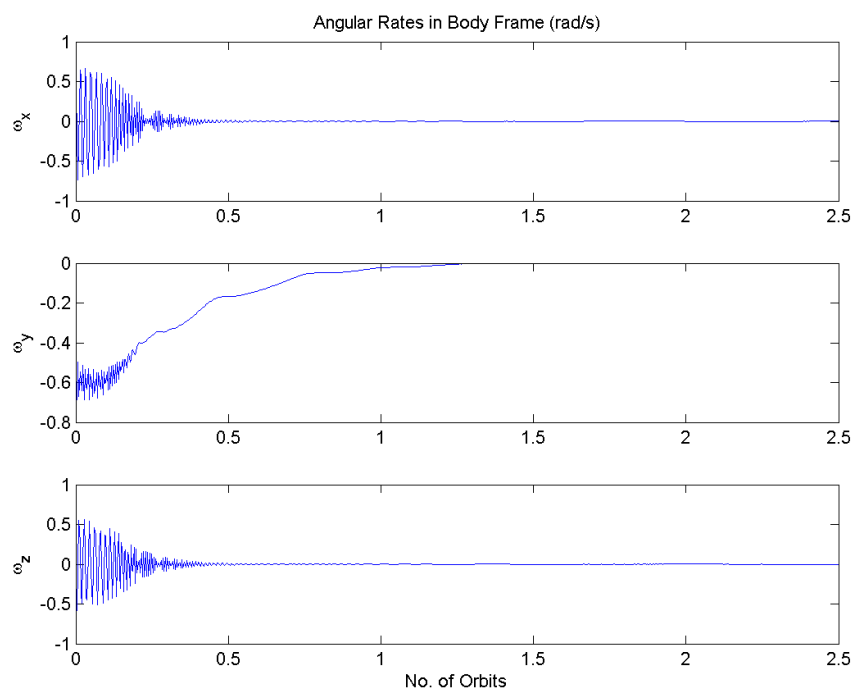


Figure 4.7: Angular rate of the satellite applying the B-dot algorithm (Y-axis coil off).

## 4.1. Detumbling Controller

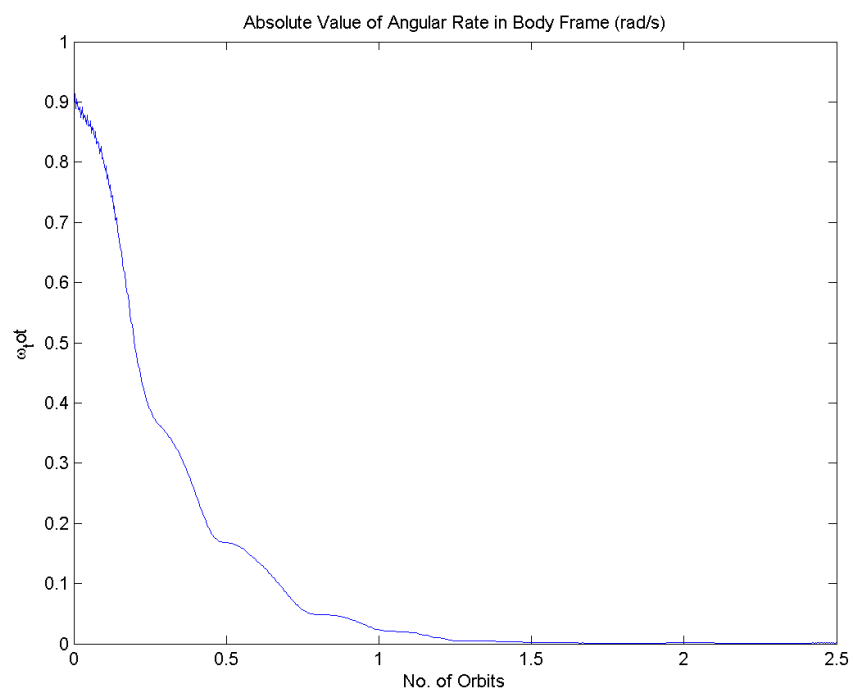


Figure 4.8: Magnitude of the angular rate of the satellite applying the B-dot algorithm (Y-axis coil off).

## Chapter 4. Attitude Control

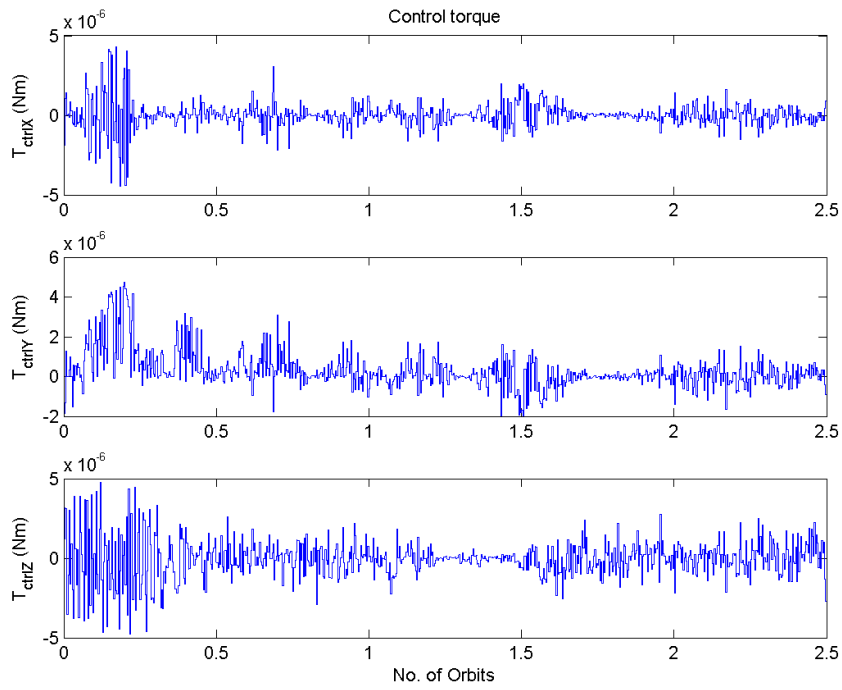


Figure 4.9: Control torque for the B-dot algorithm (Y-axis coil off).

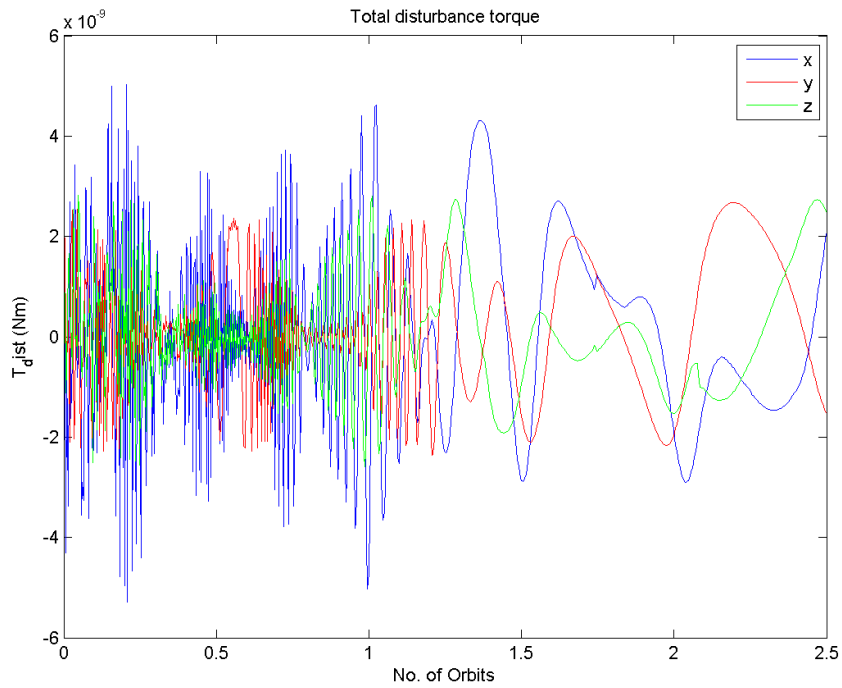


Figure 4.10: Total disturbance torque for the B-dot algorithm simulation run (Y-axis coil off).

## 4.1. Detumbling Controller

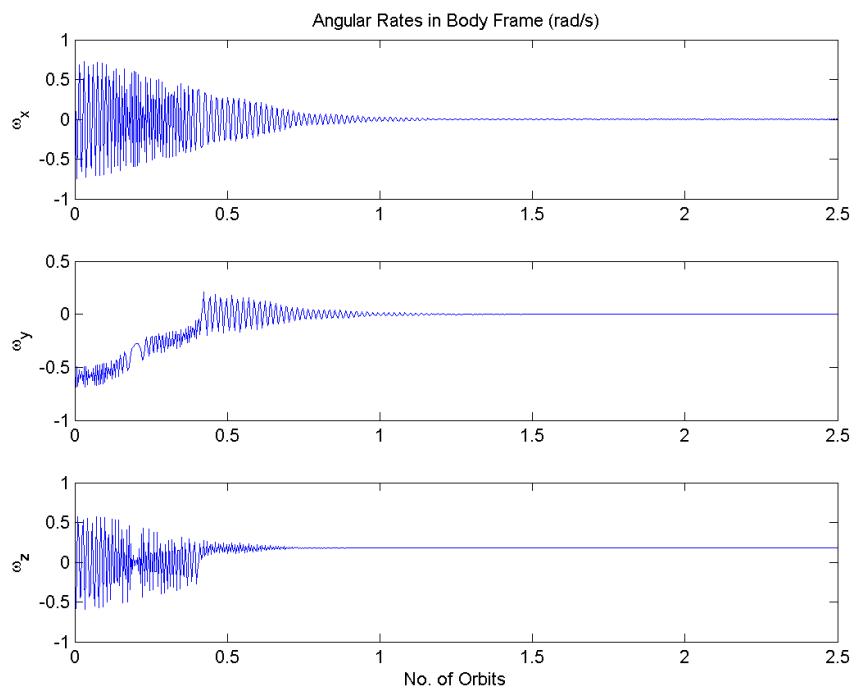


Figure 4.11: Angular rate of the satellite applying the B-dot algorithm (only Z-axis coil on).

## Chapter 4. Attitude Control

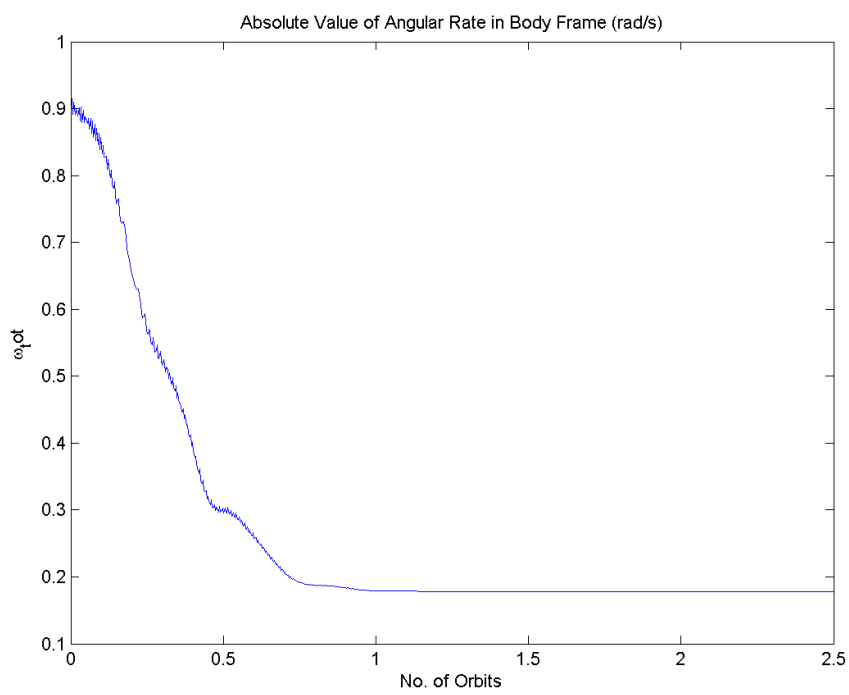


Figure 4.12: Magnitude of the angular rate of the satellite applying the B-dot algorithm (only Z-axis coil on).

## 4.1. Detumbling Controller

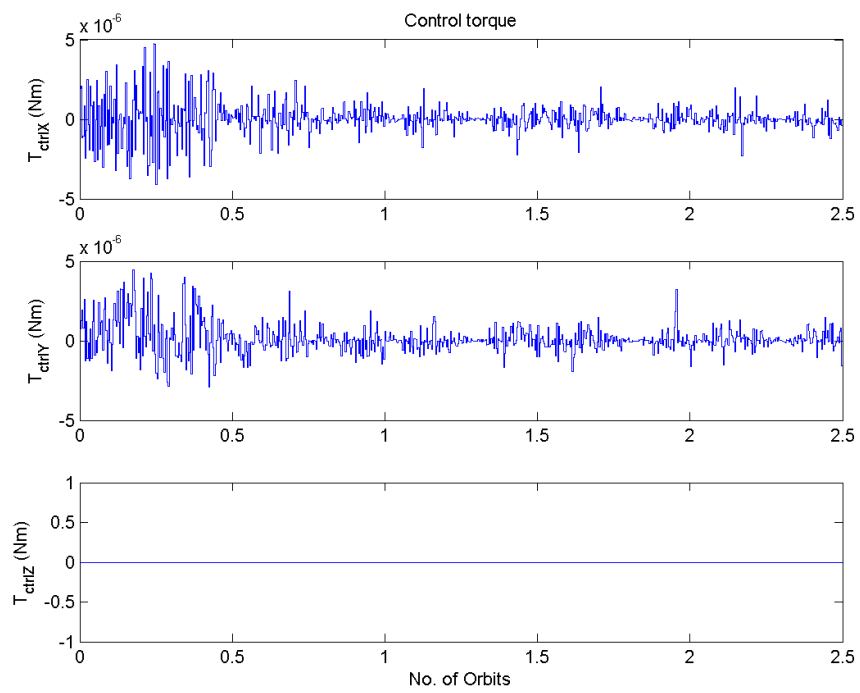


Figure 4.13: Control torque for the B-dot algorithm (only Z-axis coil on).

## Chapter 4. Attitude Control

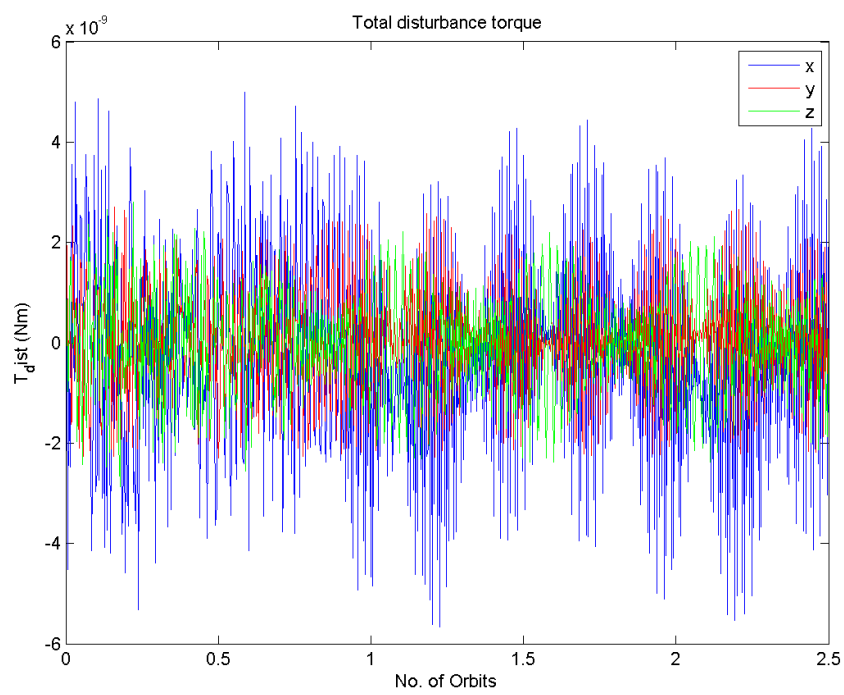


Figure 4.14: Total disturbance torque for the B-dot algorithm simulation run (only Z-axis coil on).

## 4.2 Nominal Controller

A full-state feedback controller is applied as a control scheme to stabilize the linear time-invariant system. In particular, a constant gain LQR is selected. The control law is of the form

$$\mathbf{u} = -\mathbf{K}\mathbf{x} \quad (4.11)$$

It is well known that for an infinite-horizon continuous time LQR problem, the above controller minimizes the quadratic cost functional

$$\mathbf{J} = \int_0^{\infty} (\mathbf{x}^T \mathbf{Q} \mathbf{x} + \mathbf{u}^T \mathbf{R} \mathbf{u}) dt \quad (4.12)$$

where  $\mathbf{Q}$  and  $\mathbf{R}$  are symmetric positive semidefinite and definite weighting matrices, respectively, subject to a state dynamics

$$\dot{\mathbf{x}} = \mathbf{A}\mathbf{x} + \bar{\mathbf{B}}\mathbf{u}, \mathbf{x}(0) = \mathbf{x}_0 \quad (4.13)$$

The gain matrix  $\mathbf{K}$  is given by  $\mathbf{K} = \mathbf{R}^{-1} \bar{\mathbf{B}}^T \mathbf{P}$ , where  $\mathbf{P}$  is the positive semidefinite solution of the algebraic Riccati equation

$$\mathbf{P}\mathbf{A} + \mathbf{A}^T \mathbf{P} - \mathbf{P} \bar{\mathbf{B}} \mathbf{R}^{-1} \bar{\mathbf{B}}^T \mathbf{P} + \mathbf{Q} = 0 \quad (4.14)$$

Note that the control gain  $\mathbf{K}$  renders the closed-loop system matrix  $\mathbf{A} - \bar{\mathbf{B}}\mathbf{K}$  Hurwitz.

Although the aforesaid controller is primarily intended for a linear time-invariant system (in this case, the ‘‘averaged’’ system in Eq. (2.54)), it will be applied to the satellite system, which is a nonlinear time-varying system. It is shown in Section 4.2.1 that the control law described in Eq. (4.11) exponentially stabilizes the original nonlinear system Eq. (2.23).

### 4.2.1 Averaging theory

Averaging theory will be used to show that the control law Eq. (4.11) exponentially stabilizes the linearized time-periodic system Eq. (2.52).

The use of the averaging method is to approximate the solution of a time-varying periodic system by the solution of a time-invariant ‘‘averaged’’ system (see [50], Theorem 10.4). This is possible since, via change of variables, the original nonautonomous system can be represented as a perturbation of the autonomous system. As was seen in Section 2.7.4, the linearized equations for the satellite system can be regarded as periodic.

Consider the linear periodic system

$$\dot{\mathbf{x}} = \epsilon \mathbf{F}(t)\mathbf{x} \quad (4.15)$$

where  $\mathbf{F}(t) = \mathbf{F}(t + T)$ ,  $T = 2\pi/\omega_0$  is the orbital period and  $\epsilon > 0$  is a small parameter which models the slow fluctuations of the dynamics of  $\mathbf{x}$ . Indeed, when  $\epsilon$  is small the solution  $\mathbf{x}$  will vary ‘‘slowly’’ with  $t$  relative to the periodic variation of  $\mathbf{F}(t)$ .

## Chapter 4. Attitude Control

We associate Eq. (4.15) with the autonomous average system

$$\dot{\mathbf{x}} = \epsilon \bar{\mathbf{F}}\mathbf{x} \quad (4.16)$$

where

$$\bar{\mathbf{F}} = \frac{1}{T} \int_0^T \mathbf{F}(\tau) d\tau$$

According to the averaging theory, if the averaged system is exponentially stable (i.e.  $\bar{\mathbf{F}}$  is Hurwitz), then the original nonautonomous system is also exponentially stable for a sufficiently small  $\epsilon$ .

Consider a variable change such that  $\mathbf{z}_1 = \mathbf{q}_v$ ,  $\mathbf{z}_2 = \dot{\mathbf{q}}_v/\epsilon$  and a new control input  $\mathbf{v} = \epsilon^2 \mathbf{u}$ . Let  $\mathbf{z} = [\mathbf{z}_1^T \mathbf{z}_2^T]^T$  be a state vector. Thus,  $\mathbf{x}$  and  $\mathbf{z}$  are related by the state transformation

$$\mathbf{x} = \mathbf{T}\mathbf{z} \quad (4.17)$$

where

$$\mathbf{T} = \begin{bmatrix} \mathbf{E}_{3 \times 3} & \mathbf{0}_{3 \times 3} \\ \mathbf{0}_{3 \times 3} & \epsilon \mathbf{E}_{3 \times 3} \end{bmatrix}$$

The system in Eq. (2.54) can now be written in terms of the new state and input vectors as

$$\dot{\mathbf{z}} = \epsilon(\tilde{\mathbf{A}}\mathbf{z} + \tilde{\mathbf{B}}\mathbf{v}) \quad (4.18)$$

where

$$\tilde{\mathbf{A}} = \frac{1}{\epsilon} \mathbf{T}^{-1} \mathbf{A} \mathbf{T}, \quad \tilde{\mathbf{B}} = \frac{1}{\epsilon^3} \mathbf{T}^{-1} \bar{\mathbf{A}}$$

From this point, it suffices to show that the autonomous averaged system in Eq. (4.18) is exponentially stable under the full state feedback control law  $\mathbf{v} = \epsilon^2 \mathbf{u}$ , where  $\mathbf{u} = -\mathbf{K}\mathbf{x}$ . The exponential stability of the z-dynamics is assured regarded the exponential stability of the averaged x-dynamics for the transformation in Eq. (4.17) is linear.

The control input  $\mathbf{v}$  can be expressed as

$$\mathbf{v} = -\tilde{\mathbf{K}}\mathbf{z}$$

where  $\tilde{\mathbf{K}} = \epsilon^2 \mathbf{K} \mathbf{T}$ . Then, the closed-loop system can be expressed as

$$\dot{\mathbf{z}} = \epsilon(\tilde{\mathbf{A}} - \tilde{\mathbf{B}}\tilde{\mathbf{K}})\mathbf{z}$$

On the other hand, using Eq. (4.18) we have that

$$\begin{aligned} \epsilon \mathbf{T}(\tilde{\mathbf{A}} - \tilde{\mathbf{B}}\tilde{\mathbf{K}})\mathbf{T} &= \mathbf{T}(\mathbf{T}^{-1} \mathbf{A} \mathbf{T} - \mathbf{T}^{-1} \tilde{\mathbf{B}} \mathbf{K} \mathbf{T}) \mathbf{T}^{-1} \\ &= \mathbf{A} - \bar{\mathbf{B}} \mathbf{K} \end{aligned}$$

As is shown in Section 4.2.2,  $\mathbf{A} - \bar{\mathbf{B}}\mathbf{K}$  is Hurwitz. Consequently, the closed-loop system matrix  $\tilde{\mathbf{A}} - \tilde{\mathbf{B}}\tilde{\mathbf{K}}$  is Hurwitz as well. This implies that the average system is exponentially stable. It follows that the control law in Eq. (4.11) exponentially stabilizes the linearized time-periodic system in Eq. (2.52). This is the same result as in [27].

### 4.2.2 Simulations

This section presents some representative simulations carried out to assert the performance of the LQR controller presented earlier. A vast amount of simulation runs were carried out to verify the performance of this attitude control method.

The orbit parameters used for these simulations are those of a polar orbit with an inclination of nearly  $99^\circ$  and an orbit height of close to 650 km. These parameters imply an orbital period of 98 min and  $\omega_0 = 0.011$  rad/s. This kind of orbit is typical for CubeSats. The inertia tensor of the spacecraft is given as  $I = \text{diag}([4.8 \ 6.0 \ 3.5]^T) \cdot 10^{-3} \cdot \text{kg} \cdot \text{m}$  and the Control Reference Frame is assumed to coincide with the Body Reference Frame.

For the LQR gain matrix  $\mathbf{K}$  computation,  $\mathbf{R} = \mathbf{E}_{3 \times 3}$  and a heuristic method as proposed in [3] has been used to define the weighting matrix  $\mathbf{Q}$ , which is given by the following form

$$\mathbf{Q} = 0.5 \cdot q^2 \begin{bmatrix} k_1^2 & 0 & 0 & k_1 k_2 & 0 & 0 \\ 0 & k_1^2 & 0 & 0 & k_1 k_2 & 0 \\ 0 & 0 & k_1^2 & 0 & 0 & k_1 k_2 \\ k_1 k_2 & 0 & 0 & k_2^2 & 0 & 0 \\ 0 & k_1 k_2 & 0 & 0 & k_2^2 & 0 \\ 0 & 0 & k_1 k_2 & 0 & 0 & k_2^2 \end{bmatrix} \quad (4.19)$$

where the weighting parameters have been set to  $k_1 = 0.001$ ,  $k_2 = 0.00001$  and  $q = 20000$ . A remark about the form of the weighting matrix is that the constant parameter  $k_1^2$  penalizes deviations in the quaternion vector, the constant parameter  $k_2^2$  penalizes deviations in the quaternion vector rates and the parameter product  $k_1 k_2$  penalizes the cross-products.

The choosing of these weighting matrices  $\mathbf{Q}$  and  $\mathbf{R}$  yields the following eigenvalues for the closed-loop system matrix  $\mathbf{A} - \bar{\mathbf{B}}\mathbf{K}$ :

$$(-0.0004 \pm 0.0018i, -0.0004 \pm 0.0006i, -0.0011 \pm 0.0007i)$$

The initial conditions are

$$\begin{aligned} [\omega_{1o} \ \omega_{2o} \ \omega_{3o}]^T &= [+2 \ +1 \ -2]^T \text{ }^\circ/\text{s} \\ (\text{Roll}, \text{Pitch}, \text{Yaw}) &= [+20 \ -32 \ -88]^T \text{ }^\circ \end{aligned}$$

It is noteworthy that these initial conditions are largely distanced from the equilibrium, even further from what is usually considered in other works [27,51,52]. The idea behind this is to demonstrate the robustness of the controller when the system is not close to the reference, i.e. when the system exhibits a clear nonlinear behaviour.

Figures 4.15 to 4.18 demonstrate the application of the nadir pointing controller (Eq. (4.11)) on the nonlinear system (Eqs. (2.23) and (2.31)), without any external perturbations added.

## Chapter 4. Attitude Control

As can be seen in Fig. 4.15, from the second orbit onward the attitude angles remains in the  $\pm 10$  degree window, whereas Fig. 4.16 shows that the angular velocity drops close to zero after the first orbit.

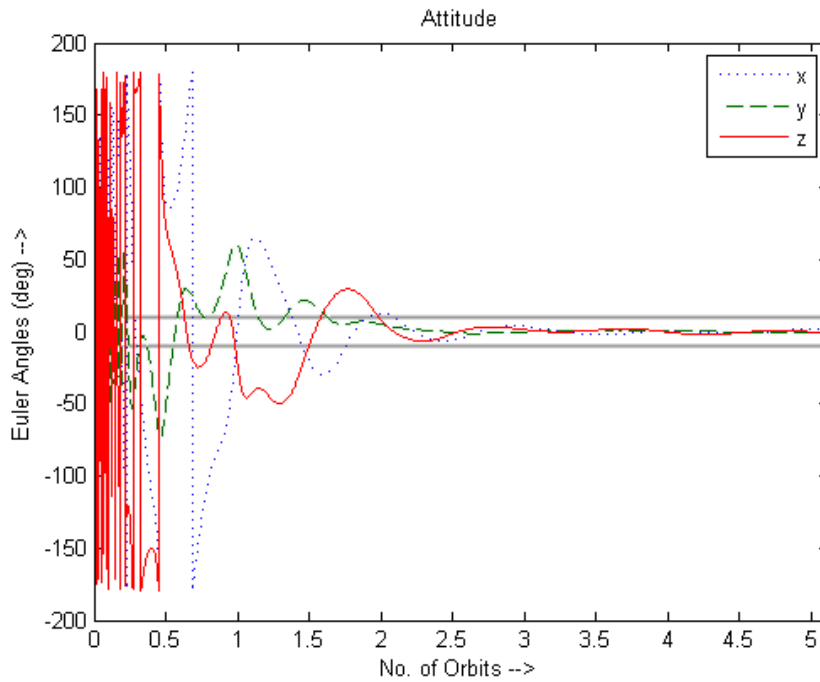


Figure 4.15: Attitude Euler Angles

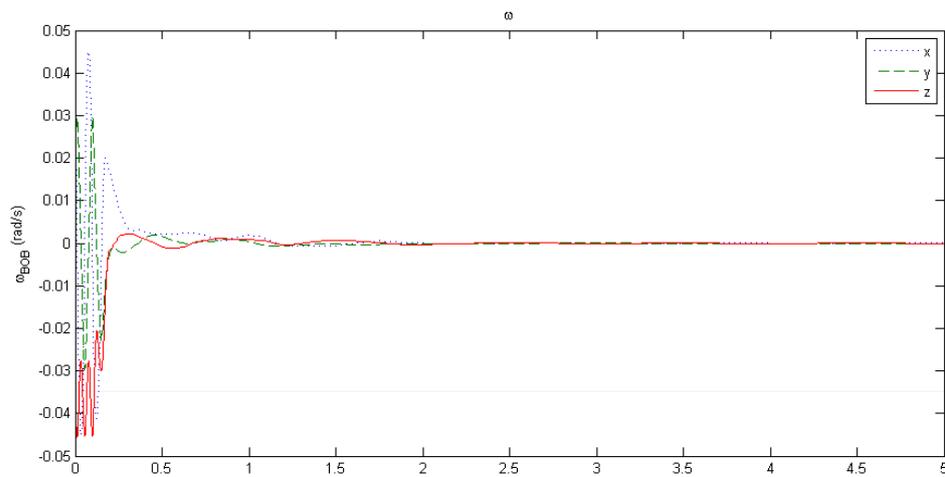


Figure 4.16: Body Angular Rate

4.2. Nominal Controller

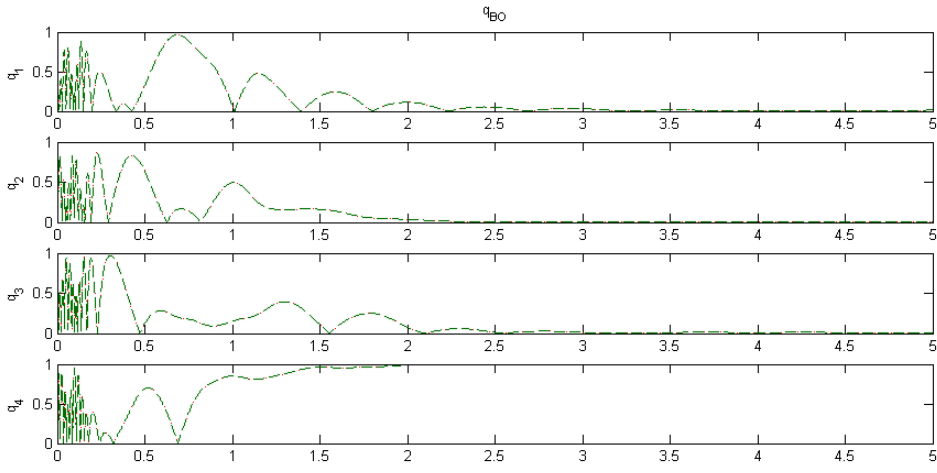


Figure 4.17: Attitude Quaternion

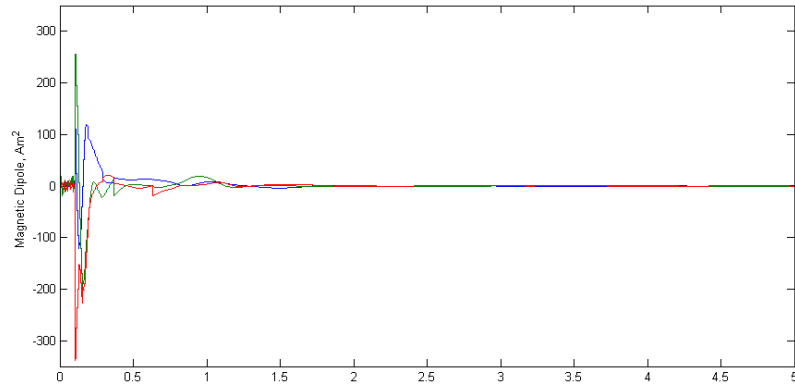


Figure 4.18: Applied Magnetic Dipole

Figures 4.19 to 4.22 demonstrate the application of the same controller on the same system, but this time with external perturbations added. Perturbations considered include aerodynamic drag, gravity gradient and solar pressure.

In this case, roll, pitch and yaw set inside the  $\pm 10$  degree window after the fourth orbit, as can be seen in Fig. 4.19.

## Chapter 4. Attitude Control

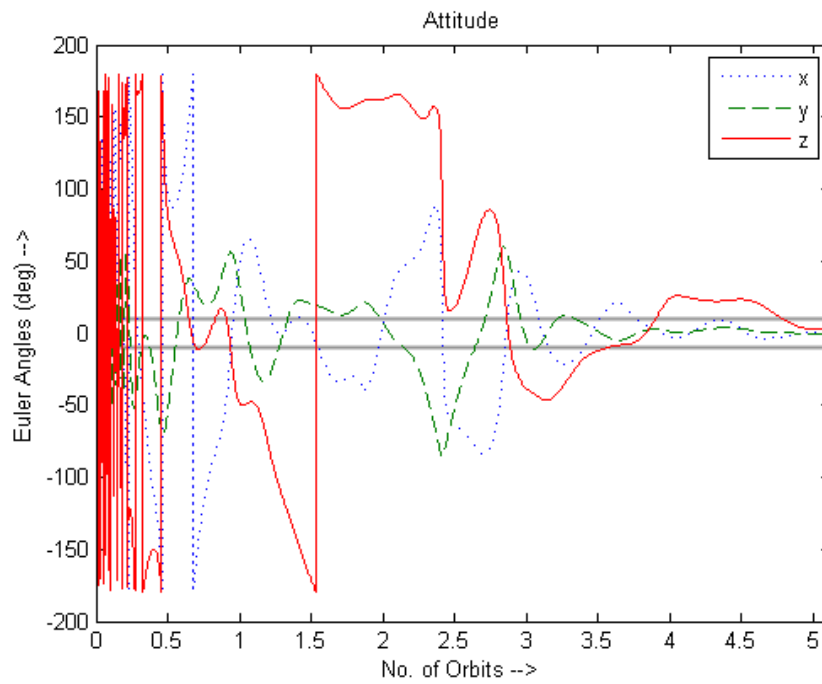


Figure 4.19: Attitude Euler Angles (with perturbances)

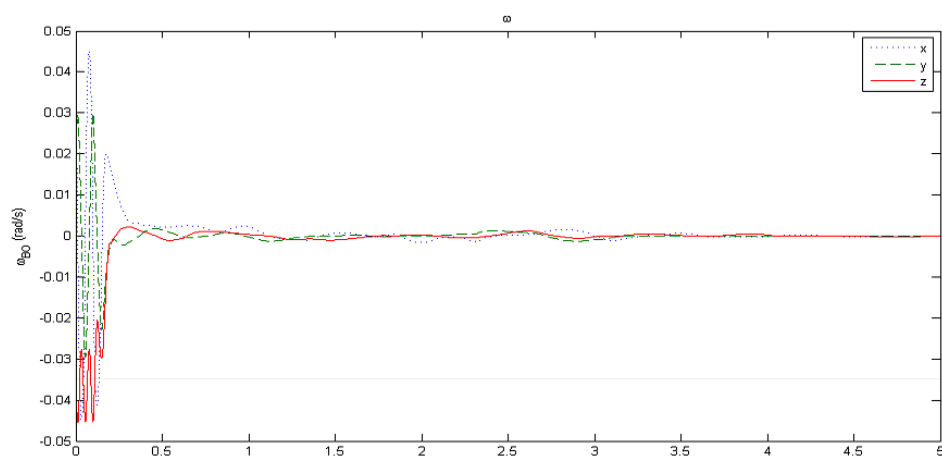


Figure 4.20: Body Angular Rate (with perturbances)

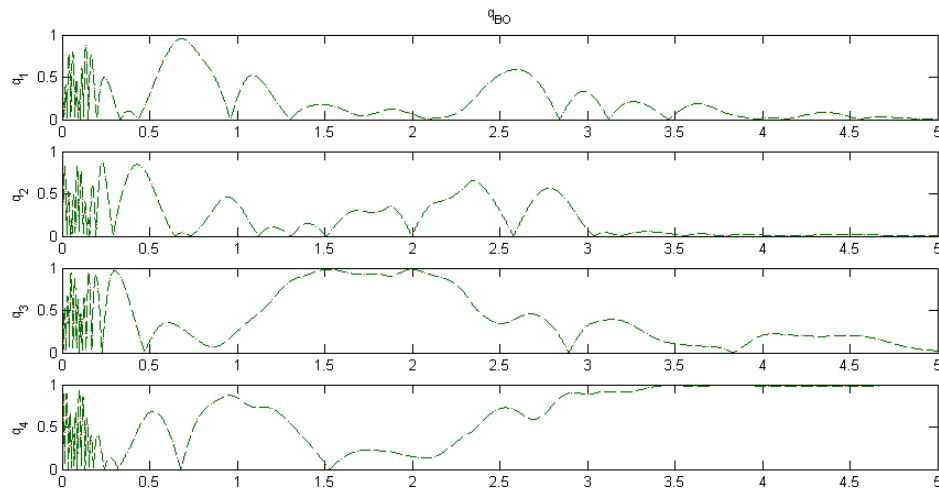


Figure 4.21: Attitude Quaternion (with perturbances)

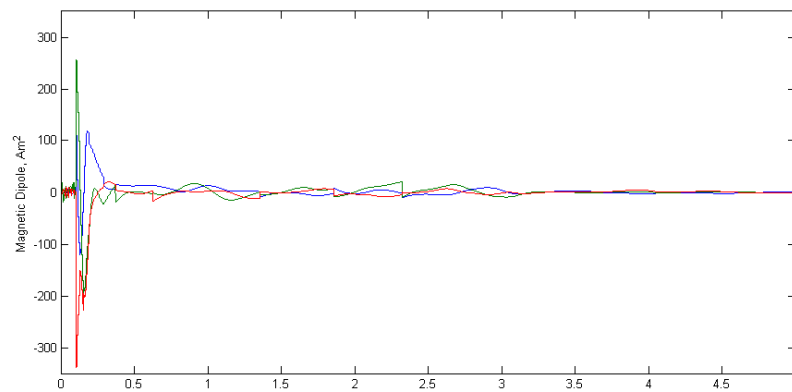


Figure 4.22: Applied Magnetic Dipole (with perturbances)

## 4.3 Summary

In this chapter, the two attitude controllers to be used in the two different control phases were presented. In the case of the detumbling phase, the trustworthy B-dot control law was introduced and a controller based on it was developed. In the case of the nominal pointing phase, a LQR based controller was designed.

Theoretical background along with computer simulations of both controllers were also presented in order to show the feasibility of the controllers.

This page has been intentionally left blank.

# Chapter 5

## AntelSat Simulation Environment

Testing the attitude estimators and controllers for the spacecraft is of paramount importance to evaluate their performance. However, a total physical replication of the characteristics of the environment in space—vacuum, zero gravity and temperature conditions—is not a viable option for the vast majority of the CubeSat projects as the costs involved are prohibitive. Typically, a realistic simulator is used instead. The latter simulates the orbit and attitude dynamics of the spacecraft together with disturbances. Attitude estimator and controllers implementations are also included, as well as actuator and sensor models.

Section 5.1 commences the chapter by giving a general description of the simulation environment developed for Simulink and of the models used in it. Section 5.2 continues with a more detailed description of the models used to generate the reference vectors. In particular, Section 5.2.1 treats the orbit propagator, Section 5.2.2 deals with the magnetic field model, Section 5.2.3 handles the Sun vector model and Section 5.2.4 approaches the eclipse model. Section 5.3 follows with the different actuator and sensor models. More specifically, Sections 5.3.1 to 5.3.3 address the models used for the magnetometer, Sun sensors and gyroscope, respectively. Section 5.3.4 closes the chapter with the magnetorquer model.

### 5.1 Introduction

The simulator for carrying out closed loop simulations was developed under MATLAB as a Simulink model and was mainly based on [6, 13, 20]. For the orbital propagators and the reference vectors models, publicly available libraries were used (see more in the correspondent sections below). Simulink implies a very fluid and visual way of working, since every part of the system can be represented with blocks and these can be interconnected with arrowed lines.

Figure 5.1 shows the content of the top hierarchical block of the simulator. The green block (block number 1 in the picture) incorporates the spacecraft kinematics and dynamics models, as well as the disturbances torque models. The orange block (block number 2) includes the hardware of the spacecraft that interacts with the environment, i.e. sensors and actuators. Lastly, the blue block (block number 3)

## Chapter 5. AntelSat Simulation Environment

consists of the determination and control algorithms that run onboard.

The rest of the models involved in the simulations, the "truth" or real models, are computed offline beforehand and the results are saved as files. They are calculated once and their results are used for various simulations. When the simulator runs, these files are loaded and used as inputs. The "truth" models give the true translational position and velocity of the spacecraft in the orbit, the geomagnetic field, and the Sun and eclipse model for each point on this orbit. This offline pre-computation is done in such a way since the translational motion of the satellite is independent of its rotational motion and any change in the orbit is disregarded for the period of time considered in the simulations. Splitting the total amount of calculations and reusing the offline results for various simulation runs achieves vast time savings.

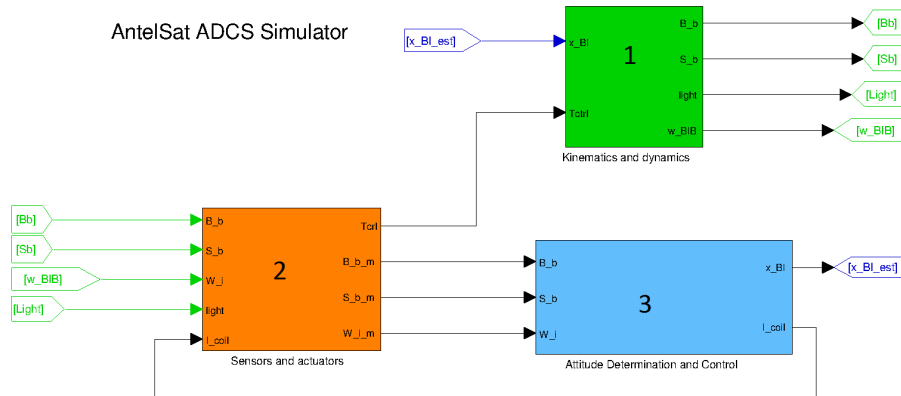


Figure 5.1: Top hierarchical block of the AntelSat attitude simulator.

The green block including the spacecraft dynamics and disturbance torques blocks contains the equations discussed in Sections 2.4 and 2.5, respectively, and will not be treated furthermore in this chapter.

Some outputs from the true models are converted to the BRF and these resultant signals are taken by the sensor models to simulate realistic outputs from gyroscopes, Sun sensors and magnetometers. This is described further in Section 5.3.

## 5.2 Reference Models

The truth models are used to calculate the true translational motion of the satellite through its orbit, as well as the true Sun vector and geomagnetic field on the points

of the orbit.

For ascertaining the spacecraft position the Simplified General Perturbations (SGP4) orbital propagator is used. Inputs needed for this model are the Julian Date and the orbital parameters for the satellite, obtained through the Two Line Element (TLE) provided by NORAD [53].

For the geomagnetic model, the International Geomagnetic Reference Field (IGRF) model is used [54], whereas an algorithm as in [55] is employed to obtain the Sun vector.

Validation of the models used in Simulink and their implementations in C was performed together with the software development group, see [56].

### 5.2.1 Orbit Propagators

A general description of orbits and their elements, as well as Two Line Elements (TLE) was previously presented in Section 2.1. In order to generate the attitude reference vectors, a method for finding the translational state of the satellite on its orbit must be implemented. A numerical way of computing position and velocity of the spacecraft is used for the AntelSat, i.e. an orbital propagator. One of the most widely used orbital propagators in CubeSat projects is the Simplified General Perturbation version 4 (SGP4) model. This model is used for near-Earth objects—objects with orbital periods up to 255 minutes. Publicly available code was first published in FORTRAN and nowadays can be found both in MATLAB and C++ [57].

Satellite translational motion models can be classified according to how the equations of motion are solved. There are two general classifications: general perturbations and special perturbations. General perturbation models involve solving the equations of motion analytically. On the other hand, special perturbation models involve solving the equations of motion through numerical integration. Although special perturbation models are generally more accurate and less complicated than general perturbation models, they are computationally expensive. The SGP model is an example of a general perturbations model. SGP4 considers perturbing accelerations due to the oblateness of the Earth, asymmetry of the Earth’s mass about the equatorial plane, and atmospheric drag [58].

As aforementioned, it takes both the Julian Date and the TLE provided by NORAD as input. Position errors yielded in the SGP4 are due to different causes. First off, the accuracy of the TLE elements at epoch is in the order of a few kilometers. Secondly, after one week SGP4 position errors are about 100 km. On top of that, any lack of synchrony in the onboard real time clock will also add to the total errors. For these reasons, a daily update of the TLE is advised and onboard TLE data that is more than one week old is not taken into account.

### 5.2.2 Magnetic Field Model

As treated in Section 2.4.4, the magnetic field surrounding the Earth is created by a combination of sources, but more than 90% of this field is generated internally

## Chapter 5. AntelSat Simulation Environment

to the planet. This portion is called the Main Field and can be described with different mathematical models. The model used in the simulator and onboard the satellite is the IGRF published by the International Association of Geomagnetism and Astronomy (IAGA). The IAGA also publishes code of the implementation of this model written in C and the needed coefficients for it [26]. In the attitude simulator, this code is used together with a wrapper for MATLAB.

### 5.2.3 Sun Vector Model

The Sun vector is calculated using an algorithm similar to the one in [55]. The Sun model is used to get the Sun vector in the inertial ECI frame. This inertial vector is then transformed to the satellite body frame using both satellite orbit and attitude information. The algorithm uses a simple technique and yields results of modest accuracy. However, these results suffice for the application.

The algorithm takes the time elapsed since the reference epoch. This epoch is the J2000 epoch, that is, 1st January 2000, 12:00:00 PM, or 2451545.0 Julian Date (JD). The input time is in Julian Date and the elapsed Julian centuries  $t_{UT}$  is calculated

$$t_{UT} = \frac{t_{JD} - 2451545}{36525} \quad (5.1)$$

Then, the mean anomaly and mean longitude of the Sun,  $\lambda_{M_\odot}$  and  $M_\odot$  respectively, are given by

$$\begin{aligned} \lambda_{M_\odot} &= 280.460^\circ + 36000.77 t_{UT} \\ M_\odot &= 357.5277233^\circ + 35999.05034 t_{UT} \end{aligned} \quad (5.2)$$

Since the Sun travels in an eccentric orbit with respect to the Earth, the ecliptic longitude of the Sun is introduced to account for the corrections in the mean longitude

$$\lambda_{ecliptic} = \lambda_{M_\odot} + 1.914666471^\circ \sin(M_\odot) + 0.019994643 \sin(2M_\odot) \quad (5.3)$$

The obliquity of the Sun can be approximated using a first-order model, thus yielding a linear model of the ecliptic of the Sun  $\epsilon$

$$\epsilon = 23.439291^\circ - 0.0130042 t_{UT} \quad (5.4)$$

Lastly, the unit Sun vector is given in the inertial frame as

$$\hat{\mathbf{s}}_{ECI} = \begin{bmatrix} \cos(\lambda_{ecliptic}) \\ \sin(\lambda_{ecliptic}) \cdot \cos(\epsilon) \\ \sin(\lambda_{ecliptic}) \cdot \sin(\epsilon) \end{bmatrix} \quad (5.5)$$

### 5.2.4 Eclipse model

The satellite will be around a third of the length of its orbit in shadow, the eclipse model is needed to know whether the satellite is in eclipse or not for a certain time instant. The spacecraft is assumed to be a point mass, whereas the Sun and the Earth are assumed to be spheres of finite size. When the satellite is in shadow, the Sun sensors give null readings.

This algorithm take the outputs of the Sun vector and the SGP4 models (position vector of the satellite in the ECI frame) as inputs. It outputs a boolean with values 0 if the spacecraft is in eclipse and 1 if the spacecraft is illuminated by the Sun.

## 5.3 Sensor and Actuator Models

Sensor models are introduced to achieve more realistic simulations, inserting noise in the measurements inputs for the attitude estimators and controllers. White Gaussian noise is added to the measurements. These models are treated in Sections 5.3.1 to 5.3.3. The actuator model translates the control outputs from the attitude controller into torques acting on the satellite dynamics. This model is presented in Section 5.3.4.

The complexity of both actuators and sensors models was kept in a level that would both yield realistic enough results and keep total simulation run times low. In the case of the magnetometer and gyroscope, for a quantity  $q$  measured at instant  $k$ , the models considered for this work are of the following form:

$$\hat{q}_k = q_k + \varepsilon_{bias} + \varepsilon_{noise} \tag{5.6}$$

where  $\hat{q}_k$  is the measured value  $\varepsilon_{bias}$  is the bias of the measurement and  $\varepsilon_{noise}$  is Gaussian noise.

Figure 5.2 show the sensors and actuators top block and Fig. 5.3 display a detail of the block with all the sensors models.

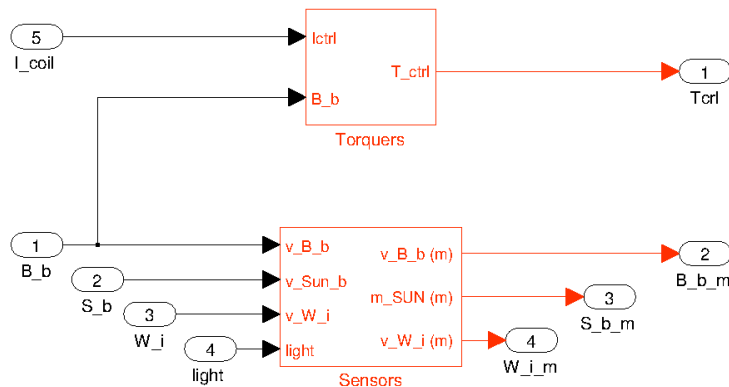


Figure 5.2: Sensors and actuators top block.

## Chapter 5. AntelSat Simulation Environment

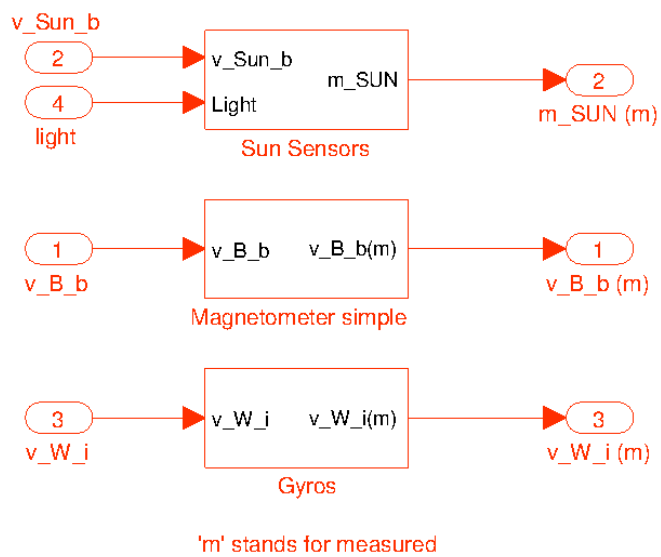


Figure 5.3: Sensors block in detail.

### 5.3.1 Magnetometer Model

The magnetometer model outputs noisy magnetic field measurements in the BRF. It takes as input the geomagnetic field vector from the truth model, rotated from the ECI to the BRF. Gaussian noise and a constant bias are then added to the input. Values for the noise variance and bias are based on measurements taken in the flight hardware. Figure 5.4 presents the magnetometer model block.

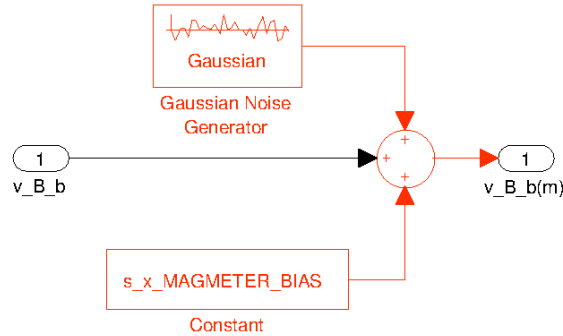


Figure 5.4: Magnetometer model.

### 5.3.2 Sun Sensors Model

The Sun sensors consist of six directional light transducers each of which outputs a current depending on the angle made by the sensor normal with the Sun vector based on a cosine law

$$I = I_o \cos(\theta) \tag{5.7}$$

where  $I_o$  is the maximum intensity of the sensor when the angle is zero. A current-to-voltage converter circuit is placed before the 12-bit ADC of the microcontroller to obtain voltage readings of the light transducers.

The Sun sensors Simulink model outputs six different noisy Sun intensity measurements, one for each Sun sensor placed on every face of the AntelSat. It takes as input the Sun vector from the truth model, rotated from the ECI to the BRF. A dot product is then performed between this real Sun vector in the BRF and a constant corresponding to each Sun sensor—e.g. the constant is  $[100]$  for the Sun sensor in the  $+X$  face,  $[-100]$  for the one on  $-X$ , etc. The resultant vector from this dot product is then multiplied by the output of the real eclipse model—when the satellite is in eclipse, the output of the eclipse model is zero, thus the output of the Sun sensors are also zero. ADC saturation and gain are then simulated. Finally, Gaussian noise is added and the ADC quantization is also simulated. Values for the noise variance are estimated. Figure 5.5 presents the model block for an individual Sun sensor.

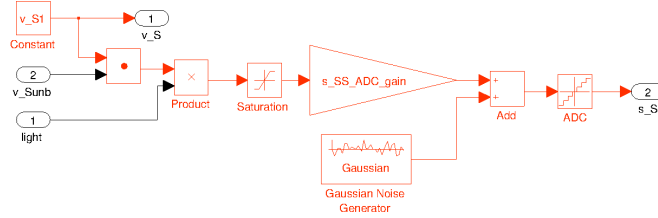


Figure 5.5: Model of an individual Sun sensor.

The output of this Sun sensors model block goes to the determination block, where the Sun vector is computed. At least three Sun sensors detecting the Sun at a time are needed to correctly determine the Sun vector. In order to construct the latter, the outputs of the three solar cells facing the Sun are selected, say  $\mathbf{c}_i$ ,  $\mathbf{c}_j$  and  $\mathbf{c}_k$  with corresponding voltage output  $V_i$ ,  $V_j$  and  $V_k$ . For computing the normalized Sun vector in the body frame  $\hat{\mathbf{s}}_B$ , for each of the selected sensors we have:

$$\mathbf{c}_m^T \mathbf{s}_B = \cos(\theta_m) = \frac{V_m}{V_o} = kV_m \quad \text{for } m=i,j,k \quad (5.8)$$

After combining the three corresponding equations and representing them as a matrix, it yields the following expression

$$\begin{aligned} C_m \mathbf{s}_B &= k \mathbf{V}_m \\ \hat{\mathbf{s}}_B &= \frac{k C_m^{-1} \mathbf{V}_m}{\|k C_m^{-1} \mathbf{V}_m\|} \end{aligned} \quad (5.9)$$

It is worth noting that knowledge of the constant  $V_o$  (or  $k$ ) is not needed for the calculation of the normalized vector.

### 5.3.3 Gyroscope Model

The gyroscope model outputs noisy measurements of the angular rate of the BRF w.r.t. the ECI. It takes the output of the angular rate computed in the dynamics blocks as input. Gaussian noise and a constant bias are then added to the input. Values for the noise variance and bias are based on the datasheet of the selected sensor model and estimations. A drift term has not been included in the model since the chosen gyroscope measures using the Coriolis effect and therefore suffers no drift. Figure 5.6 presents the gyroscope model block.

### 5.3. Sensor and Actuator Models

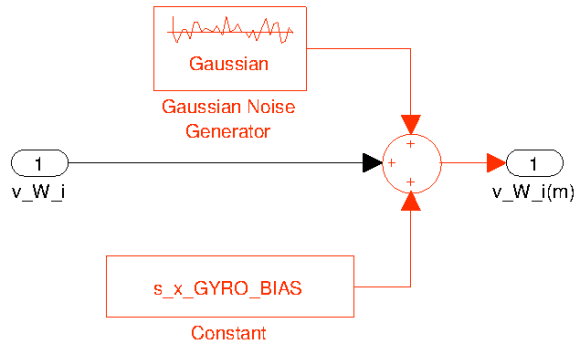


Figure 5.6: Gyroscope model.

#### 5.3.4 Magnetorquer Model

The magnetorquer model takes the current output vector from the attitude controller as input. A zero-order hold and quantization blocks are added to simulate PWM. The resultant signal is then multiplied by the effective area of the coils to obtain the control dipole, as in Eq. (2.24). This intermediate signal is then multiplied by the geomagnetic field vector in the BRF, giving the control torque as the output of the block, as in Eq. (2.26). Figure 5.6 presents the magnetorquer model block.

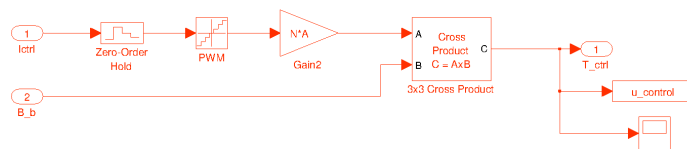


Figure 5.7: Magnetorquer model.

## 5.4 Summary

This chapter introduced the simulation environment developed for AntelSat, which was based on different other aforementioned works. This environment provides a key tool for the analysis of the AntelSat mission and the development of both the determination and control algorithms. The simulator blocks include the equations of motion of the satellite.

Among other things, the blocks also include an orbit propagator and real eclipse, Sun vector and geomagnetic field models. On top of that, the simulation environment also incorporates models for the actuators and sensors selected for the AntelSat mission.

# Chapter 6

## AntelSat Hardware

### 6.1 Introduction

The spacecraft ADCS uses primarily low power and low cost sensors and actuators in order to provide time permissible attitude stabilization with a pointing accuracy of  $\pm 10$  degrees in each axis.

Regarding the attitude determination, sensors available in the satellite are one 3-axis magnetometer, three 1-axis gyroscopes and six different Sun sensors. The Sun sensors are composed of one photodiode, one for each of the sides of the spacecraft. All these sensors are connected to the ADCS microcontroller which is responsible for handling the attitude data.

Attitude control relies on magnetic actuation only, using three different magnetorquers. The magnetorquers, like the gyroscopes, are aligned with the geometrical axes of the body of the spacecraft. The coils are commanded by the ADCS microcontroller using pulse width modulation (PWM). The interface between the microcontroller and the coils is composed of H-Bridges which are in charge of dealing with the currents circulating through the magnetorquers.

At the time of starting this thesis, the configuration of sensors and actuators to be used in the AntelSat ADCS had already been chosen. The selection was mainly based on the conclusions of an antecedent in the AntelSat project and is justified since it is common among other CubeSat projects [59]. Another pivotal decision regarding the fabrication of the spacecraft was to outsource the side panels which included solar panels. The selected solar panels were GomSpace's NanoPower P110UC series [60]. An advantage of this model is that the panels for the +X, +Y and +Z faces include a 1-axis gyroscope and a magnetorquer embedded in their 10 layer PCB. Figure 6.1 presents a diagram of the ADCS with its sensors and actuators, also indicating the interfaces used for communication.

Actuators for the AntelSat are explained in more detail in Section 6.2, whereas sensors are treated in Section 6.3. Finally, Section 6.4 addresses general aspects of the design of the hardware. However, explaining the development of both the hardware prototypes and flight version is not the main objective of this document and for this reason it will only be presented in a concise way.

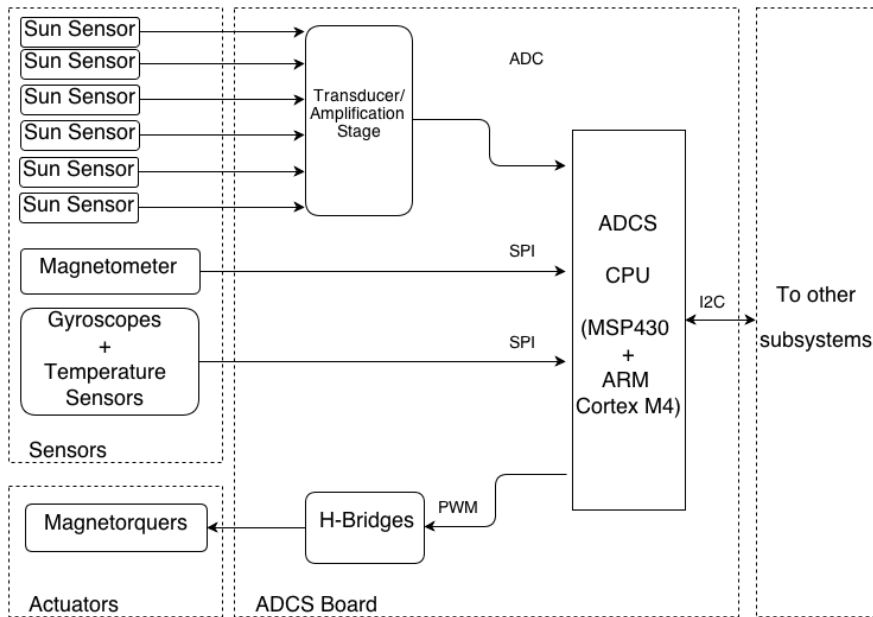


Figure 6.1: ADCS diagram with sensors and actuators.

## 6.2 Attitude Actuators

Attitude control for the AntelSat relies on magnetorquers solely. The magnetorquers main components, the electromagnetic coils, are embedded into the solar panels and are manufactured by GomSpace Aps. Section 6.2.2 presents the specifications for the magnetorquers.

The following is a very brief summary of the most common methods and actuators used to control satellites and is presented as a reference for the reader.

### Passive Control Techniques

- Gravity Boom:** it relies on the gravity-gradient stabilization method, which is based on the fact that an elongated object in a gravity field tends to align its longitudinal axis through the Earth's center. It offers a typical accuracy of  $\pm 5^\circ$  in two controlled axes. The orientation about the nadir vector is unconstrained [1]. This type of control is not suitable for spacecrafts which comply with the CubeSat standard: a two unit CubeSat would have to possess an expandable gravity boom which would require precious onboard space.
- Permanent Magnet:** A permanent magnet forces an alignment of the satellite body with the geomagnetic field. If the satellite is detumbled, it can provide two axis stabilization with a pointing accuracy within  $\pm 5^\circ$ . However, a permanent magnet cannot reduce the kinetic energy of the spacecraft, that is, it cannot remove oscillation from the satellite.
- Spin Control:** Spin stabilization is a passive control technique that stabilizes a satellite in two axes using the gyroscopic effect created by rotating

the entire spacecraft around the remaining axis. As the satellite rotates, its angular momentum vector remains approximately fixed in inertial space [1]. This method is generally disregarded for CubeSats: the rotation is achieved using thrusters and storing the required fuel takes up much volume, which is a vital resource for this type of satellites.

### Active Control Techniques

- **Thrusters:** Thrusters are reaction engines, i.e. they obtain thrust in conformity with Newton’s third law. They expel propellant at high velocity in one direction, accelerating the satellite in the opposite direction with a force of equal magnitude. The amount of propellant stored onboard determines the lifetime of the ADCS. Since volume is a scarce resource in satellites that comply with the CubeSat standard, thrusters are not usually considered for these kind of missions.
- **Momentum Wheels:** Momentum wheels are basically composed of an electrical motor attached to a flywheel. By rotating the mass of the flywheel, the spacecraft counter-rotates this rotation according to the conservation of angular momentum. Three-axis control of the satellite can be achieved with three different momentum wheels and typical accuracy can be as low as  $\pm 0.1^\circ$ . However, momentum wheels are not usual in CubeSat missions. Main reasons for this include relatively large power and mass requirements. Moving parts are also avoided to improve robustness.
- **Magnetorquers:** Electromagnetic actuators create a magnetic field that interacts with the geomagnetic field, thus generating a torque that rotates the spacecraft until the two fields align—exactly like a compass. Magnetorquers are a common choice for CubeSat projects since their mass, volume and power requirements are well suited for this kind of missions.

#### 6.2.1 Estimating Minimum Requirements for AntelSat Actuators

Equation (2.26) shows how the magnetic moment of a coil is related to the magnetic torque. Because of the vector product, for given vectors of magnetic dipole of a coil and geomagnetic field, the torque created by the interaction of these two is maximum when the vectors are perpendicular. In this case, the magnetic dipole magnitude of each coil can be expressed as

$$m_{coil} = \frac{T_{coil}}{B_E}$$

where  $B_E$  is the geomagnetic field.  $B_E$  can be approximated as  $2\mu_m/R_{orb}^3$  for a polar orbit at the equator.  $\mu_m = 7.96 \times 10^{15} \text{ Tm}^3$  is the total magnetic dipole strength of the Earth. Thus,

$$m_{coil} = \frac{T_{coil} R_{orb}^3}{2\mu_m}$$

## Chapter 6. AntelSat Hardware

where  $R_{orb} = 7.0 \times 10^6$  m.

The torque that the coils have to exert has to be greater than the worst case total disturbance torque estimated in Appendix A,  $T_{dist,tot} = 2.67 \times 10^{-7}$  Nm. It is noteworthy that it is most likely than in the real case the different disturbance torques cancel each other partially. For this reason, it is valid to expect a real total disturbance torque with a magnitude lower than the estimated value.

Nevertheless, as a design constraint for the coils these would have to exert a total torque  $T_{coil} > 2T_{dist,tot}$ . Hence, the magnetic dipole of each coil should be of a minimum value of

$$m_{coil,min} = 1.2 \times 10^{-2} \text{ Am}^2 \quad (6.1)$$

### 6.2.2 AntelSat Actuators Specifications

The actuators used for the AntelSat are embedded in +X, +Y and +Z solar panels. As explained in Section 6.1, the solar panels were acquired from GomSpace ApS and the coils are embedded in their multilayer PCB. The +Z side panel is a GomSpace's NanoPower P110UC series [60] whereas both the +X and +Y are both custom made. Table 6.1 summarizes the specifications for each coil.

Parameter	+X Side	+Y Side	+Z Side	Units
Track width	0.20	0.23	–	mm
Copper thickness	0.07	0.07	–	mm
Clearance	0.2	0.2	–	mm
Coil width	6	6	–	mm
Layers	10	10	–	–
Dimension X	80.4	70	–	mm
Dimension Y	198	198	–	mm
Windings per layer	15	15	–	–
Effective area	2.14	1.82	1.55	m <sup>2</sup>
Coils length	80	80	–	m
Coil resistance	95.9	81.5	135	Ω
Dipole moment	0.074	0.074	0.038	Am <sup>2</sup>

Table 6.1: Specifications for coils.

Dipole moments are given for a voltage of +3.3 V applied to the coils. From Eq. (2.24), it follows that the magnitude of the magnetic dipole of a magnetorquer is

$$m_{coil} = N_{coil} A_{coil} i_{coil}$$

## 6.2. Attitude Actuators

where  $A_{coil}$  is the area of the coil,  $N_{coil}$  is the number of windings of the coil and  $i_{coil} = V_{coil}/R_{coil}$  is the magnetorquer current, where  $V_{coil}, R_{coil}$  are the voltage and the resistance of the coil, respectively. In the case of the AntelSat, the coils will be connected to a maximum voltage of +5 V. Clearly, the dipole values are related by  $m_{coil,5V} = (5/3.3)m_{coil,3.3V}$ . Table 6.2 contains the dipole values for  $V_{coil} = +5$  V

Side	Dipole moment ( $\text{Am}^2$ )
+X	0.112
+Y	0.112
+Z	0.068

Table 6.2: Dipole values of different magnetorquers for  $V_{coil} = +5$  V.

The dipole moment values fulfill the requirements in Section 6.2.1:  $m_{coil,min} = 1.2 \times 10^{-2} \text{Am}^2$ .

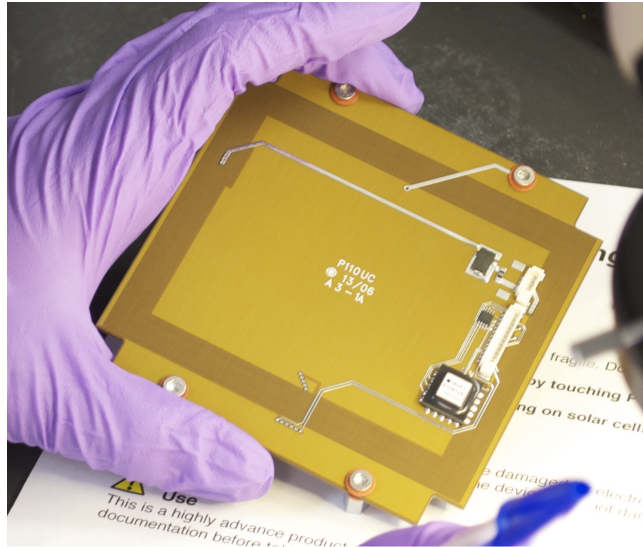


Figure 6.2: Picture of the +X side panel with magnetorquer.

Figures 6.2 and 6.3 show the inner face of the +X and +Y side panels, respectively. The embedded coils can be seen: they correspond to the thick darker rectangle close to the borders of the PCB.



Figure 6.3: Picture of the +Y side panel with magnetorquer.

## 6.3 Attitude Sensors

The following is a very brief summary of the most commonly used sensors in satellite missions and is presented as a reference for the reader. It is mainly based on [1,21].

**Reference Sensors** use celestial references such as the Sun, the Earth, or the stars to provide vector observations.

- **Star Trackers:** Star sensors represent the most common sensor for high-accuracy missions. On 3-axis stabilized satellites, trackers are used to track one or more stars to output 2- or 3-axis attitude information. Star sensors are susceptible to being blinded by celestial bodies such as the Sun, Moon or planets. These sensors are not usually taken into account for CubeSat missions since they are relatively expensive, heavy and with high power consumption. Also, the spacecraft must be stabilized before the trackers can be successfully used.
- **Horizon Sensors:** Horizon sensors detect the contrast between the cold of deep space and the heat of the Earth's atmosphere utilizing infrared sensors. Although they can get accuracies from 0.1 to 0.25 deg, costs can be prohibitive for CubeSat missions. Horizon sensors with coarser accuracies present lower costs, but in this case they are not as widely used as Sun sensors.
- **Sun Sensors:** Sun sensors are visible-light detectors which measure one or two angles between their mounting base and incident sunlight. They exploit the fact that the Sun is a well defined reference. However, Sun sensors require a clear field of view: information from Sun sensors is not available during eclipses. This poses a problem since most low-Earth orbits include

## 6.3. Attitude Sensors

eclipse periods and attitude determination systems must provide other ways to estimate the attitude during those periods. Coarse accuracy Sun sensors are a widely used choice for attitude determination in CubeSat missions.

- **Magnetometers:** Most spacecrafts with low-Earth orbits, and CubeSats in particular, carry a magnetometer as part of their attitude determination system. A 3-axis magnetometer measures the direction and intensity of the local geomagnetic field. When this measure is compared to Earth's known field, it is possible to establish the spacecraft attitude. Benefits of magnetometer are low power consumption, low cost, small size and weight. Also, their information is always available. However, they are not as accurate as star of horizon sensors: Earth's field can shift with time and is not known precisely. On top of that, magnetic fields created by onboard electronics affect measurements. In particular, magnetorquers must be turned off while the magnetometer is sampled to avoid corrupt measurements.
- **GPS receivers:** Global Positioning System (GPS) receivers are becoming more common on spacecraft for a very precise orbit determination and timing. Nevertheless, the power consumption for a CubeSat is relatively high and receivers are expensive. In the case of the AntelSat, as a project decision it was decided not to include a GPS receiver considering their high power requirements and in order to keep the general complexity of the system as low as possible.

**Inertial Sensors** measure magnitudes relative to an inertial frame, but without any knowledge of an external, absolute reference.

- **Gyroscopes:** Gyroscopes measure the speed or angle of rotation from an initial reference. Traditionally, inertial reference units are mounted in multi axis gimbals assemblies and are mechanically complex, heavy and with large power requirements. Off-the-shelf, commercially available gyros are based on different concepts—such as piezoelectric quartz gyros. These advances have resulted in a decrease in size, weight, cost and power requirements, whereas accuracies and ease of integration have increased. Gyroscopes are a usual choice in CubeSat missions.

The sensor market evolves swiftly so the general characteristics of sensors exposed above are prone to change in the near future.

The selected sensors for the AntelSat are six Sun sensors, a 3-axis magnetometer and three 1-axis gyroscope. Table 6.3 shows a summary of the sensors and their models. Section 6.3.1 presents these sensors more in detail.

### 6.3.1 AntelSat Sensors Specifications

- **Sun Sensors: SLCD-61N8**

Sensor	Manufacturer	Model	Measurement
Gyro	Analog Devices	ADIS16251	Angular velocity
Magnetometer	PNI Corporation	MicroMag3	B-field
Photodiode	Silonex	SLCD-61N8	Sun vector

Table 6.3: AntelSat ADCS sensors

The Sun sensors in the AntelSat consist of a photodiode connected to the analog-to-digital converter (ADC) of the microprocessor with an amplification stage connected in between these two. The photodiode used model is the one included in the solar panels, SLCD-61N8 from Silonex Inc. [61]. Table 6.4 summarizes its main specifications.

Whenever the spacecraft is illuminated by the Sun, only three sides are exposed to direct sunlight. Then, the three sides with highest current values are utilized to compute the Sun vector.

Property		Units
Type	Solderable planar photodiode	
Interface	Analog	
Dimensions	$3.4 \times 1.3 \times 0.4$	4
Short circuit current	170	$\mu\text{A}$
Open circuit voltage	0.40	V
Half angle	60	$^{\circ}$
Operating temperature	-40 to 125	$^{\circ}\text{C}$

Table 6.4: Specifications for the SLCD-61N8 photodiode.

- **Gyroscope: ADIS16251**

The solar panels for the +X, +Y and +Z faces also include a 1-axis gyroscope, the ADIS16251 from Analog Devices [62]. Their properties are shown in Table 6.5. They also appear in Figs. 6.2 and 6.3 as the chips with the largest packaging.

Most of the commercially available gyroscopes are intended for gaming or robotics applications, with measurement ranges of at least  $\pm 250^{\circ}$ , rendering them unsuitable for missions like AntelSat. However, the ADIS16251 is used in applications such as instrumentation control or avionics instrumentation.

### 6.3. Attitude Sensors

This fact is reflected on its three different scale range:  $\pm 20^\circ$ ,  $\pm 40^\circ$ ,  $\pm 80^\circ$  and they make this gyroscope an acceptable choice for AntelSat.

The ADIS16251 operates on the principle of a resonator gyroscope and measures the angular rate directly using the Coriolis effect. Hence, no drift due to integration of acceleration exists.

The integration with the microprocessor is via a 4-wire, industry standard serial peripheral interface (SPI). The rate measurement are filtered with an internal Barlett Window FIR filter before they are output. The maximum throughput rate for the gyro is 256 samples per second. Other useful features include an on-chip temperature sensor, auto zero for bias drift calibration and embedded integration for short term angle estimates.

Property		Units
Type	Angular rate sensor	
Interface	SPI	
Dimensions	$11 \times 11 \times 5.5$	$\text{mm}^3$
Scale range	$\pm 20, \pm 40, \pm 80$	$^\circ/\text{sec}$
Output resolution	0.01832, 0.00916, 0.00458	$^\circ/\text{sec}/\text{LSB}$
Nonlinearity	0.1	% of full scale
Operating voltage	5	V
Power supply current	18	mA, normal mode
Operating temperature	-40 to 85	$^\circ\text{C}$
Shock tolerance	2000	g

Table 6.5: Specifications for the ADIS16251 gyroscope.

- **Magnetometer: MicroMag3**

The MicroMag is an integrated 3-axis magnetic field sensing module from PNI Sensor Corporation [63]. Table 6.6 summarizes the properties of the sensor. As discussed in Section 6.1, this sensor model selection is directly inherited from the precedent projects in the AntelSat development project. Figure 6.4 displays the magnetometer.

The magnetometer consists of three 1-axis PNI's patented magneto-inductive sensors combined with a measurement circuit, also in charge of implementing the interface with the microprocessor—a 4-wire SPI interface.

Property	Units	
Type	Magnetic field sensor	
Interface	SPI	
Dimensions	$25.4 \times 25.4 \times 19$	$\text{mm}^3$
Scale range	$\pm 1100 \mu\text{T}$	$^\circ/\text{sec}$
Resolution	0.015	$\mu\text{T}$
Linearity	0.6	%
Operating voltage	3	V
Power supply current	0.4	mA, normal mode
Operating temperature	-20 to 70	$^\circ\text{C}$

Table 6.6: Specifications for the MicroMag 3 magnetometer.

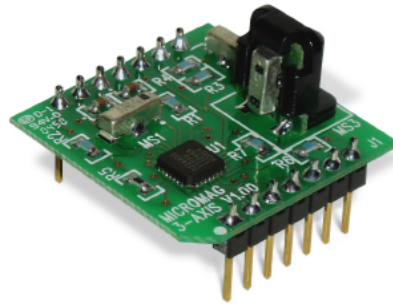


Figure 6.4: MicroMag 3 magnetometer [63]

## 6.4 Design of the Hardware

Each subsystem in the AntelSat project is conceived as an independent module and for this reason every one of them possess its own microcontroller. The ADCS board is based on an 16-bits MSP430 microcontroller from Texas Instruments, a MSP430F5438A [64]. The MSP430 is a low power processor running at 8 MHz. Among many peripherals included, the MSP430 comes with several SPI and I2C communication interfaces, different configurable clock sources, 16-bits timers and PWM outputs. Since this microcontroller is computing power-limited, the ADCS also has a 32-bits ARM Cortex-M4F from STMicroelectronics, a STM32F303CC [65]. The ARM is in charge of performing more demanding calculations as it runs at 64 MHz and has a hardware floating-point unit capable of executing single-cycle multiplications and divisions. Both microprocessors are programmed and debugged via the JTAG interface. Figure 6.5 shows a diagram of the ADCS subsystem with its CPUs and other components.

## 6.4. Design of the Hardware

Communications of the ADCS with the rest of the subsystems are implemented in the MSP430 via I2C. The communications interface between the two CPUs is SPI. The physical and electrical interconnection among the rest of the subsystems in the satellite is implemented using a PC104/plus connector type.

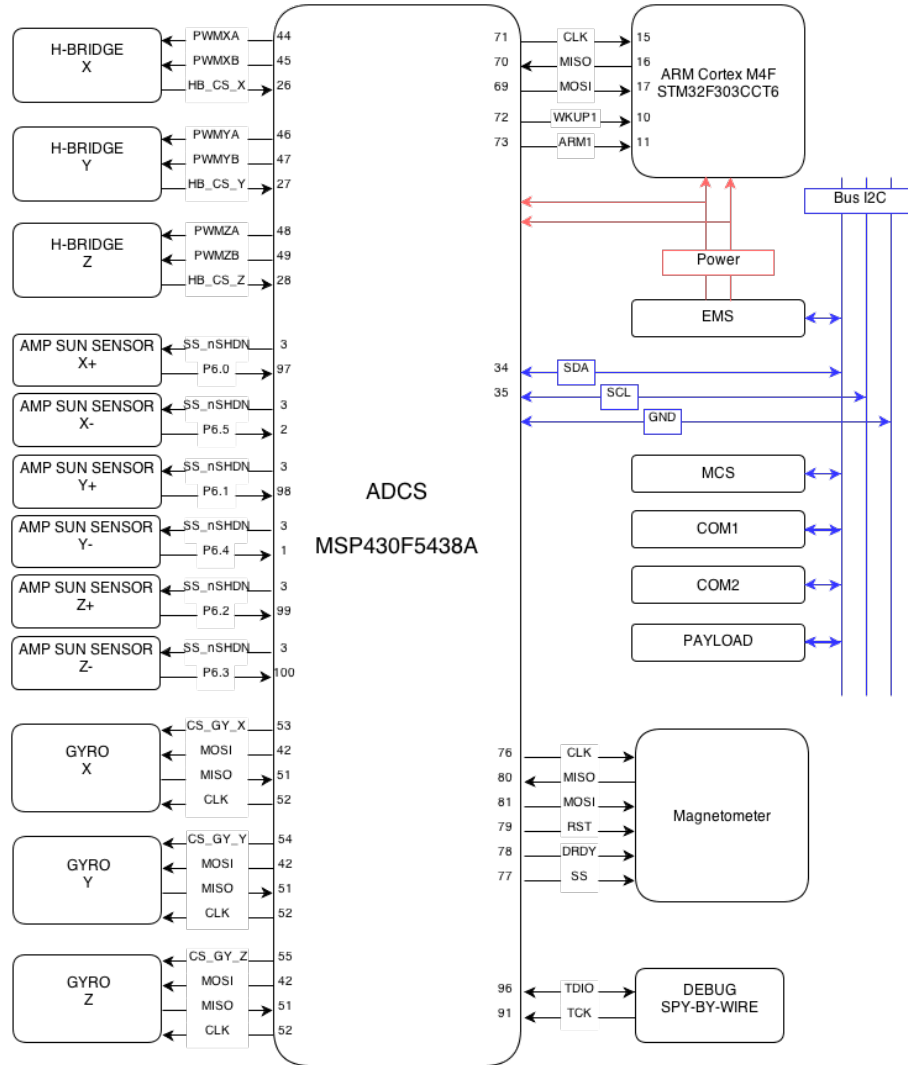


Figure 6.5: Block diagram of the hardware of the ADCS.

The ADCS board receives +5 V as power input. Then, the power line is separated in three by using three different linear voltage regulators:

- **Circuit A:** for magnetorquers and gyroscopes. Voltage is +5 V. Controlled by the MSP430.
- **Circuit B:** for Sun sensors and the magnetometer. Voltage is +3.3 V. Controlled by the MSP430.
- **Circuit C:** for the CPUs. Voltage is +3.3 V. Always on.

## Chapter 6. AntelSat Hardware

Separating power circuits using linear regulators helps stabilizing input voltages and reduces noise levels.

Both the attitude actuators and sensors are located outside the ADCS board and all of them are controlled by the MSP430 CPU. The incoming analog signal from the Sun sensors is first amplified and then read by the ADC of the MSP430. The interface of the magnetometer is SPI, as well as for the gyroscopes. The coils of the magnetorquers are commanded with pulse-width-modulation (PWM) outputs of the MSP430.

Electrically, a magnetorquer can be seen as an inductive load similar to a DC motor. The digital pins of the MSP430 are not capable of driving the current required by the coils and voltage peaks derived from switching inductive loads can damage the CPU's outputs. Hence, driving the coils requires some type of interface electronics and for this reason a H-Bridge is used. The output of the H-Bridges is filtered with a simple RC circuit to drive the coils with a voltage signal as close to DC voltage as possible and to mitigate ripples. The PWM frequency is 2 kHz and the cut frequency of the RC filter is less than a tenth of the former. A series resistance has also been added to address the effects of having magnetorquers with different specifications.

Sensors and actuators are placed throughout the spacecraft in the interest of minimizing interference in measurements. In close relation to this, magnetic actuation indeed affects magnetometer reading which may mislead the attitude determination. As physical separation of magnetometer and magnetorquers is not enough considering the small volume involved, magnetic sensing and actuation are separated in time. As the controller cycle is 1000 ms, it is split into 800 ms dedicated for actuation and the remaining 200 ms are reserved for metering.

Figure 6.6 shows the a finished ADCS board.

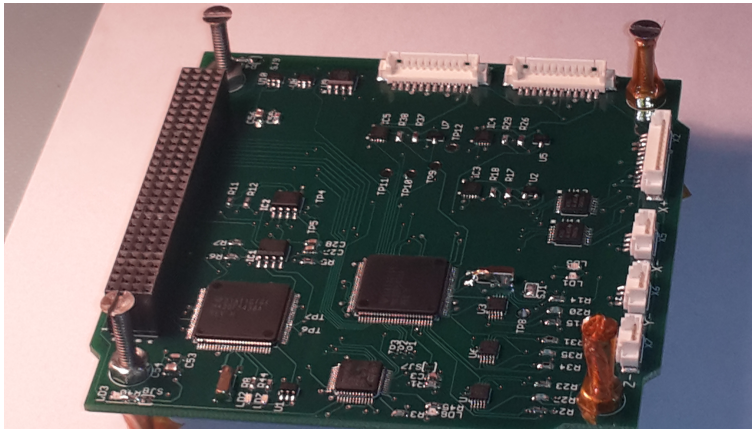


Figure 6.6: Finished flight version of the ADCS board.

Software running on both CPUs was developed together with the help of the software development group. The MSP430 software, in charge of implementing the communication with the rest of the subsystems and the ARM, as well as controlling actuators and sensors, is based on a real time operating system designed in house,

see [66]. The attitude control and determination algorithms were ported to the ARM, see [56].

As the space presents a very harsh environment, requirements for hardware become more stringent. Some aspects must be taken into account when designing hardware for space:

- Temperature varies in large ranges in short time terms. Temperature differences in an orbit could get up to  $20 - 40^{\circ}\text{C}$  in the inside of a satellite.
- Radiation exposure is very high. Higher radiation doses cause electronic components to degrade faster. Radiation can also cause random bit flips in memory.
- Vacuum causes some materials to outgas.
- During launch, the hardware experiences violent vibrations and shaking.

To address these conditions, the electronic components were selected following the guidelines provided in [67]. The document instructs on how to consider components with derated specifications, i.e. to consider the components with reduced power ratings. On the other hand, outgassing of materials is avoided by placing the satellite in a thermo-vacuum chamber for several hours some weeks before launch. The gasses and moisture in the components of the satellite are then released. An urethane conformal coating is applied on the PCBs since it provides a very good electrical insulation with low outgassing.

The ADCS board consists of a four layer PCB with surface-mount components, with most passive components of 0603 and 0402 sizes. The design of both the prototype version and flight version was carried out by the author of this thesis, while all the boards were soldered by hand by Ignacio De León, Gonzalo Gutiérrez, Gonzalo Sotta, and the author. Appendix B includes some relevant pictures of the ADCS and AntelSat hardware.

## 6.5 Summary

This chapter has introduced the design and development of the hardware of the AntelSat ADCS, in a succinct manner. In particular, the choice of attitude sensors and actuators has been presented. A summary of the most common choices for attitude sensors and actuators in satellites has also been given.

The choice of sensors includes six Sun sensors composed of the SLCD-61N8 photodiode from Silonex, three 1-axis ADIS16251 gyroscopes from Analog Devices and one 3-axis Micromag 3 magnetometer from PNI Corporation. The actuators are three electromagnetic coils, one per geometrical axis of the body of the satellite. The coils are embedded in the solar panels PCBs. Overall cost is not significant, as is usual in CubeSat missions, at the expense of accuracy.

This page has been intentionally left blank.

# Chapter 7

## Conclusions and Recommendations

The aim of this thesis has been to design and implement an effective attitude determination and control system for the AntelSat nanosatellite. This chapter summarizes the conclusions for each previous chapter and gives recommendations for future work.

### 7.1 Conclusions

To begin with, the modelling of the satellite kinematics and dynamics was presented in Chapter 2, along with a description of the Keplerian orbital elements and the environment in a low-Earth orbit. The coordinate systems used in the thesis were introduced, as well as the chosen attitude parametrization, quaternions, which do not suffer from singularities. Moreover, a linearized model of the satellite was offered.

The two different attitude determination methods implemented for AntelSat, the optimal quaternion estimation method and the unscented Kalman filter, were described in Chapter 3. Advantages of the former include simplicity, the need of only two types of sensors and relatively low computational times. On the other hand, advantages of the latter include a lower steady-state mean error and valid outputs even when the satellite is in eclipse. Simulations displayed the performance of both algorithms using the low-cost off-the-shelf sensor setup chosen for AntelSat. QuEst presented a mean error of  $4.5^\circ$  outside the eclipse whereas UKF got a steady-state mean error of  $1.7^\circ$  after the convergence phase. It was shown that reducing substeps of the Runge Kutta implementation sensibly decreased overall UKF computation times without a significant loss of accuracy.

The B-dot detumbling controller was described in Chapter 4, along with the controller implementation and a Lyapunov stability analysis. The controller only utilizes measurements from the magnetometer as inputs. Simulations showed that the controller is able to detumble the satellite from an initial angular rate of about  $50^\circ/\text{s}$  to  $0.1^\circ/\text{s}$  in less than two and a half orbits.

Also in Chapter 4, the problem of attitude control of a nadir pointing spacecraft the nominal pointing controller was presented: a constant gain LQR controller.

## Chapter 7. Conclusions and Recommendations

The performance of the linear controller was assessed in a nonlinear simulation environment, which included disturbance torques. Simulations showed that it is feasible to achieve 3-axis control based on magnetic actuation for the AntelSat. The simulations also showed that the algorithm converged even when the initial conditions are largely distanced from the equilibrium.

A complete simulation environment including AntelSat dynamics and disturbance torques has been implemented in Simulink, based on the works mentioned in Chapter 5. The simulation environment provided a valuable tool for developing the attitude determination and control algorithms and also to evaluate their performance in realistic scenarios.

As reviewed in Chapter 6, construction of both prototype and flight version hardware was successfully implemented. The construction included design and fabrication of the electronic boards and their electrical and functional testing.

### 7.2 Recommendations for Future Work

A valuable tool in these type of projects are closed-loop simulations involving the environment simulator and the onboard hardware (Hardware-in-the-Loop simulations, or HIL). Validation of the determination and control algorithms developed in Simulink is a time demanding task. On top of that, once these algorithms are implemented and ported to the onboard hardware, further testing should be carried out to ensure these implementations perform similarly to the Simulink versions. The latter can be achieved in a straightforward manner by using HIL tools. Although some work was done, a final version of a HIL platform could not be finished due to time constraints.

Overall power consumption for attitude control could be reduced by adding a passive actuator, such as a permanent magnet. Although permanent magnets are not able to decrease rotational energy in a tumbling satellite, they can provide 2-axis stabilization after the satellite is detumbled.

It would be interesting to consider adding some modifications to the UKF attitude estimator in order to achieve the following improvements. The robustness of the UKF against bias in sensors can be increased by adding these bias in the state vector of the filter, as done in [13]. Also, an UKF approach without the need of rate sensors appears attractive since rate sensors might not be always available. This approach could be implemented using the geomagnetic field and the geomagnetic field derivative, such as in [68].

# Appendix A

## Worst case disturbance torques

Environment modelling and analytical expressions for disturbance torques in particular are presented in detail in Section 2.4. However, they are presented again in this section, in a slightly modified way, with the aim of finding a worst case scenario for the total disturbance torque value  $T_{dist,tot}$ . As well, conservative values for parameters are used and these sometimes differ from the ones selected in Section 2.4. This approach follows the guidelines presented in [1].

Despite the fact that the magnitude of the resultant disturbance torque here calculated is the sum of every individual disturbance, it is very unlikely that all the disturbances point in the same direction. Hence, in the real case, the resultant torque is of a lower magnitude than the calculated value most of the time. However, the worst case disturbance calculation is valid and useful for other uses, such as estimating the required torque that the actuators should exert.

### A.1 Aerodynamic Drag

The aerodynamic drag value can be modelled as

$$\|\mathbf{T}_{aero}\| = \frac{1}{2}C_a\rho_a A_p \|\mathbf{v}_{sat}\|^2 (C_{CoP} - C_{CoM}) \quad (\text{A.1})$$

where  $C_a$  is the aerodynamic drag coefficient,  $\rho_a$  is the atmosphere density,  $\mathbf{v}_{sat}$  is the translational velocity vector of the satellite,  $A_p$  is the projected area of the satellite and  $C_{CoP} - C_{CoM}$  is the distance between the center of pressure and the center of mass. Since AntelSat complies with the CubeSat standard, the latter parameter has a value of up to 0.02 m, and this value will be used in for the rest of this section.

For computing the worst case scenario, an orbit height of 600 km is considered and the values  $C_a = 2.2$ ,  $\rho_a = 1 \times 10^{-12} \text{ kg/m}^3$  and  $\mathbf{v}_{sat} = 7558 \text{ m/s}$  are used. For the projected area, the case in which one of the diagonals of the satellite coincides with the direction of the translational velocity is employed. For this case,  $A_p = \frac{5}{\sqrt{6}}a^2$ ;  $a = 0.1 \text{ m}$ .

The selected values yield a torque value of

$$\|\mathbf{T}_{aero}\| = 2.6 \times 10^{-7} \text{ Nm}$$

## Appendix A. Worst case disturbance torques

### A.2 Solar Radiation Pressure

The disturbance torque due to solar radiation can be modelled as

$$\|\mathbf{T}_{sr}\| = \frac{F_{solar}}{c} A_p C_k \cos i (C_{CoP} - C_{CoM})$$

where  $F_{solar} = 1363 \text{ W/m}^2$  is the solar constant,  $c = 3.0 \times 10^8 \text{ m/s}$  is the speed of light,  $C_k = 1.7$  is a coefficient used to specify the outer material of the satellite and  $i$  is the angle of incidence of the solar radiation on the surface of the satellite. As aforementioned,  $C_{CoP} - C_{CoM} = 0.02 \text{ m}$ .

For worst case scenario,  $i = 0^\circ$  and  $A_p = 2a^2$ ;  $a = 0.1 \text{ m}$  are considered and thus it yields

$$\|\mathbf{T}_{sr}\| = 3.1 \times 10^{-9} \text{ Nm}$$

### A.3 Gravity-gradient

A simplified version of the torque due to the gravity-gradient can be expressed as

$$\|\mathbf{T}_{gg}\| = \frac{3\mu_G}{2R_{orb}^3} |I_z - I_y| \sin 2\theta$$

where  $\mu_G = 3.986 \times 10^{14} \text{ m}^3/\text{s}^2$  is the Earth's gravitational constant,  $\theta$  is the maximum deviation of the z-axis from the local vertical,  $|I_z - I_y| = 0.002524 \text{ kg/m}^2$  is the maximum difference between the inertia moments of the satellite and  $R_{orb}$  is the distance from the center of the Earth to the satellite.

For worst case scenario,  $\theta = 45^\circ$ . Lastly, setting  $R_{orb} = 7.0 \times 10^6 \text{ m}$ , yields

$$\|\mathbf{T}_{gg}\| = 3.9 \times 10^{-9} \text{ Nm}$$

### A.4 Total Torque

Type	Value (Nm)
Aerodynamic drag	$2.6 \times 10^{-7} \text{ Nm}$
Solar pressure	$3.1 \times 10^{-9} \text{ Nm}$
Gravity-gradient	$3.9 \times 10^{-9} \text{ Nm}$
<b>TOTAL</b>	<b><math>2.67 \times 10^{-7} \text{ Nm}</math></b>

Table A.1: Total magnitude of worst case torque.

It follows that the worst case disturbance torque is  $T_{dist,tot} = 2.67 \times 10^{-7} \text{ Nm}$ .

## Appendix B

### AntelSat and ADCS Pictures

This chapter includes some relevant pictures that portray different stages of the design and construction of the AntelSat.

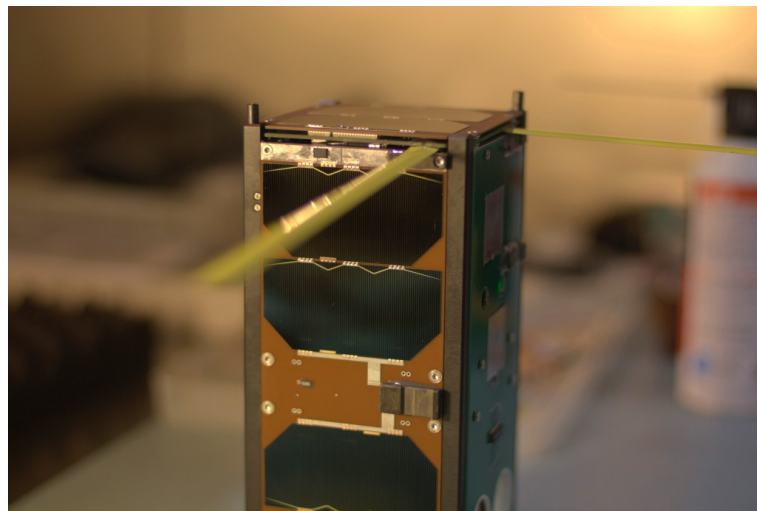


Figure B.1: Complete AntelSat with antennas deployed.

## Appendix B. AntelSat and ADCS Pictures

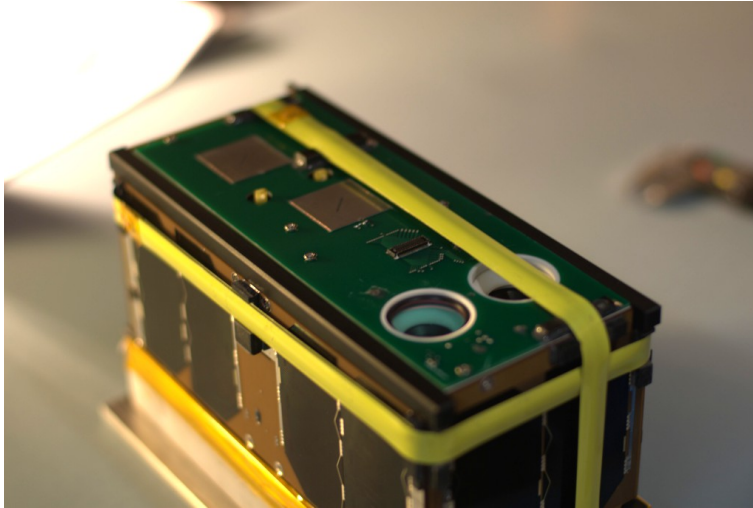


Figure B.2: Complete AntelSat with antennas in a stowed position.

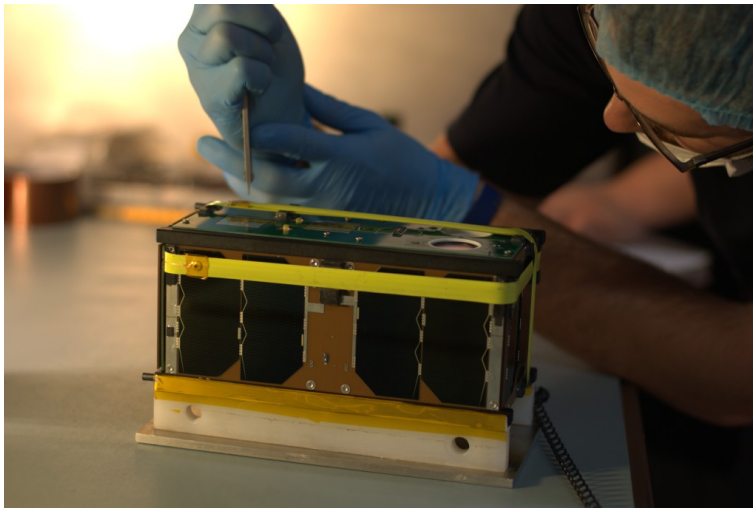


Figure B.3: Dimensions check after the thermo-vacuum test.

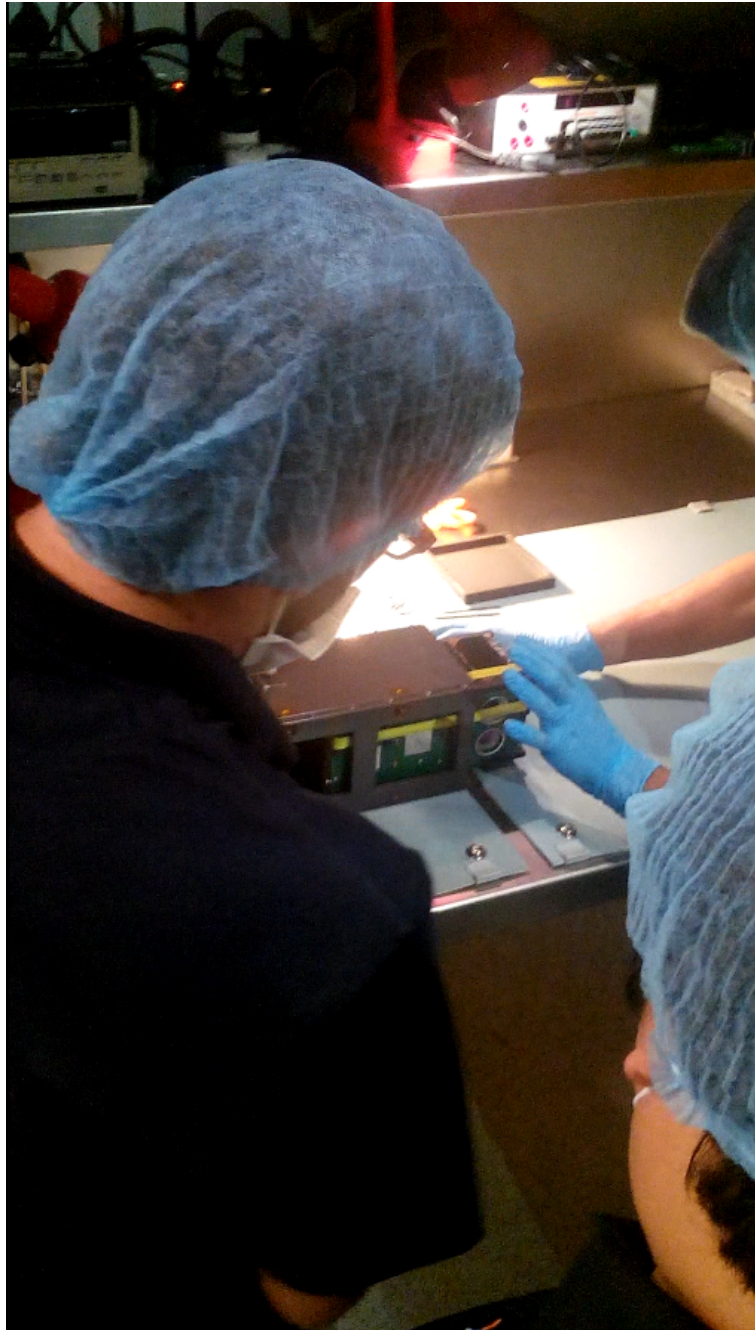


Figure B.4: Getting AntelSat inside a storage P-POD.

Appendix B. AntelSat and ADCS Pictures

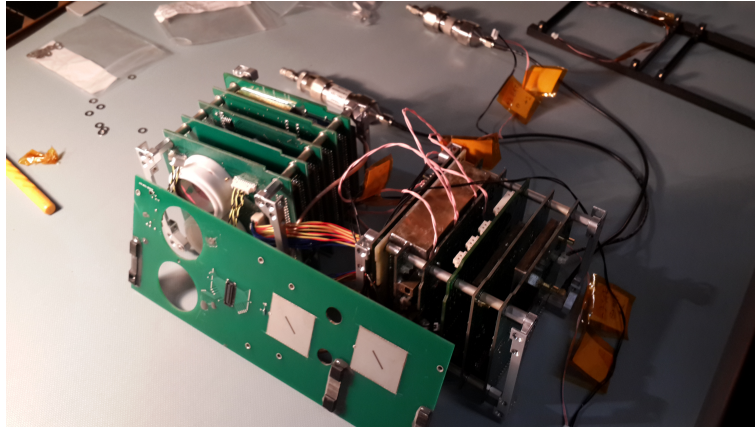


Figure B.5: Interconnection of internal PCBs.

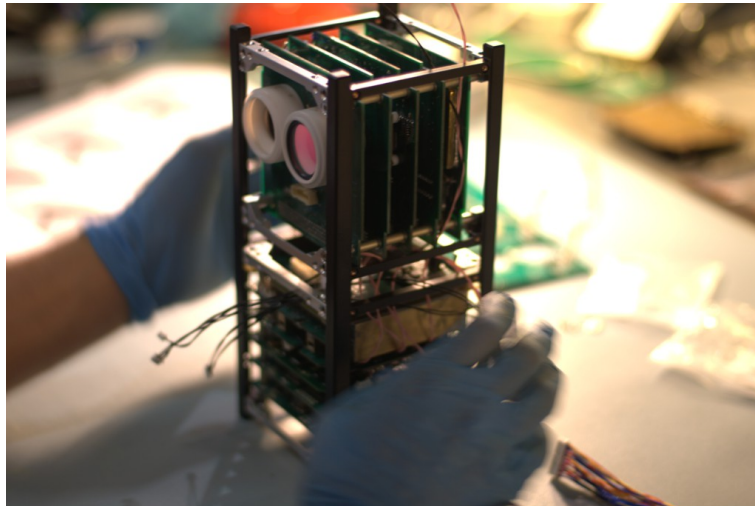


Figure B.6: AntelSat in the integration phase.

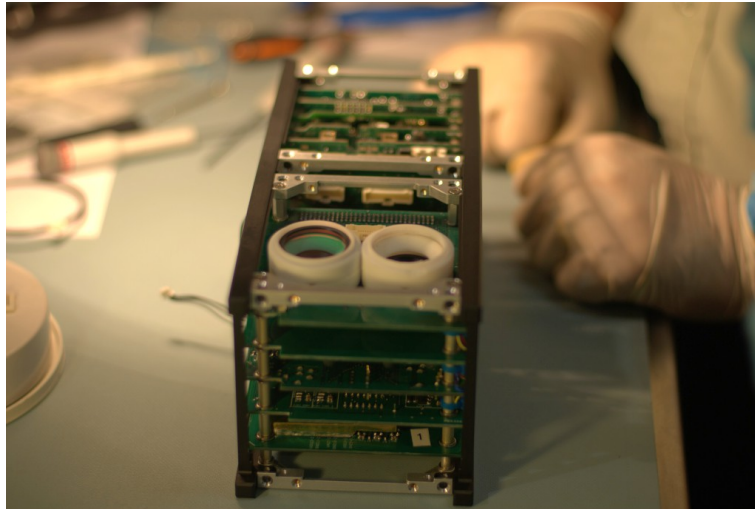


Figure B.7: Assembly of the satellite.

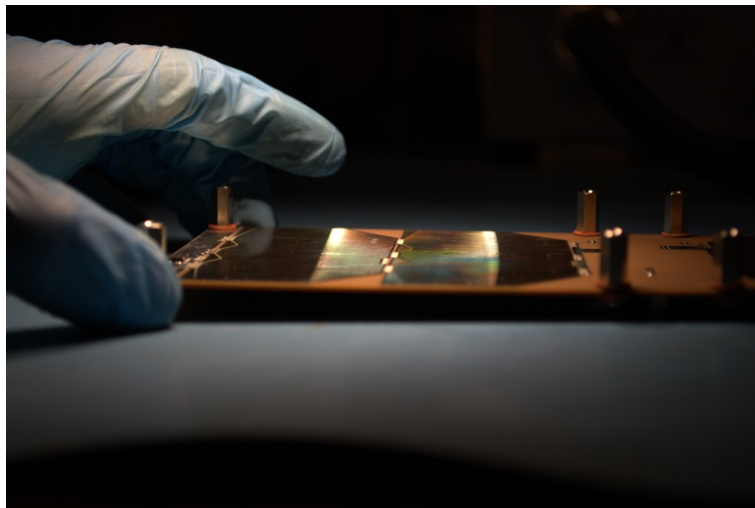


Figure B.8: Handling of one of the solar panels in the lab.



Figure B.9: Photodiodes testing.

Appendix B. AntelSat and ADCS Pictures

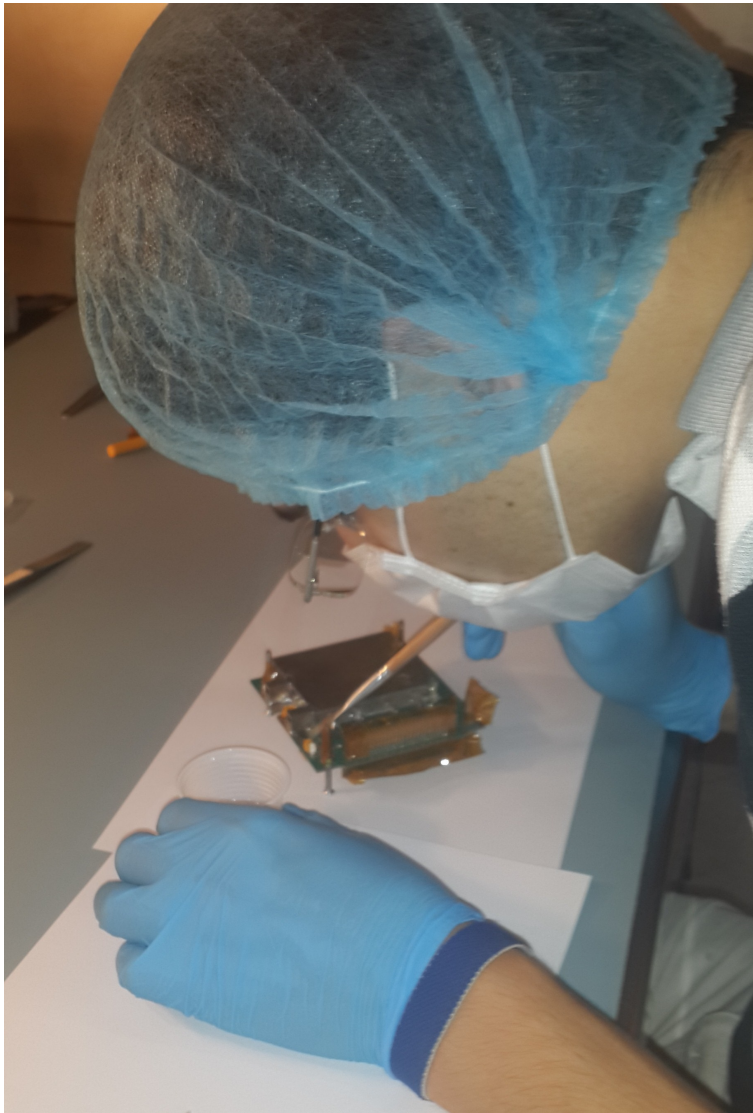


Figure B.10: Applying urethane conformal coating on the PCBs.

# Appendix C

## ADCS After Launch

This appendix briefly comments on the events after the release of the AntelSat into space.

As treated in Section 1.4, AntelSat was put into orbit on June 19th 2014. One-way communication was achieved on the same day, while uplink was finally established around fifteen days later. For reasons related to the operation, it was not possible to initiate ADCS until some months later.

The main objective when the ADCS was eventually turned on was to decrease the angular velocity of the satellite. From outputs of the attitude estimation algorithm, it was possible to determine the initial angular velocity magnitude at about  $1.5^\circ/\text{s}$ . Later, the detumbling controller (see Section 4.1) was triggered. Due to a precautionary restriction, the algorithm was only run in short time periods of ten to fifteen minutes. This restriction was inspired by bad experiences of various other missions (see for example [13, 69]) in which the application of the detumbling algorithm ended up increasing the angular rate and not the opposite. The aim of the precaution was to mitigate the outcome in case that some error related to the detumbling algorithm occurred. This design restriction proved fruitful since, due to misconfiguration of some ADCS parameters, the AntelSat increased its angular velocity, although only some degrees per second. Later inspection revealed that the magnitude of the total angular velocity was close to  $12^\circ/\text{s}$  at this stage. Reconfiguration of the mentioned ADCS parameters led to the eventual detumble of the AntelSat to a final angular velocity of magnitude close to  $0.5^\circ/\text{s}$ . At this point, the performance of the onboard magnetometer (described in Section 6.3.1) began to degrade notoriously since measurements of each axis included offsets of unacceptable value. Lastly, it was decided that the magnetometer could not be trusted any further, rendering the ADCS unusable.

Figures C.1 to C.3 illustrate the information above. Figure C.1 displays the module of the angular velocity estimations. These estimations are the outputs of the attitude determination algorithm included in ADCS logs received from the AntelSat. The x-axis shows the dates corresponding to the outputs. Figure C.2 displays the same information but this time the estimation results are presented consecutively and the x-axis shows the corresponding sample number. Finally, Fig. C.3 demonstrates the behaviour of the magnetometer. Blue, red, and green

## Appendix C. ADCS After Launch

lines correspond to the x, y, and z axis, respectively. The readings are presented in a consecutive manner, similar to Fig. C.2, and the x-axis shows the corresponding sample number. It can be seen that after sample number 400, the measurements corresponding to each axis began spreading, and after sample number 500 this separation increased in notoriety. It can also be seen that not only the offsets changed along sample numbers, but also the corresponding gains for each axis.

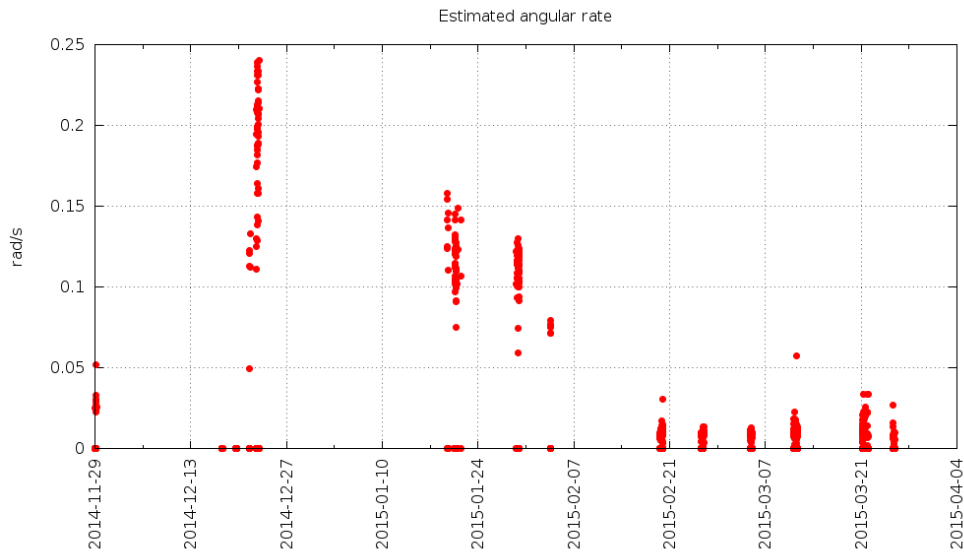


Figure C.1: Estimated angular rate magnitude.

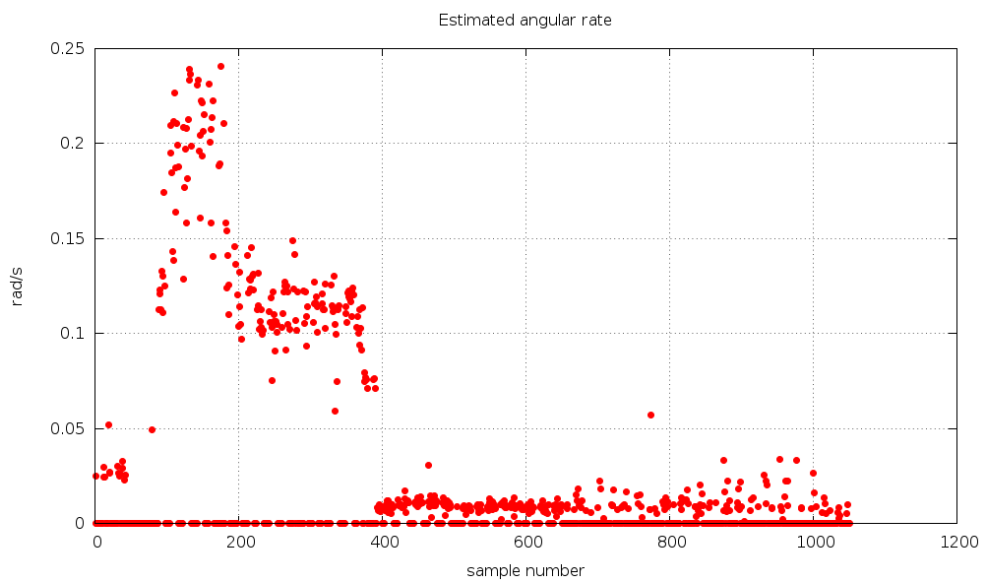


Figure C.2: Estimated angular rate magnitude vs. sample number.

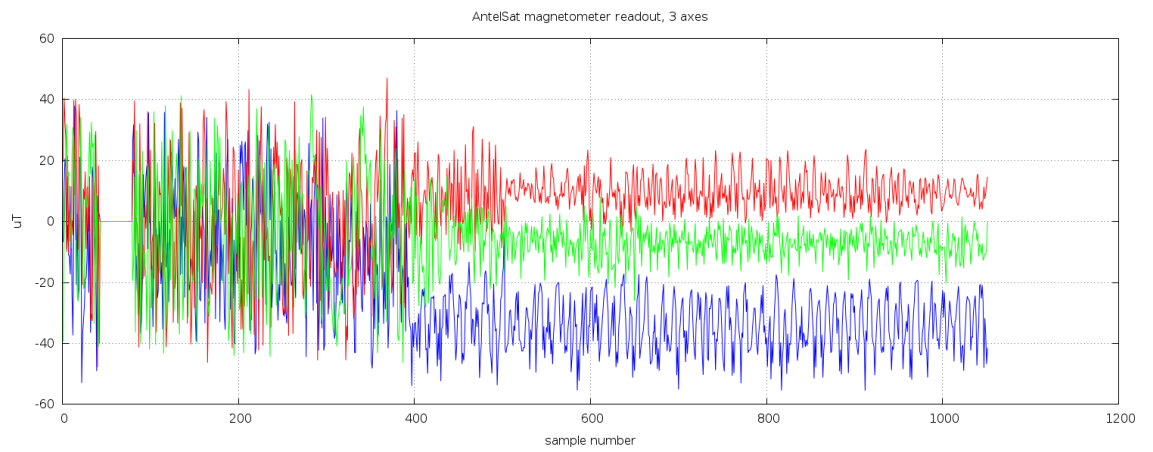


Figure C.3: Magnetometer readings vs. sample number.

This page has been intentionally left blank.

# Bibliography

- [1] W.J. Larson and J.R. Wertz. Space mission analysis and design. Technical report, Torrance, CA (United States); Microcosm, Inc., 1992.
- [2] Hank Heidt, Jordi Puig-Suari, Augustus Moore, Shinichi Nakasuka, and Robert Twiggs. CubeSat: A new generation of picosatellite for education and industry low-cost space experimentation. 2000.
- [3] T. Graversen, M.K. Frederiksen, and S.V. Vedstesen. *Attitude control system for AAU CubeSat*. Aalborg University. Department of Control Engineering, 2002.
- [4] R. Miyagusuku, K.R. Arias, and E.R. Villota. Hybrid magnetic attitude control system under CubeSat standards. In *Aerospace Conference, 2012 IEEE*, pages 1–9, march 2012.
- [5] D.V. Guerrant. Design and analysis of fully magnetic control for picosatellite stabilization. Master's thesis, California Polytechnic State University, 2005.
- [6] Jens Gießelmann. Development of an active magnetic attitude determination and control system for picosatellites on highly inclined circular low earth orbits. *Master of Engineering RMIT University*, pages 1–11, 2006.
- [7] European Space Agency. Envisat. "<https://earth.esa.int/web/guest/missions/esa-operational-eo-missions/envisat>", 2015. [Online; accessed 06-May-2015].
- [8] Juan Pechiar. Lai globosat 04. <http://iie.fing.edu.uy/investigacion/grupos/lai/gso4.html>, 2010. [Online; accessed 28-July-2013].
- [9] S De Jong, GT Aalbers, and J Bouwmeester. Improved command and data handling system for the delfi-n3xt nanosatellite. In *Proceedings of the 59th International Astronautical Congress, Glasgow, Scotland*, 2008.
- [10] Sajid Ghuffar. Design and implementation of attitude determination algorithm for the cubesat UWE-3. *Luleå University of Technology, Kiruna, Sweden*, 2010.

## Bibliography

- [11] Muriel Noca, Fabien Jordan, Nicolas Steiner, Ted Choueiri, Florian George, Guillaume Roethlisberger, Noémy Scheidegger, Hervé Peter-Contesse, Maurice Borgeaud, Renato Krpoun, et al. Lessons learned from the first Swiss pico-satellite: SwissCube. 2009.
- [12] Pablo Aguirre and Conrado Rossi. Ultra-low power temperature sensor. In *Memorias del 5º Congreso Iberoamericano de Sensores. Ibersensor. Montevideo, Uruguay*, sep 2006.
- [13] Kasper Fuglsang Jensen and Kasper Vinther. Attitude determination and control system for AAUSAT3. Master’s thesis, Aalborg University, 2010.
- [14] ISC Kosmotras. Dnepr space launch system user’s guide, Nov 2001.
- [15] NASA SpaceFlight. Russian dnepr rocket lofts record haul of 37 satellites. <http://www.nasaspaceflight.com/2014/06/russian-dnepr-rocket-record-launch-37-satellites/>, June 2014.
- [16] Bong Wie. *Space vehicle dynamics and control*. Aiaa, 1998.
- [17] North American Aerospace Defense Command. About NORAD. <http://www.norad.mil/AboutNORAD.aspx>. Accessed: 2015-03-23.
- [18] T Kelso. NORAD two-line element set format. <http://www.celestrak.com/NORAD/documentation/tle-fmt.asp>. Accessed: 2015-03-24.
- [19] Raymond A Serway, Robert J Beichner, and John W Jewett. Physics for scientists and engineers with modern physics. 2000.
- [20] Sanyam S Mulay, Jaideep Joshi, Yashovardhan S Chati, Vaibhav V Unhelkar, Saptarshi Bandyopadhyay, Shashank Tamaskar, Mallesh Bommanahal, Chaitanya Talnikar, Avnish Kumar, and Hari B Hablani. Attitude determination and control of Pratham, Indian Institute of Technology Bombay’s first student satellite. *Advances in the Astronautical Sciences*, 145:1509–1528, 2012.
- [21] Thomas Bak, Rafal Wisniewski, and Mogens Blanke. Autonomous attitude determination and control system for the ørsted satellite. In *Aerospace Applications Conference, 1996. Proceedings., 1996 IEEE*, volume 2, pages 173–186. IEEE, 1996.
- [22] Renato Miyagusuku, Klebes R Arias, and ER Villota. Hybrid magnetic attitude control system under cubesat standards. In *Aerospace Conference, 2012 IEEE*, pages 1–9. IEEE, 2012.
- [23] J.R. Wertz. *Spacecraft attitude determination and control*, volume 73. Kluwer Academic Pub, 1978.
- [24] J. J. Butler, B. C. Johnson, J. P. Rice, E. L. Shirley, and R. A. Barnes. Sources of differences in on-orbital total solar irradiance measurements and description of a proposed laboratory intercomparison. In *Journal of Research*

- of the National Institute of Standards and Technology*, volume 113, pages 187–203, 2008.
- [25] National Geophysical Data Center. Geomagnetism-national geophysical data center. "<http://www.ngdc.noaa.gov/geomag/>", 2014. [Online; accessed 26-December-2014].
- [26] International Association of Geomagnetism and Aeronomy. International association of geomagnetism and aeronomy - division V-MOD geomagnetic field modeling. "<http://www.ngdc.noaa.gov/IAGA/vmod/home.html>", 2014. [Online; accessed 26-December-2014].
- [27] Mahmut Reyhanoglu and Jaime Rubio Hervas. Three-axis magnetic attitude control algorithms for small satellites. In *Recent Advances in Space Technologies (RAST), 2011 5th International Conference on*, pages 897–902. IEEE, 2011.
- [28] R. Wisniewski. *Satellite attitude control using only electromagnetic actuation*. PhD thesis, Aalborg University. Department of Control Engineering, 1996.
- [29] S Bhat. Controllability of nonlinear time-varying systems: applications to spacecraft attitude control using magnetic actuation. *Automatic Control, IEEE Transactions on*, 50(11):1725–1735, 2005.
- [30] F Landis Markley. Fast quaternion attitude estimation from two vector measurements. *Journal of Guidance, Control, and Dynamics*, 25(2):411–414, 2002.
- [31] John L Crassidis, F Landis Markley, and Yang Cheng. Survey of nonlinear attitude estimation methods. *Journal of Guidance, Control, and Dynamics*, 30(1):12–28, 2007.
- [32] Matthew C VanDyke, Jana L Schwartz, and Christopher D Hall. Unscented Kalman filtering for spacecraft attitude state and parameter estimation. *Department of Aerospace & Ocean Engineering, Virginia Polytechnic Institute & State University, Blacksburg, Virginia*, 2004.
- [33] John L Crassidis and F Landis Markley. Unscented filtering for spacecraft attitude estimation. *Journal of guidance, control, and dynamics*, 26(4):536–542, 2003.
- [34] Simon J Julier and Jeffrey K Uhlmann. A general method for approximating nonlinear transformations of probability distributions. Technical report, Technical report, RRG, Department of engineering science, University of Oxford, 1996.
- [35] Simon S Haykin, Simon S Haykin, and Simon S Haykin. *Kalman filtering and neural networks*. Wiley Online Library, 2001.
- [36] Mark L Psiaki, Francois Martel, and Parimal K Pal. Three-axis attitude determination via Kalman filtering of magnetometer data. *Journal of Guidance, Control, and Dynamics*, 13(3):506–514, 1990.

## Bibliography

- [37] Todd Humphreys. Attitude determination for small satellites with modest pointing constraints. 2002.
- [38] Simon Dan. Optimal state estimation Kalman H and nonlinear approaches, 2006.
- [39] Jouni Hartikainen, Arno Solin, and Simo Särkkä. Optimal filtering with Kalman filters and smoothers—a manual for Matlab toolbox EKF/UKF. 2011.
- [40] H Iida and Keiken Ninomiya. A new approach to magnetic angular momentum management for large scientific satellites. *NEC research & development*, 37(1):60–77, 1996.
- [41] Mark L Renard. Command laws for magnetic attitude control of spin-stabilized earth satellites. *Journal of Spacecraft and Rockets*, 4(2):156–163, 1967.
- [42] Masamichi Shigehara. Geomagnetic attitude control of an axisymmetric spinning satellite. *Journal of spacecraft and rockets*, 9(6):391–398, 1972.
- [43] Carlo Arduini and Paolo Baiocco. Active magnetic damping attitude control for gravity gradient stabilized spacecraft. *Journal of Guidance, Control, and Dynamics*, 20(1):117–122, 1997.
- [44] Marco Lovera and Alessandro Astolfi. Spacecraft attitude control using magnetic actuators. *Automatica*, 40(8):1405–1414, 2004.
- [45] Francois Martel, Parimal Pal, and Mark Psiaki. Active magnetic control system for gravity gradient stabilized spacecraft. 1988.
- [46] K.L. Musser and L.E. Ward. Autonomous spacecraft attitude control using magnetic torquing only. *Flight Mechanics Estimation Theory Symposium*, pages 23–37, 1989.
- [47] T. Flatley, W. Morgenstern, A. Reth, and F. Bauer. A B-dot acquisition controller for the RADARSAT spacecraft. In *NASA conference publication*, pages 79–90. NASA, 1997.
- [48] H.N. Shou, J.S. Sheu, and J.H. Wang. Micro-satellite detumbling mode attitude determination and control: UKF approach. In *Control and Automation (ICCA), 2010 8th IEEE International Conference on*, pages 673–678. IEEE, 2010.
- [49] A.V. Oppenheim and R.W. Schaffer. *Discrete-time signal processing*. Pearson Education, 2010.
- [50] Hassan K Khalil and JW Grizzle. *Nonlinear systems*, volume 3. Prentice hall Upper Saddle River, 2002.

- [51] Mark L Psiaki. Magnetic torquer attitude control via asymptotic periodic linear quadratic regulation. *Journal of Guidance, Control, and Dynamics*, 24(2):386–394, 2001.
- [52] Matias Tassano, Pablo Monzon, and Juan Pechiar. Attitude determination and control system of the Uruguayan CubeSat, AntelSat. In *Advanced Robotics (ICAR), 2013 16th International Conference on*, pages 1–6. IEEE, 2013.
- [53] David A Vallado and Paul Crawford. SGP4 orbit determination. In *Proceedings of AIAA/AAS Astrodynamics Specialist Conference and Exhibit*, pages 18–21, 2008.
- [54] CC Finlay, S Maus, CD Beggan, TN Bondar, A Chambodut, TA Chernova, A Chulliat, VP Golovkov, B Hamilton, M Hamoudi, et al. International geomagnetic reference field: the eleventh generation. *Geophysical Journal International*, 183(3):1216–1230, 2010.
- [55] David A Vallado. *Fundamentals of astrodynamics and applications*, volume 12. Springer, 2001.
- [56] Pablo Yaniero and Simon Gonzalez. Desarrollo de software para CubeSat. 2014.
- [57] FR Hoots and RL Roehrich. Spacetrack report No. 3, models for propagation of NORAD element sets. december 1980.
- [58] Sara R Ostrom. Parallelization of the air force space command (AFSPACE-COM) satellite motion models. Technical report, DTIC Document, 1993.
- [59] V Alonsoperez, A Castro, and S Zito. Proyecto Lai sistema de determinacion de actitud. 2011.
- [60] GomSpace ApS. Nanopower P110 series solar panels datasheet, 2013.
- [61] Silonex Inc. SLCD-61N8 solderable planar photodiode datasheet. 104118 REV 0.
- [62] Analog Devices. Programmable low power gyroscope ADIS16251 datasheet, 2009.
- [63] PNI Sensor Corporation. PNI MicroMag 3, 3-axis magnetic sensor module datasheet, 2008.
- [64] Texas Instruments Incorporated. MSP430F543xA, MSP430F541xA datasheet, Jan 2010.
- [65] STMicroelectronics. STM32F302xB, STM32F302xC, STM32F303xB, STM32F303xC datasheet, 2012.
- [66] Gustavo De Martino. Software y protocolos para CubeSat. Dec 2013.

## Bibliography

- [67] NASA Goddard Space Flight Center. EEE-INST-002: Instructions for EEE parts selection, screening, qualification, and derating, May 2003.
- [68] Mohammad Abdelrahman and Sang-Young Park. Sigma-point Kalman filtering for spacecraft attitude and rate estimation using magnetometer measurements. *Aerospace and Electronic Systems, IEEE Transactions on*, 47(2):1401–1415, 2011.
- [69] David M Harland and Ralph Lorenz. *Space systems failures: disasters and rescues of satellites, rocket and space probes*. Springer Science & Business Media, 2007.

# List of Tables

1.1	AntelSat orbital parameters. . . . .	9
2.1	TLE set format [18] . . . . .	14
6.1	Specifications for coils. . . . .	86
6.2	Dipole values of different magnetorquers for $V_{coil} = +5\text{ V}$ . . . . .	87
6.3	AntelSat ADCS sensors . . . . .	90
6.4	Specifications for the SLCD-61N8 photodiode. . . . .	90
6.5	Specifications for the ADIS16251 gyroscope. . . . .	91
6.6	Specifications for the MicroMag 3 magnetometer. . . . .	92
A.1	Total magnitude of worst case torque. . . . .	100

This page has been intentionally left blank.

# List of Figures

1.1	AntelSat ready to be inserted into a P-POD. This picture was taken inside a clean room at Cal Poly. . . . .	3
1.2	AntelSat nanosatellite subsystems and their interconnections. . . .	4
1.3	Render of the AntelSat with antennas in a stowed configuration. . .	6
1.4	Render with an exploded view of the AntelSat. . . . .	6
1.5	Diagram of Dnepr rocket (units in mm) [14]. . . . .	9
2.1	Geometric properties of an ellipse and Keplerian orbital elements. .	12
2.2	Inertial Reference Frame . . . . .	15
2.3	Orbit Reference Frame . . . . .	16
2.4	Body Reference Frame . . . . .	16
2.5	Observed daily radio flux at 10.7 cm [1]. . . . .	21
2.6	Density vs. altitude for various F10.7 values [1]. . . . .	21
2.7	Earth's magnetic field modelled as a dipole magnet. N stands for the north pole of the dipole magnet. . . . .	22
2.8	Total magnetic field strength contours in $nT$ . The data was generated using the IGRF model for Jan 1st, 2010 for an orbit height of 630 km [13]. . . . .	23
2.9	Fundamental underactuation. Not all degrees of freedom may be manipulated at any given time. . . . .	27
3.1	Deterministic Attitude Determination Process Diagram . . . . .	34
3.2	Attitude error in degrees of QuEst with respect to $\mathbf{q}_{bo}$ . . . . .	46
3.3	Absolute attitude error in degrees of QuEst with respect to $\mathbf{q}_{bo}$ . .	46
3.4	Absolute attitude error of QuEst with respect to $\mathbf{q}_{bo}$ , in logarithmic scale. . . . .	47
3.5	Absolute attitude error in degrees of UKF with respect to $\mathbf{q}_{bi}$ . . .	47
3.6	Absolute attitude error of UKF with respect to $\mathbf{q}_{bi}$ , in logarithmic scale. . . . .	48
4.1	Block diagram of the B-dot controller . . . . .	53
4.2	Block diagram of the state variable filter . . . . .	54
4.3	Angular rate of the satellite applying the B-dot algorithm. . . . .	56
4.4	Magnitude of the angular rate of the satellite applying the B-dot algorithm. . . . .	56
4.5	Control torque for the B-dot algorithm. . . . .	57

## List of Figures

4.6	Total disturbance torque for the B-dot algorithm simulation run. . . . .	57
4.7	Angular rate of the satellite applying the B-dot algorithm (Y-axis coil off). . . . .	58
4.8	Magnitude of the angular rate of the satellite applying the B-dot algorithm (Y-axis coil off). . . . .	59
4.9	Control torque for the B-dot algorithm (Y-axis coil off). . . . .	60
4.10	Total disturbance torque for the B-dot algorithm simulation run (Y-axis coil off). . . . .	60
4.11	Angular rate of the satellite applying the B-dot algorithm (only Z-axis coil on). . . . .	61
4.12	Magnitude of the angular rate of the satellite applying the B-dot algorithm (only Z-axis coil on). . . . .	62
4.13	Control torque for the B-dot algorithm (only Z-axis coil on). . . . .	63
4.14	Total disturbance torque for the B-dot algorithm simulation run (only Z-axis coil on). . . . .	64
4.15	Attitude Euler Angles . . . . .	68
4.16	Body Angular Rate . . . . .	68
4.17	Attitude Quaternion . . . . .	69
4.18	Applied Magnetic Dipole . . . . .	69
4.19	Attitude Euler Angles (with perturbances) . . . . .	70
4.20	Body Angular Rate (with perturbances) . . . . .	70
4.21	Attitude Quaternion (with perturbances) . . . . .	71
4.22	Applied Magnetic Dipole (with perturbances) . . . . .	71
5.1	Top hierarchical block of the AntelSat attitude simulator. . . . .	74
5.2	Sensors and actuators top block. . . . .	77
5.3	Sensors block in detail. . . . .	78
5.4	Magnetometer model. . . . .	79
5.5	Model of an individual Sun sensor. . . . .	80
5.6	Gyroscope model. . . . .	81
5.7	Magnetorquer model. . . . .	81
6.1	ADCS diagram with sensors and actuators. . . . .	84
6.2	Picture of the +X side panel with magnetorquer. . . . .	87
6.3	Picture of the +Y side panel with magnetorquer. . . . .	88
6.4	MicroMag 3 magnetometer [63] . . . . .	92
6.5	Block diagram of the hardware of the ADCS. . . . .	93
6.6	Finished flight version of the ADCS board. . . . .	94
B.1	Complete AntelSat with antennas deployed. . . . .	101
B.2	Complete AntelSat with antennas in a stowed position. . . . .	102
B.3	Dimensions check after the thermo-vacuum test. . . . .	102
B.4	Getting AntelSat inside a storage P-POD. . . . .	103
B.5	Interconnection of internal PCBs. . . . .	104
B.6	AntelSat in the integration phase. . . . .	104
B.7	Assembly of the satellite. . . . .	105

## List of Figures

B.8	Handling of one of the solar panels in the lab. . . . .	105
B.9	Photodiodes testing. . . . .	105
B.10	Applying urethane conformal coating on the PCBs. . . . .	106
C.1	Estimated angular rate magnitude. . . . .	108
C.2	Estimated angular rate magnitude vs. sample number. . . . .	108
C.3	Magnetometer readings vs. sample number. . . . .	109



This is the last page.  
Compiled on Wednesday 12<sup>th</sup> August, 2015.  
<http://iie.fing.edu.uy/>